DISSERTATION

BUILDING THE FOUNDATIONS FOR A PHYSICALLY BASED PASSIVE MICROWAVE PRECIPITATION RETRIEVAL ALGORITHM OVER THE US SOUTHERN GREAT PLAINS

Submitted by

Sarah Ringerud

Department of Atmospheric Science

In partial fulfillment of the requirements

For the Degree of Doctor of Philosophy

Colorado State University

Fort Collins, Colorado

Spring 2015

Doctoral Committee:

Advisor: Christian D. Kummerow
Co-Advisor: Christa D. Peters-Lidard

Steven C. Reising
Susan C. van den Heever
Thomas H. Vonder Haar

ABSTRACT

BUILDING THE FOUNDATIONS FOR A PHYSICALLY BASED PASSIVE MICROWAVE PRECIPITATION RETRIEVAL ALGORITHM OVER THE US SOUTHERN GREAT PLAINS

The recently launched NASA Global Precipitation Measurement Mission (GPM) offers the opportunity for a greatly increased understanding of global rainfall and the hydrologic cycle. The GPM algorithm team has made improvements in passive microwave remote sensing of precipitation over land a priority for this mission, and implemented a framework allowing for algorithm advancement for individual land surface types as new techniques are developed. In contrast to the radiometrically cold ocean surface, land emissivity in the microwave is large with highly dynamic variability. An accurate understanding of the instantaneous, dynamic emissivity in terms of the associated surface properties is necessary for a physically based retrieval scheme over land, along with realistic profiles of frozen and liquid hydrometeors. In an effort to better simulate land surface microwave emissivity, a combined modeling technique is developed and tested over the US Southern Great Plains (SGP) area. The National Centers for Environmental Prediction (NCEP) Noah land surface model is utilized for surface information, with inputs optimized for SGP. A physical emissivity model, using land surface model data as input, is used to calculate emissivity at the 10 GHz frequency, combining contributions from the underlying soil and vegetation layers, including the dielectric and roughness effects of each medium. An empirical technique is then applied, based upon a robust set of observed channel covariances, extending the emissivity calculations to all channels. The resulting emissivities can then be implemented in calculation of upwelling microwave radiance, and

combined with ancillary datasets to compute brightness temperatures (Tbs) at the top of the atmosphere (TOA). For calculation of the hydrometeor contribution, reflectivity profiles from the Tropical Rainfall Measurement Mission Precipitation Radar (TRMM-PR) are utilized along with coincident Tbs from the TRMM radiometer (TMI), and cloud resolving model data from NASA-Goddard's MMF model. Ice profiles are modified to be consistent with the higher frequency microwave Tbs. Resulting modeled TOA Tbs show correlations to observations of 0.9 along with biases 1K or less and small RMS error and show improved agreement over the use of climatological emissivity values. The synthesis of the emissivity and cloud resolving model input with satellite and ancillary datasets leads to creation of a unique Tb database for SGP that includes both dynamic surface and atmospheric information physically consistent with the LSM, emissivity model, and atmospheric information, for use in a Bayesian-type precipitation retrieval scheme utilizing a technique that can easily be applied to GPM as data becomes available.

TABLE OF CONTENTS

Chapter 1: Introduction and Motivation

Precipitation detection and measurement from space has been a central interest and goal of satellite meteorology since the earliest images were transmitted to the surface (e.g. Fritz and Winston 1962). Quantitative measurement of global precipitation via satellite has evolved along with technology and algorithm complexity, from early regression-based visible and infrared techniques (Barrett 1970, Arkin and Meisner 1987) to the utilization of active sensors such as the Tropical Rainfall Measuring Mission (TRMM) precipitation radar (PR) (Kummerow et al. 1998). The recently launched Global Precipitation Measurement (GPM) mission (Hou et al. 2014) will further advance understanding of global precipitation through utilization of a constellation of passive microwave radiometers, along with a dual frequency precipitation radar (DPR). While the radar/radiometer combination contains increased information content, global coverage from a single satellite in low-earth orbit is insufficient. It is therefore advantageous to design passive microwave retrievals that are developed and calibrated using the GPM Microwave Imager (GMI)/DPR combination, and apply this to the much higher spatial and temporal coverage of the passive microwave constellation. The constellation approach, with its greater temporal resolution, has the potential to provide global data useful for various hydrological applications.

Current passive microwave precipitation retrievals differ in approach over ocean and land surfaces. Over the radiometrically cold ocean surface background, emissivities in the microwave regime are generally around 0.5, and any hydrometeors in the column interact strongly with outgoing radiation, leading to higher radiance in areas of liquid water. In the microwave region, the Rayleigh-Jeans approximation may be applied:

$$B_\lambda \cong \frac{2ck_BT}{\lambda^4} \qquad (1)$$

Planck radiance (B), at wavelength λ, can be considered linearly proportional to temperature (T) in this case, where c is the speed of light, and k_B is Boltzmann's constant. The increased radiance resulting from absorption by water can be directly interpreted via an increase in brightness temperature (Tb), relative to the cold ocean background. At higher frequencies of the microwave spectrum, ice scattering is detectable as a depression in Tb. To illustrate, Tbs measured by the AMSR-E radiometer are plotted for a sample swath over eastern South America on June 1, 2003 for the 10.65, 18.7, and 89.0 GHz horizontally polarized channels:

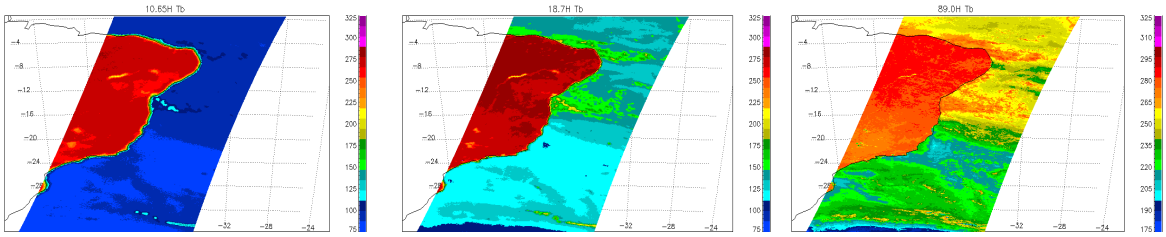

10.65 GHz 18.7 GHz 89.0 GHz

Figure 1.1: AMSR-E brightness temperatures from a June 1, 2003 overpass at the 10.65 (left), 18.7 (center), and 89.0 (right) GHz horizontal polarization channels

Though these frequencies are all within relative atmospheric "window" regions, transmittance is not zero, and one sees some contribution from the atmosphere. The 10.65 GHz channel has the smallest such contribution, and is primarily showing us the surface. Over the ocean there is a clear sensitivity to sea surface temperature (SST), and increased Tb due to liquid water emission off the coast near -16 degrees latitude along with a well-defined band also visible in the southeastern corner. The land in this channel appears much warmer due to the higher emissivity of the surface, and the transition at the coast is

abrupt. Inland water is visible here, for example the Sao Francisco River in the northeast quadrant of the swath. The 18.7 GHz channel is nearer to a weak water vapor absorption line at 22.235. Liquid water in the atmosphere clearly stands out in the previously referenced regions, as does the inland water. At 89 GHz a Tb depression is noticeable in connection with the highest liquid water signals visible at the lower frequencies, suggesting ice scattering from high cloud tops. Higher sensitivity to water vapor is apparent here also. Similar general patterns indicate that the channels are not purely independent, but each appears to have some unique information to offer. The AMSR-E radiometer does not include the highest frequency channels available on the GMI instrument, whose frequencies near 165 and 183 (on the order of ice particle size) GHz are fairly opaque and will offer an even stronger indication of high cloud ice scattering.

Given the information content available from the passive microwave measurements over ocean surfaces, it is possible to develop fully-physical retrieval algorithms that utilize the multi-spectral observations together with a database of Tbs calculated using cloud model hydrometeors and a forward radiative transfer model (Kummerow et al. 2001). Uncertainties associated with this type of retrieval that must be accounted for include measurement error and noise, error in the forward model, representativeness of the cloud model database, beam filling effects, and non-uniqueness of solutions. Such retrievals are used routinely and operationally over ocean surfaces.

In a physical retrieval scheme for precipitation, a forward model is employed, and as the problem is too complex to allow for direct inversion, some method, such as a Bayesian probability scheme, is often chosen to match the results with observed Tbs, and thereby understand deviations and variability via the physical understanding represented

by the model (e.g. Evans et al. 1995, Kummerow et al. 2001). Before the atmospheric component of the observed radiance can be analyzed however, the background must be understood. Over the ocean, the surface emissivity is fairly well understood and related to only a few parameters – sea surface temperature, wind (roughness), sea foam, and salinity. Over land however, surface properties as subtle as leaf direction, and as diverse and variable as soil moisture, surface temperature, and crop lifecycle, will change the contribution of radiance from the surface. The emissivity of the land surface is often closer to 1.0, making atmospheric contributions to the signal more difficult to differentiate as is apparent from the example in Figure 1.1. Surface variations within the large area of a satellite footprint add to the difficulty of the problem. In general, land emissivities are both larger and more variable than for the ocean surface, making this a difficult problem and the key component of this research.

In the most basic sense, the observed brightness temperature is some function of surface and atmospheric properties that interact with microwave radiation: $Tb = F(x)$. This can be further stratified over land into surface (soil and vegetation) and atmospheric contributions, each absorbing and scattering the upwelling radiation. The computational complexity of this model increases as more atmospheric layers are considered, as well as interaction with clouds and precipitation. To interpret the radiation received by the satellite instruments at the top of the atmosphere, each interaction must be understood and accounted for. Generally the atmosphere and surface are simplified to a workable number of layers and parameters to make such computations possible.

As a result of the difficulty in dynamically representing the surface emission, current retrievals resort to empirical algorithms over land (Adler et al. 1994, Conner and Petty

1998) that aim to link ice scattering in the higher frequency channels to precipitation. There are several caveats associated with this type of technique, including precipitation "misses" for warm-cloud precipitation (Petty, 1999), as well as large biases and differences in precipitation intensity distributions when compared to gauge and surface radar data (Tian et al, 2007). The loss of the physical component of the retrieval makes empirical methods less useful as a tool for understanding global precipitation in the context of Earth system science, and to quantify retrieval sensitivities to environmental variables. It is therefore highly desirable to develop a self-consistent physical retrieval over land. Such a retrieval scheme would allow errors and biases to be examined from a physical standpoint, making it more valuable from a science perspective.

Microwave radiation emitted by the land surface and measured using multifrequency, dual-polarization satellites contains information about the character of the surface itself and its properties, suggesting that such measurements can be used in developing the understanding of land surface emissivity necessary for physical retrievals. The surface properties are changing dynamically in space, but are also dynamically varying in time. In the passive microwave regime over light to moderately vegetated land surfaces, emission is sensitive to soil type and soil moisture at lower frequencies, as well as properties of the vegetation cover. In addition to real time monitoring of flood extent and land use changes, observations of surface water and vegetation can be applied to weather forecasting and surface energy budget calculations. A large body of work exists in this area. Grody (1988) demonstrated the feasibility of using microwave radiometers to detect surface type, dividing the surfaces into broad categories including ocean, dry land, wet land, new ice, and old ice. A 1992 study by Heymsfeld and Fulton indicated that in the absence

of dense vegetation, brightness temperatures (Tbs) in the microwave window channels from the SSM/I satellite could be used to detect antecedent precipitation at the surface. Njoku and Li (1999) developed a retrieval using Tbs in the 6-18 GHz range along with a radiative transfer model and an iterative least-squares minimization algorithm for simultaneous retrieval of soil moisture, vegetation water content, and surface temperature, finding results reasonable when compared with coincident model data. The resulting inversion-type technique is used in the standard AMSR-E soil moisture retrieval product as well as retrievals from other platforms (Njoku et al. 2003, Owe et al. 2008). Weng and Grody, (1998) used a similar iterative procedure to retrieve surface temperature using the 19.35 and 22.23 GHz Tbs. Jackson et al. 2002 used multipolarization observations from SSM/I to retrieve soil moisture and compared results to Southern Great Plains (SGP) field campaign measurements, observing reasonable results for pixels that did not include large areas of water bodies, urban areas, or trees. McCabe et al. (2005) performed soil moisture retrievals using a method combining satellite observed 10.7 GHz horizontally polarized brightness temperatures from AMSR-E with surface data from the North American Land Data Assimilation System (NLDAS). This dataset was then coupled with a land surface microwave emission model (LSMEM), finding agreement with field campaign measurements of around 3%. A similar investigation by Gao et al. (2004) retrieved soil moisture using Tbs from an airborne L-band radiometer combined with land surface model data and LSMEM, also showing good agreement with field campaign measurements. The Gao et al. and McCabe et al. studies both indicate that the use of land surface model and parameter data combined with radiative transfer calculations has promising capabilities for passive microwave retrieval of surface soil moisture. More recently, Calvet et al. (2011)

used a coincident measurement system including a 1.41-90 GHz bipolarized radiometer and intensive *in situ* measurements of a dense wheat field, and found good correlation to measured values for retrievals of soil moisture and vegetation water content (VWC). The lowest frequency (i.e. L-band) was determined to have the most sensitivity to soil moisture, while the highest frequency (i.e. W-band) was found to be insensitive to soil moisture with a moderate sensitivity to VWC. In a 2011 study, Jones et al. used vegetation optical depth retrieved from the AMSR-E 18.7 GHz channel to explore vegetation phenology, including canopy height, density, structure, and water content, finding that the satellite-derived product corresponded well with other metrics of phenology and showed appropriate seasonal and geographic variability.

Liquid water in the form of dew or interception of precipitation by a vegetation canopy can also have observable effects in the passive microwave regime. Jackson and Moy (1999) reviewed previous work in this area and conclude that water interception and dew have a measurable effect on microwave Tbs higher than 5 GHz, masking soil emission. Lin and Minnis (2000) used ground observations of dewpoint and skin-air temperature differences combined with SSM/I emissivities to suggest that dew effects decrease early morning emissivities in Oklahoma by roughly 5%, decoupled from the soil moisture variability. The same effect is noted by Moncet et al. (2011) in the U.S. corn belt region during the summer months.

Work has also been done by Grody (2008) on the retrieval of snow parameters, showing a sensitivity to snow grain size in the 23, 31, 89, and 150 GHz channels along with information about snowpack age. Hong (2010) used the AMSR-E 6.9 GHz channel to retrieve information about small-scale roughness and refractive index of sea ice and snow,

as a way of monitoring sea ice and climate change. Multi-frequency algorithms have been developed for dynamic retrieval of snow depth using models of grain size variation as a function of emission in microwave frequencies (Kelly et al. 2003). Retrieval of any such examples of surface information requires knowledge of surface emission and emissivity at the frequency and polarization of interest.

Accurate, global knowledge of land surface characteristics and associated emissivity offers the potential for future improvement of physical retrieval of atmospheric quantities, such as water vapor, clouds, and rainfall, by providing an accurate background surface over which to calculate radiative transfer through the atmosphere. A summary of many currently employed techniques utilizing satellite observations and modeling techniques is presented in Ferraro et al. 2013. Aires et al. (2001) for example, use a neural network approach, along with a training database of simulated data to retrieve surface temperature, integrated water vapor content, cloud liquid water path, and microwave land surface emissivities in the 19-85 GHz range from SSM/I Tbs over land. A 2004 paper by Skofronick-Jackson et al. utilized the higher frequency channels of the AMSU-B radiometer to retrieve falling snow over land surfaces using a physical model and database of previously reported emissivities for a given snow cover amount. Bauer et al. (2005) used climatological emissivity values along with a variational retrieval scheme to compute rain, snow, and cloud water profiles and assess retrieval errors over land surfaces in preparation for future focus on high latitude and weak precipitation retrievals, finding that the sounding channels provided a high enough signal-to-noise ratio to be useful for global retrievals. The Microwave Integrated Retrieval System (MiRS) retrieval and data assimilation system (Boukabara et al., 2011) simultaneously retrieves atmosphere and

surface states in a 1DVAR approach starting with a first guess surface emissivity from mean retrieved clear sky values. While this approach yields an estimate of surface emissivity, it does so using covariance matrices rather than a physical model directly computing emissivity as a function of the surface properties. It is desirable then, and a goal of the present research as a next step in this area, to determine the feasibility of a coupling between physical models of the atmosphere and a similarly physical model of the surface that would supply dynamically varying surface information for dynamic emissivity estimation.

Dynamic emissivity, changing along with dynamically varying surface characteristics, is difficult to validate, and associated error troublesome to define, as emissivity is not a directly measurable quantity on the large scales observed by satellite platforms. Emissivity can be modeled or retrieved, and the results compared directly in the context of surface properties. The emissivities can also be validated indirectly for clear-sky scenes using top of the atmosphere (TOA) Tbs.

Spaceborne radiometers measuring passive radiation emitted by the Earth's surface offer a unique platform for determining emissivity. Satellite-derived microwave brightness temperature observations include information content about the surface emission in cases where the signal has not been completely saturated by absorption in the atmosphere. In the microwave region, the Rayleigh-Jeans approximation (1) can be applied, and Planck radiance considered linearly proportional to temperature. The observed upwelling Tb at a given polarization and frequency contains contributions from both the surface and a non-scattering atmosphere (downwelling and upwelling) over a specular surface can be written as:

$$Tb = \varepsilon T_{sfc} e^{-\tau(0,z^*)/\mu} + (1-\varepsilon)\int_{z^*}^{0} T_{atm}(z) e^{-\tau(z,0)} d\tau/\mu + \int_{0}^{z^*} T_{atm}(z) e^{-\tau(z,z^*)} d\tau/\mu \qquad (2)$$

Where ε is the surface emissivity, T_{sfc} is the surface temperature, T_{atm} is the temperature of the atmospheric layer at height z, τ is the optical depth of an atmospheric layer, z* is the top of the atmosphere, and μ is the cosine of the incidence angle. The first term is the contribution to TOA Tb from the surface, attenuated by the atmosphere, and the second and third terms contain the attenuated contributions from reflected downwelling and upwelling atmospheric radiation. A vegetated land surface is neither purely specular nor purely Lambertian scattering, but some combination of contributions. Over the SGP area, where the surface type is dominated by agriculture and might be considered rough and Lambertian during the growing season, and less so during periods of bare soil or snow cover, calculations suggest a difference in incoming Tb on the order of 0.1K for AMSR-E-specific calculations. Previous work by Matzler (2005) and Prigent et al. (2006) suggests that at the 53° incidence angle, the specular assumption has little impact, and it is therefore applied here to simplify the radiative transfer. If it assumed that the surface temperature and optical depth of the atmosphere are known, observed Tb can be used to solve for emissivity. Retrieval therefore requires some *a priori* knowledge of the atmosphere and its optical depth in order to remove it and separate the surface emission signal as well as an accurate T_{sfc}. Such retrievals are routinely performed globally in clear-sky conditions. A requirement of accurate emissivity retrieval is an accurate estimate of surface temperature. This becomes an issue particularly in desert areas, where the frequency-dependent

penetration depth is highly variable, and the correct temperature for the emissivity calculation is not straightforward (Moncet et al. 2011).

Emissivity can also be modeled. Physical emissivity modeling requires dynamic inputs for characterizing the surface state. Land surface models (LSMs), such as the National Centers for Environmental Prediction's (NCEP) Community Noah model, contain in their output high-resolution information about surface state, including profiles of soil water and temperature, along with vegetation information (Ek et al. 2003). The coupling of LSM output to a microwave emission model presents many challenges. The observed microwave signal from the soil depends upon the dielectric profile of the local soil and is highly frequency dependent (Jackson and Moy, 1999, Norouzi et al. 2012). At passive microwave frequencies, the penetration layer is relatively shallow, and may not correspond to standard LSM output layering. In this study, an initial goal will be the assessment of how well LSM output can be used as input to a physical emissivity model in the production of reasonable dynamic land surface emissivities. Model results will be compared to retrieved values and assessed in the context of land surface parameters.

Physical modeling of land surface emissivity requires knowledge of surface parameters including skin temperature, soil type/texture and moisture, type, roughness, and moisture content of vegetation, intercepted water or dew, plus a radiative transfer model to compute the radiance of these layers and their interfaces. Scattering and emission must be accounted for and will vary with frequency. Weng et al. (2001) describe such a model, utilizing a 3-layer medium as well as their interfaces and a 2-stream radiative transfer solution. This model, LandEM, is used operationally within the Community Radiative Transfer Model (CRTM) and has been adopted for several recent emissivity

comparison studies (e.g. Ferraro et al. 2013, Ringerud et al. 2014a). Another operationally used source is the Community Microwave Emission Modeling Platform (CMEM) developed by the European Centre for Medium-Range Weather Forecasts (ECMWF). This model is described in Holmes et al. (2008) and is written in a modular format, allowing the user to optimally swap out parameterizations and modeling schemes for individual pieces, offering for example, three semi-empirical soil dielectric mixing models developed for various frequency ranges. Both modeling schemes are semi-empirical, and involve parameterizations developed initially for modeling at lower L-band frequencies (with a much deeper penetration depth) for soil moisture retrieval.

Recent work comparing emissivity values from retrieval algorithms and physical models indicates significant differences between the two (Ferraro et al. 2013, Ringerud et al. 2014a). In particular, modeled emissivities show a significant lack of dynamic variability when compared to retrieved values, with the largest disagreements observed at the higher window channel frequencies. In order to perform physical retrievals using passive microwave satellite measurements, this variability in emissivity must be understood, as it will provide the background emission over which the atmospheric components, such as clouds or precipitation, will be retrieved.

Bytheway and Kummerow (2010) demonstrated that microwave emissivities are not independent of frequency. The authors showed that, for particular regions, robust covariance relationships could be constructed between each of the microwave window channel frequencies. The 10.65 GHz H-pol emissivities were retrieved from equation (2) in clear skies using water vapor and land surface temperature from the Atmospheric Infrared Sounder (AIRS) instrument, and mapped to other channels as a function of retrieved values

using linear fits to the covariance relationships. The authors found that these relationships worked quite well over the Southern Great Plains region, but that the covariance relationships could break down over desert surface types, where challenges persist due to the complexities of the soil moisture profile shape in combination with a much more variable penetration depth for desert soil textures.

For calculation and study of global surface emissivity, it must be possible to accurately calculate emissivity using easily obtainable available *a priori* data. Emissivity depends on both the dielectric and roughness properties of the surface. A quantitative description of surface roughness is difficult, and assumptions of roughness height and standard deviation are required within physical emissivity models in the absence of available input data (Weng et al. 2001). Several parameters necessary for accurate modeling of land surface emissivity in the microwave regime are relatively static (soil type, vegetation type, etc.). Assuming that these parameters are known, the emissivity methodology can be tested in the context of the surface parameters driving the dynamic variability: vegetation, soil moisture, and surface temperature. Dew and intercepted water will likely also need to be included in such a model. Lin and Minnis (2000) suggest that in the Southern Great Plains (SGP) region much of the variability in emissivity could be attributed to a diurnal cycle, likely the result of early morning dew. Moncet et al. (2011) also observed this effect globally over cropland areas using a large database of quality controlled retrieved emissivities. The importance of a correct surface temperature value must be emphasized again here, and cannot be ruled out as a source of error in such investigations.

This study investigates emissivity estimation using both physical models and satellite retrievals. Modeled and retrieved emissivities are examined and compared as a function of dynamic surface characteristics. As a result of these comparisons, a semi-physical technique, combining physical modeling with empirical relationships derived from retrieval, is developed. For validation purposes, emissivity values are combined with atmospheric information in order to compute brightness temperature values at the top of the atmosphere, which can then be compared directly to satellite observations. This is done first for clear-sky cases in order to assess the accuracy of the modeled emissivities. Specific modeling techniques and data sources will be described in detail in the following chapters.

Following the description and validation of the semi-empirical emissivity model, it is utilized in creation of a physical database of the type used for Bayesian precipitation retrieval. Simulated brightness temperatures can then be compared to observed values, and an assessment made as to the sensitivity of the Tbs to characterization of surface emissivity. As the accuracy of the Bayesian retrieval is a direct function of the quality of the database and the ability to accurately simulate observed conditions, the use of dynamically modeled emissivities will be compared with simulations using climatological emissivity values, in order to assess the value added. Building upon the many previous studies discussed here, the main goal of the present research is to determine whether emissivity in the microwave can be physically understood, linked to surface parameters, and simulated with sufficient accuracy to serve as the surface component in development of a physical retrieval of atmospheric parameters over land.

Chapter 2: Emissivity Retrieval and Modeling

Toward the development of the optimal emissivity modeling system for use in physical retrievals of atmospheric and hydrometeor information, it is necessary first to examine and assess currently operational methods. Both emissivity retrieval and modeling will be explored as well as the input data to each. A central goal will be the assessment of how well LSM output can be used as input to a physical emissivity model in the production of reasonable dynamic land surface emissivities. Model results will be compared to retrieved values and assessed with respect to land surface parameters. The following sections, published in the journal Transactions in Geoscience and Remote Sensing and referenced as Ringerud et al. 2014a, describe data and methods used in the satellite retrieval and land surface model + physical emissivity model calculations, followed by a quantitative and qualitative comparison of results from each.

2.1: Clear Sky Emissivity Retrieval

Passive microwave window channel measurements are sensitive to soil moisture because of the effects of water on the dielectric properties of the soil. The same measurements are sensitive to vegetation because of the water content of the vegetation (its dielectric properties) as well as scattering and absorption of radiation by the vegetation itself.

For comparison to the forward model computed emissivities, a clear air emissivity retrieval is developed for the AMSR-E passive microwave window channels. AMSR-E is a conically scanning 12-channel radiometer aboard the National Aeronautics and Space

Administration (NASA) EOS Aqua, a polar orbiting, sun-synchronous satellite. The retrieval is performed using intercalibrated level 1C AMSR-E brightness temperatures. The level 1C standardized format and calibration was developed as an initial prototype framework for the GPM radiometer constellation and is described at http://mrain.atmos.colostate.edu/LEVEL1C/level1C_overview.html. Pixels are determined to be cloud-free using collocated Aqua-Moderate Resolution Imaging Spectroradiometer (MODIS) 1 km cloud mask information (Frey et al. 2008), for which validation at the SGP site indicates 85% agreement with ground based lidar cloud detection, with most mischaracterized scenes corresponding to cases of thin cloud with low optical depth (Ackerman et al. 2008). Cloud clearing is done in the strictest sense, designating as clear only those pixels for which the MODIS algorithm has determined "Confident Clear" over the full extent of the largest AMSR-E footprint size. Cloud-free pixels are then combined with coincident ancillary atmospheric information including the surface skin temperature and water vapor, from the European Centre for Medium-Range Weather Forecasts (ECMWF) interim reanalysis (Dee et al. 2007). ERA-Interim is a reanalysis product, with surface parameters available 3-hourly. Values were interpolated from 1-degree gridded output. Many possible sources of input data exist, particularly for the surface temperature. This includes available satellite-retrieved surface temperature estimates as well as higher resolution model data such as that available from a LSM. ECMWF was chosen here as an independent data source, and one that is routinely used as ancillary data input for satellite retrievals such as GPROF. ECMWF data has been employed in other emissivity studies as well, including Holmes et al. (2008), where it was used in conjunction with the Community Microwave Emission Modeling Platform (CMEM), a forward land surface emissivity model

applicable to the frequency range 1-20 GHz. It is assumed here that cloud water content is zero for the clear sky retrievals. Total precipitable water (TPW) for the pixel is also taken from the ECMWF. As a check of the ECMWF TPW values in the SGP region, a comparison to TPW calculated using balloon sounding data from the ARM SGP central facility is shown in Figure 2.1 for the year 2005 (1418 observations). There is clearly scatter in the comparison, but the agreement is generally good, with a mean bias of 1.26 mm, RMSE of 8.27, and correlation coefficient of 0.81.

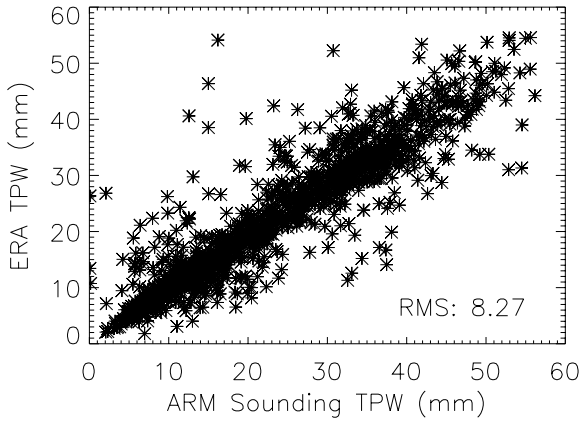

Figure 2.1: Comparison of total precipitable water values (mm) over 1 year (2005, 1418 observations) of data from the ERA-Interim reanalysis and ARM SGP sounding observations.

Radiative transfer calculations are performed through the atmospheric column for the pixel, starting with an initial emissivity guess and assuming a plane parallel atmosphere with no scattering (i.e., no hydrometeors are present in the column). The resulting simulated brightness temperature is compared to the observed Tbs. Emissivity is then adjusted based on the resulting Tb difference in an iterative process following the method of Bytheway and Kummerow (2010). This retrieval scheme is somewhat limited in that it must be assumed that the reanalysis surface temperature is equal to the wavelength-dependent surface skin temperature observed by the satellite, which depends on the

surface type and may be mitigated by vegetation as discussed in the previous section. Monthly mean values have been calculated for the 5-degree SGP box (34:39 N, -100:-95 W) outlined in Figure 2.2 over the years 2004-2011.

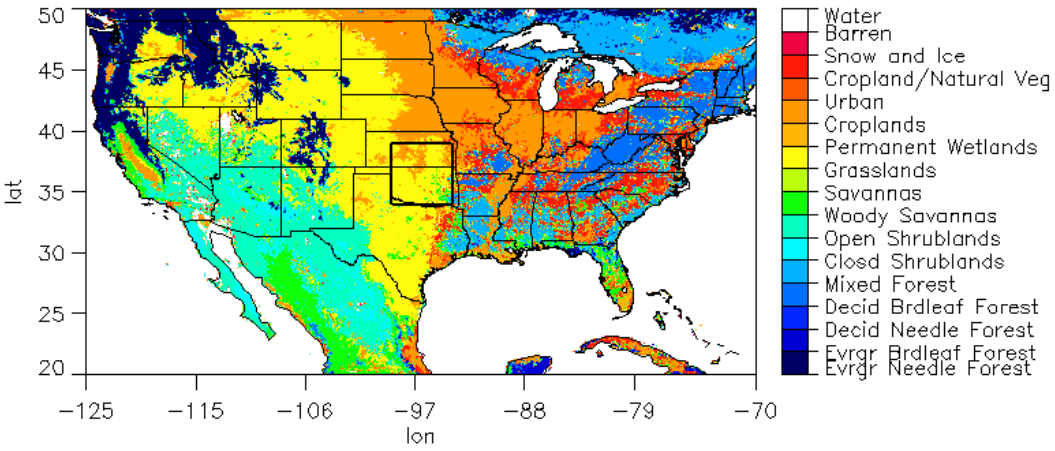

Figure 2.2: Map of the continental US. The SGP box used for the current study is outlined over Kansas and Oklahoma. Colors indicate International Geosphere-Biosphere Programme (IGBP) land surface types for 2009.

Results are shown in Figure 2.3 for the months of January and June at 0.5-degree resolution in order to compare with the climatology available from the Tool to Estimate Land-Surface Emissivities at Microwave frequencies (TELSEM); a nearly 10-year SSM/I-based climatology derived from the years 1993-2001 and described in Aires et al. (2011). Simple averaging has been applied to the retrieved emissivities within each 0.5-degree box for comparison to the TELSEM values. Lower emissivity values relative to the TELSEM climatology are present over the full domain in all frequencies, likely due to differing input surface temperature data sets. Spatial variability over the box is similar. Agreement in the monthly mean half-degree emissivity values is within 0.01-0.02 in January at 89 GHz over much of the domain. Striking low values occur in the AMSR-E retrieved datasets on the

northern edge of the domain that are not observed in the longer TELSEM climatology, likely the result of snow on the ground at the time of AMSR-E overpasses included in the retrieval

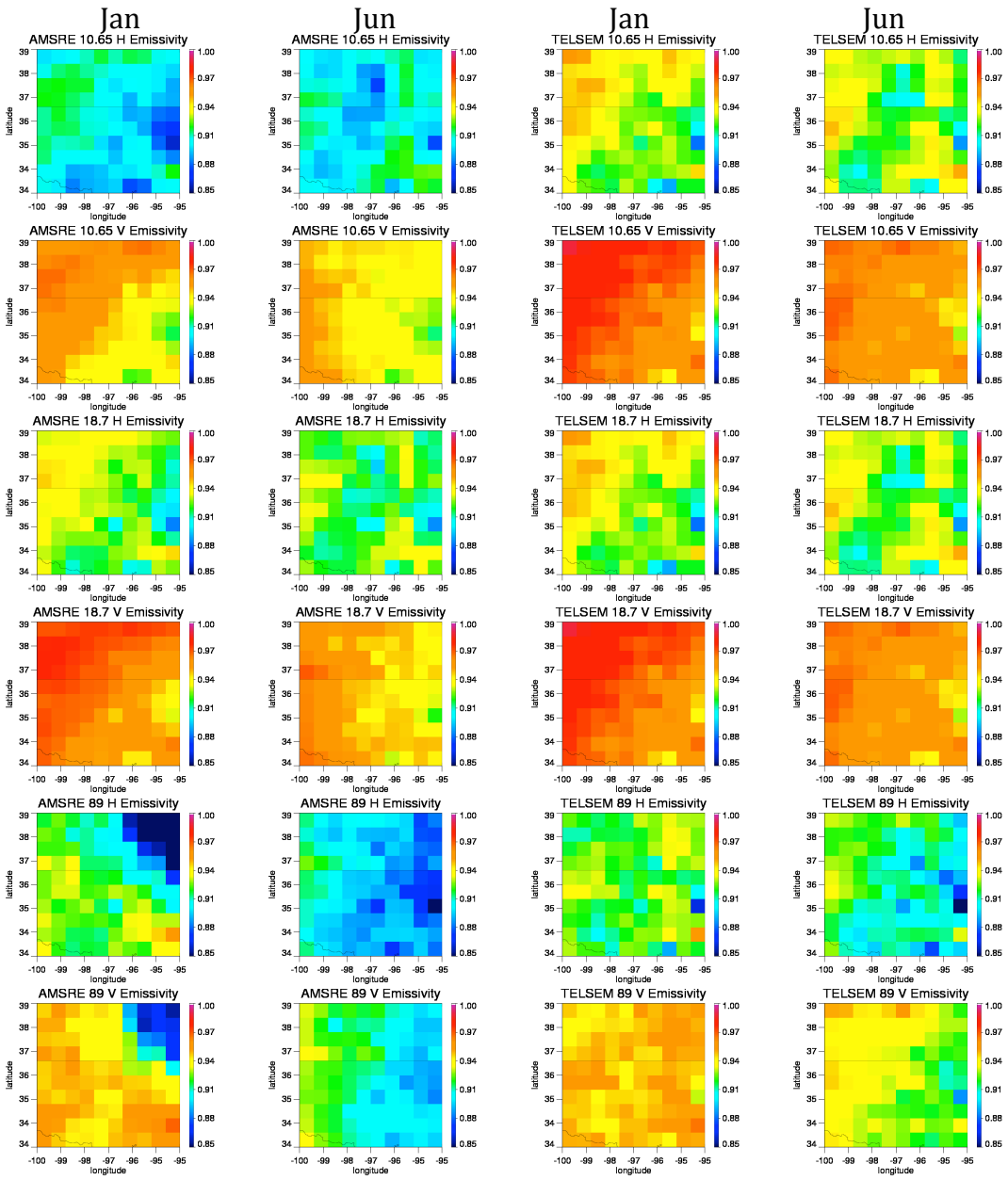

Figure 2.3: Monthly mean AMSR-E retrieved emissivity (left) (2004-2011) compared with TELSEM (right) for the months of January and June over a 5-degree box over SGP for the 10H, 10V, 18.7H, 18.7V, 89H, and 89V channels on AMSR-E. The Oklahoma/Kansas border is visible near 36.5 N.

mean. Emissivity values at 10 and 18.7 GHz show a relative minimum in south-central Kansas, an area of mixed cropland and some pasture/range land (ARM site land use/land

cover web page www.arm.gov). The southeast corner of the grid shows a relative maximum in emissivity in the 10 and 18.7 GHz channels. The seasonal contrast is most evident in the 89 GHz channel, where emissivities are significantly lower in June. The winters are clearly dryer as evidenced by the lower emissivity values in June observed in both datasets and all frequencies throughout the domain. This suggests drier soils leading to a decrease in emissivity at lower frequencies, and indicates less vegetation decreasing emissivity at the higher frequencies.

2.2: Land Surface Model

The land surface modeling portion of this project was implemented using NASA Goddard's Land Information System (LIS), a modular platform for running LSMs with various input as described in Kumar et al. (2006). The land model chosen for this work is NCEP's Community Noah Land Surface Model, version 3.2. Noah is a 1-D, uncoupled model that simulates soil moisture and temperature profiles, skin temperature, snowpack depth and water equivalent, and canopy water content by solving the 1-D surface energy and water balances (Ek et al. 2003). For the purposes of this study, the model was not run over urban areas or bodies of water. Input forcing data comes from the North American Land Data Assimilation System project phase 2 (NLDAS-2). NLDAS-2 has a grid spacing of 0.125 degrees, and non-precipitation fields come from the analysis fields of the NCEP North American Regional Reanalysis (NARR), and the precipitation fields from the gauge-only CPC analysis of daily precipitation temporally disaggregated using Stage II Doppler radar data (Xia et al. 2012). MODIS leaf area index (LAI), an 8-day product derived from visible channel spectral reflectance (Justice et al. 2002), is also an input to the LSM. Validation of

the MODIS LAI product has been performed by multiple international teams, with results suggesting reasonable agreement when compared to field campaign measurements with an average overestimation of around 10% (Yang et al. 2006). The model is run at 1km resolution. NLDAS-2 and other coarser resolution forcing data were spatially interpolated to the target resolution with the budget interpolation scheme, based on the spatial interpolation package "ipolates" from NCEP. A spin-up period of 17 months was included in the model run.

To get a sense of the model output's agreement with observations, 3 years of LSM output soil moisture and soil temperature, along with the NARR/CPC precipitation field are compared to in situ measurements from the USDA Agricultural Research Service's Micronetwork (Elliott et al. 1993). The observations come from a probe measurement at 5 cm depth, while the model data points are associated with a 10 cm top model layer, with the value corresponding to the midpoint at 5 cm. It should be noted here that point measurements are being compared to 1 km resolution model output. Time series comparisons at a single Fort Cobb watershed station (ARS station F102) are shown in Figure 2.4 for the years 2006-2008 in black, with the LSM output over plotted in cyan. The 5-minute observational data reported by the ARS Micronet station has been averaged into 3-hour intervals consistent with the LSM output, and missing data has been removed. Agreement in location of relative maxima and minima in the time series is quite good. The model soil temperature time series shows a somewhat smaller dynamic range than the observations in 2 of the 3 years, particularly in the summer. The soil moisture comparison also shows less dynamic variability on a day-to-day basis in the model, particularly on the

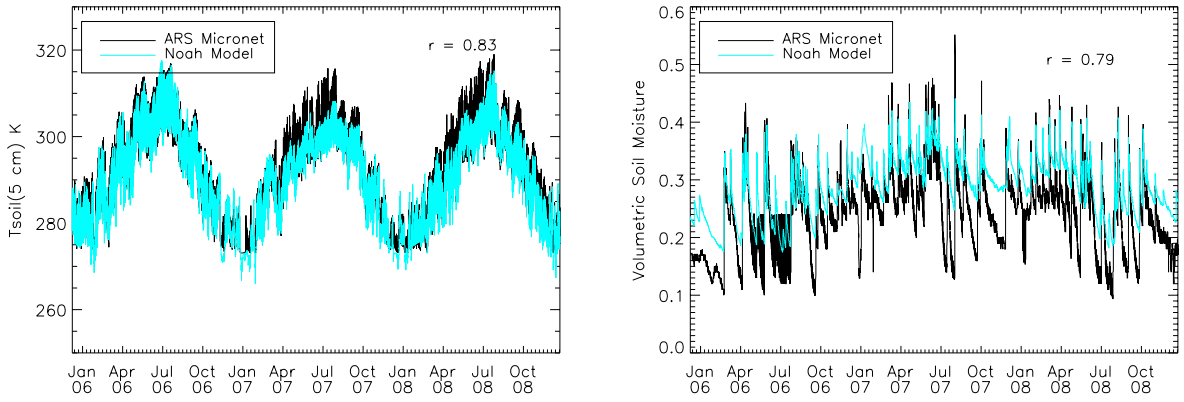

Figure 2.4: 2006-2008 time series of 5 cm soil temperature (left) and soil moisture (right) for micronetwork station F102 in southwestern Oklahoma. Observations are plotted in black, with Noah model results over plotted in cyan.

low end. The agreement is impressive, given the coarseness of the model information, with similar values and patterns of variability. The mean model biases in soil temperature and soil moisture relative to the ARS Micronet observations for the three-year period are -1.19 K and 0.04 respectively, with RMSE of 6.39 and 0.06. Anomaly correlations are high at 0.83 for the soil temperature anomalies and 0.79 for the soil moisture. Based upon model sensitivities that will be described in more detail in the following section, this translates to emissivity differences from the soil temperature bias ranging from almost zero at 6.925 GHz to about 0.005 at 89 GHz. From the soil moisture, the emissivity variation associated with the bias is less than 0.01. Some of this disagreement is likely connected to the location of the soil moisture value in each data set. Also, as stated earlier, this is a comparison of a 1 km model grid cell to a point measurement. Multiscale comparison of soil moisture is a complex and difficult problem, and the agreement in general trends and patterns here is encouraging.

2.3: Physical Emissivity Model

In order to compare LSM parameters to observed emissivity values, a radiative transfer code is required. Weng et al. (2001) describe a 3-layer model for computing land surface ε for microwave frequencies in the range 4.9-94 GHz. The model, LandEM, utilizes input surface properties for computation of the dielectric properties of the soil and vegetation, computing separate dielectric constants for each of the three layers, for example soil, vegetation, and the air above. The model then computes emissivity using a two-stream radiative transfer solution that includes volumetric scattering and reflection and transmission at the layer interfaces. Geometric optics calculations are utilized for canopy leaves. Inputs to the model are viewing angle, frequency, soil moisture content, vegetation fraction, soil temperature, clay fraction, sand fraction, and snow depth. Default parameterized values are used for leaf thickness and water content per unit of LAI. The specific version used for this work was included with the Community Radiative Transfer Model (CRTM) version 2.0.2. Initial validation of the model showed generally good agreement with observations for bare soil and grass, but some disagreement over snow covered surfaces, particularly at higher frequencies (Weng et al. 2001). A simple sensitivity analysis was used to demonstrate the relationship between model emissivity and the input surface properties at SGP. For the analysis, maximum and minimum values over a one year period at an area surface station are used (with the exception of soil type, which varies sand percentage from 0-100%), along with the AMSR-E frequencies and viewing angle. Each parameter is then varied between maximum and minimum values for computation of emissivity while keeping the others constant at their mean value. Minimum, maximum, and mean values of each parameter are shown in Table 2.1, and the resulting emissivity

Table 2.1: Mean, maximum, and minimum surface parameter values from 1 yr. of Noah model run using NLDAS-2 forcing for a single 1 km model pixel in Oklahoma, used for sensitivity calculations in Figure 2.5.

Parameter	Mean	Minimum	Maximum
MODIS LAI (m^2/m^2)	0.67	0.10	5.5
Noah 10 cm Soil Moisture (m^3/m^3)	0.25	0.14	0.14
Noah 10 cm Soil Temperature (K)	291.1	265.9	311.3
STATSGO Sand Content (%)	60	0.0	100.0

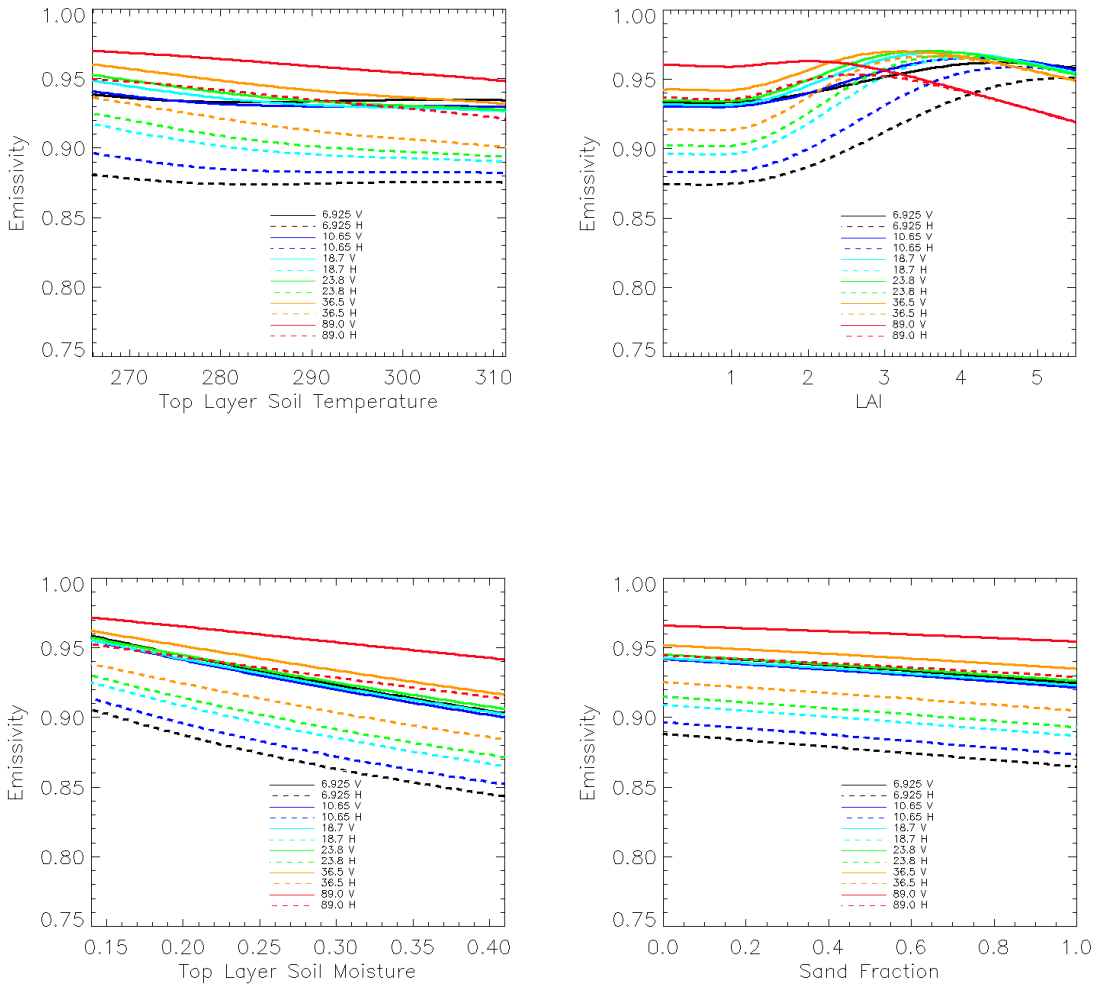

Figure 2.5: Model emissivity values at the AMSR-E Frequencies as a function of the input parameters. Both polarizations are shown for each frequency, with V in the solid lines and H the dashed.

spectra in Figure 2.5. Polarization difference decreases with frequency in all cases for the typical SGP values. Increasing the temperature of the first layer of soil under the vegetation produces a slight decrease in emissivity in all channels, with a slope that increases with frequency. Soil moisture shows the expected strong connection to emissivity as increased moisture leads to higher dielectric constant and decreased emissivity. This effect decreases as frequency increases. The variation of soil type, shown in the bottom right panel, demonstrates that increasing sand content tends to increase the dielectric constant at a given soil moisture, as more water is available in the soil. This leads to a decrease in emissivity. When clay content (in this case 1 - sand content) increases, more bound water is in the soil system, leading to a lower dielectric constant (Owe and Van de Griend 1998). As the leaf area per ground area, LAI, is increased in the model, the polarization difference decreases to almost zero at the highest values of LAI. The LAI effect is the most non-linear of the sensitivity results, showing a steepening of the emissivity change at a value of 2-3. Following the sharp increase, there is a leveling off of emissivity at all frequencies, with a decrease apparent at the highest LAI values. The degree of decrease increases with frequency. The representation of microwave emission from snow cover by the LandEM algorithm is based on dense medium theory and described in Weng et al. (2001). As very little snow cover is observed in the SGP area, and passive microwave sensors historically have difficulty with quantitative handling of snow on the ground due to the variability of emission based on snow depth, age, grain size, and other unknowns, the modeling and observation of snow cover will not be further discussed here.

For the purposes of this study, Noah land surface model data as described in section 2.2 is utilized as input to the Weng et al. emissivity model. Emission depth is not

considered as a variable in this implementation, and values of soil moisture and soil temperature from the top-most model layer (10 cm thickness with reported value at 5 cm) are used as input to the emissivity model for this initial comparison.

2.4: Analysis of Model-Retrieval Comparison

Monthly mean emissivity values computed by the Noah + LandEM coupling are shown averaged for 0.5 degree boxes over the SGP study area in Figure 2.6. For comparison with the satellite methods, footprint averages have been used and only footprints corresponding to a clear-sky AMSR-E overpass are included. The identical time period 2004- 2011 is used. A bias is evident with respect to the satellite retrieval methods plotted in Figure 2.3, but there is some consistency in the spatial patterns.

In order to compare modeled and retrieved land surface emissivities in the context of associated surface properties, both retrieved and modeled emissivities are calculated for all months and seasons of the years 2004-2011 over the full 5x5-degree box shown in Figure 2.2. Results of emissivity calculations are first compared for the full box in bins defined by MODIS LAI and LSM soil moisture values nearest the surface. Results of emissivity calculations are first compared for the full 5-degree box in bins defined by MODIS LAI and LSM soil moisture values nearest the surface. The computed difference between retrieved and modeled instantaneous emissivity values in each of the soil moisture-LAI bins is plotted in Figure 2.7 for each of the 12 AMSR-E channels over all cloud-free data points in the full 2004-2011 dataset. Comparisons are computed for the AMSR-E footprint size at each frequency and include all seasons. Colors indicate the percent difference in instantaneous emissivity values (modeled minus retrieved) as a

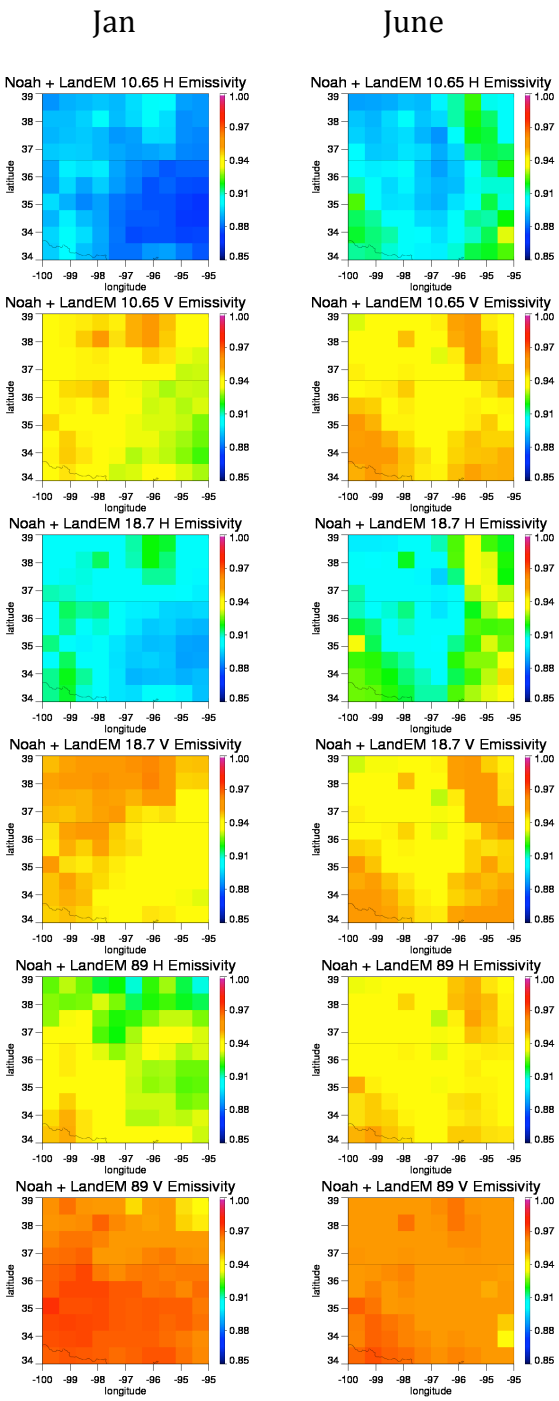

Figure 2.6: Monthly mean Noah + LandEM computed emissivities for the months of January and June 2004-2011 for a 5-degree box over SGP for the 10H, 10V, 18.7H, 18.7V, 89H, and 89V channels at 0.5-degree resolution. Only MODIS cloud-free times are included for comparison to figure 2.3. The Oklahoma/Kansas border is visible near 36.5 N.

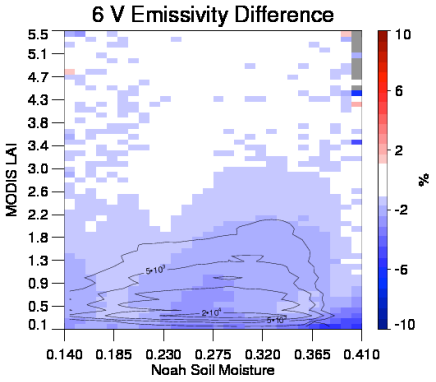
6 V Emissivity Difference
MODIS LAI
Noah Soil Moisture
%

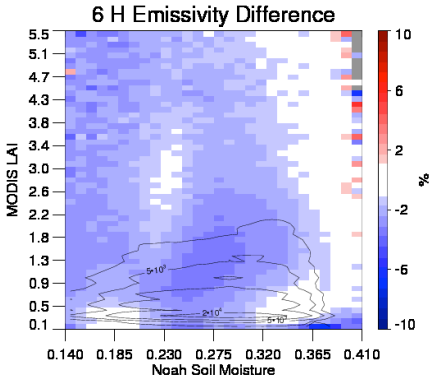
6 H Emissivity Difference
MODIS LAI
Noah Soil Moisture
%

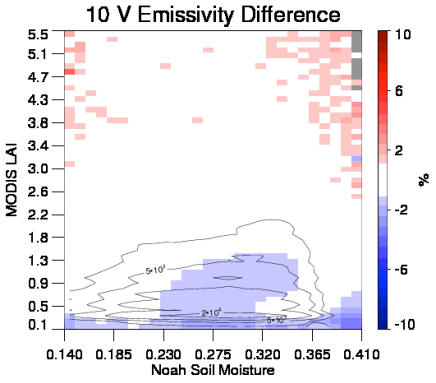
10 V Emissivity Difference
MODIS LAI
Noah Soil Moisture
%

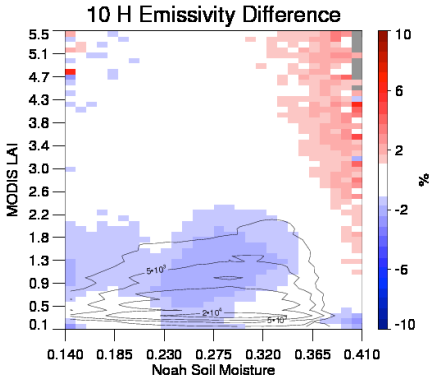
10 H Emissivity Difference
MODIS LAI
Noah Soil Moisture
%

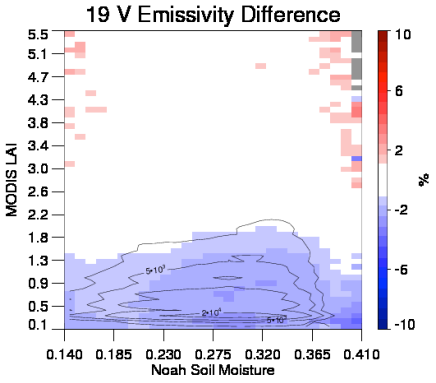
19 V Emissivity Difference
MODIS LAI
Noah Soil Moisture
%

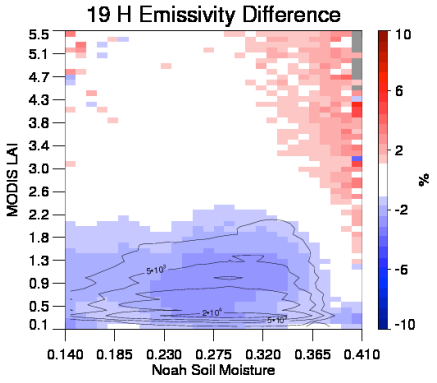
19 H Emissivity Difference
MODIS LAI
Noah Soil Moisture
%

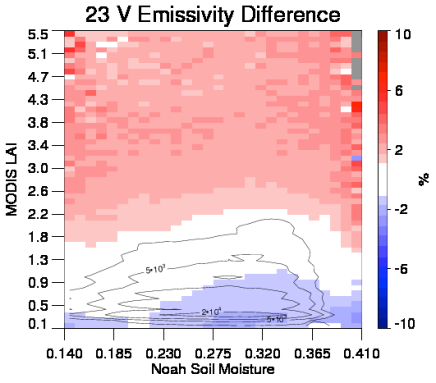
23 V Emissivity Difference
MODIS LAI
Noah Soil Moisture
%

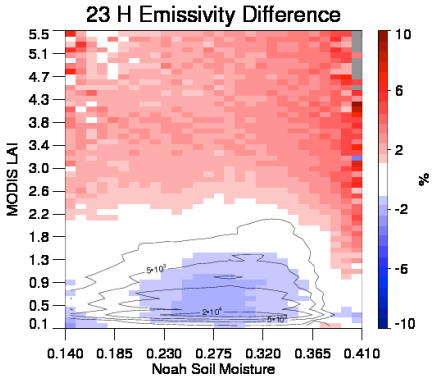
23 H Emissivity Difference
MODIS LAI
Noah Soil Moisture
%

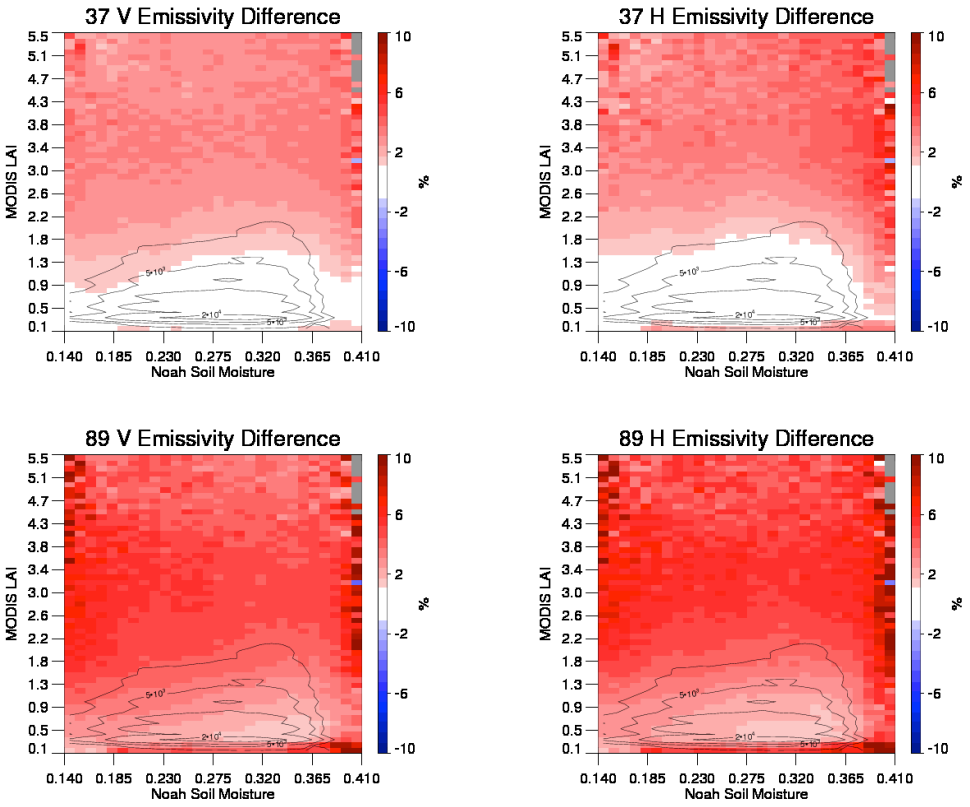

Figure 2.7: (Model – Retrieved) emissivity differences as percent of the mean retrieved emissivity in each channel over the 5-degree SGP region for all seasons of the years 2004-2011, as a function of Noah soil moisture and MODIS LAI. Colors indicate the emissivity differences (%) and contours show the total points falling into each bin (3.2 million total).

percent of the mean retrieved emissivity in each channel over the full period. White space indicates agreement within 1%. Contours show the number of data points falling into each bin, with the plotted lines indicating bins with 2500, 5000, 10,000, and 20,000 of the 3.3 million total matched cloud-free comparison points. In each channel, agreement is better in the vertical polarization. At the lowest frequency, the 6.9 GHz channel often used for soil moisture remote sensing, the model values are almost uniformly lower than the retrieved emissivities, with differences less than 5%. In the 10, 18.7, and 23 GHz channels, agreement is quite good, with differences around 1-2%. The plots for these channels show a dipole-type distribution, with the model emissivities being lower than retrieved values

for LAI less than about 2.0, and becoming higher than retrieved at larger LAIs. Agreement improves with increasing LAI in these lower frequencies where soil moisture sensitivity is high, particularly in the vertical polarization, which is slightly less sensitive to soil moisture (Fig 6). The contours indicate that the higher LAI values are seldom observed, however, and may therefore be less reliable comparisons. At the higher frequencies of 37 and 89 GHz, the model emissivities are nearly uniformly higher than the retrieved values, though it is notable that in the LAI-soil moisture bins most highly populated, differences are generally less than or equal to 1%. Disagreement increases with LAI and shows little dependence on soil moisture, as would be expected at these frequencies and their much shallower emission depth.

The analysis of modeled emissivity sensitivity shown in Figure 2.4 along with the emissivity differences shown in Figure 2.7, demonstrate the large influences of LAI and soil moisture on emissivity variability in the SGP area. To explore these dynamics further, two individual points in the full 5x5 degree model domain are chosen for closer analysis in the context of surface parameters as well as temporal variability. Both are part of the ARM Southern Great Plains (SGP) extended facility observation network covering most of Oklahoma and southern Kansas. The first is Pawhuska, an area in northeast OK dominated by natural grasses. The second is Halstead, in central Kansas, and represents an agricultural region with rotating crops including winter wheat. Comparisons of instantaneous emissivities are performed at the resolution of the AMSR-E footprint. Time series of the associated surface parameters are included and the methods used to produce emissivities are as described in the previous sections. Mean values of MODIS LAI, as well as model output soil moisture and temperature for the two stations are given in Table 2.2. It

is notable that while both data points share the same mean temperature, Pawhuska has a much higher LAI, indicating denser vegetation per area, and is also moister, making the sites an illustrative choice for comparing resulting emissivity dynamics. Biases are generally consistent with the mean LAI and soil moisture bin differences in Figure 2.7

Table 2.2: Mean surface parameter statistics for 2004-2011 time series (23,376 data points) at two DOE-ARM surface stations.

	MODIS LAI (m^2/m^2)		**Noah 10 cm Soil Moisture (m^3/m^3)**		**Noah 10 cm Soil Temperature (K)**	
	Mean	Standard Deviation	Mean	Standard Deviation	Mean	Standard Deviation
Halstead	0.739	0.385	0.196	0.052	288.7	11.60
Pawhuska	1.37	1.24	0.28	0.066	288.9	10.089

and are generally less than 1% for the lower frequency channels at Halstead and less than 2% for Pawhuska. The difference in vegetation at the two sites is evident in the 3-year timeseries of MODIS-derived LAI shown for each station in Figure 2.8 (top panels). LAI variations clearly appear seasonally and vary from year-to-year. The seasonal cycle is clearly evident in both the surface skin temperature (2nd row) and 5 cm soil temperature (3rd row) at both stations, with a decreased diurnal variability in the soil as compared to the surface. The Pawhuska soil temperature shows less variability than at Halstead, indicating possible temperature mitigation under the much higher values of LAI. Soil moisture series are shown in the 4th row, and a comparison with the last row plotting rainfall indicates soil moisture's close connection to precipitation. The timeseries demonstrate the dynamic variability of the surface parameters influencing emissivity on multiple timescales.

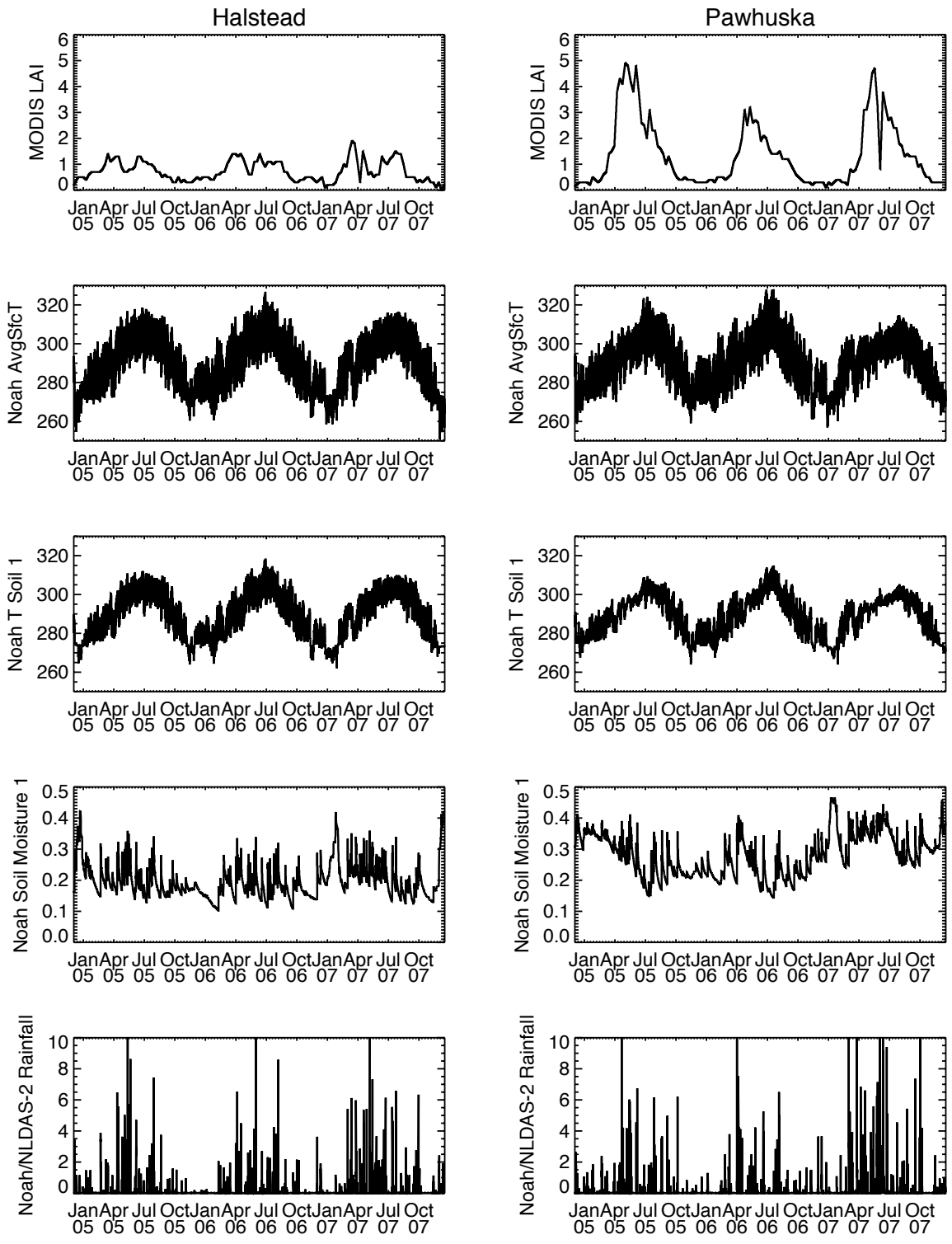

Figure 2.8: Jan 2005-Dec 2007 timeseries of LAI (top), surface temperature, 5 cm soil temperature, 5 cm volumetric soil moisture, and rainfall (bottom) for LSM data at Halstead (left column) and Pawhuska (right column) stations.

As check of mean retrieved emissivity at the two locations, a monthly average emissivity is calculated for a 0.5-degree box over the Halstead and Pawhuska surface stations for the years 2004-2011 and compared to the TELSEM dataset. Both of these are then compared to monthly averages computed from the Noah LSM + LandEM model output for the same 0.5-degree box. Averages are computed for each box at the AMSR-E footprint size and only model values corresponding to a cloud-free retrieval data point are included. The monthly averages for the 10.65, 18.7, and 89 GHz (H and V polarization) AMSR-E channels are shown in Figure 2.9. Agreement between the two satellite methods is quite good with the exception of a fairly constant bias in the 10H and 10V channels. This is not surprising considering the TELSEM climatology is derived from SSM/I measurements and must effectively extrapolate to the 10.65 GHz channel. Monthly variability is very similar for the two retrieved series even in these channels, while the time series of model values is relatively flat, particularly for the Halstead footprint. Retrieved emissivities are higher than the modeled values in the monthly mean at Pawhuska station for both polarizations at 10.65 and 18.7 GHz. The two agree reasonably well at Halstead in absolute value, but the model again appears to lack dynamic changes over the seasonal cycle. The closer agreement at Halstead may suggest that the water-LAI relationships in the LandEM model are more applicable to the agricultural region around that area than to the grazed natural grassland around Pawhuska. In the 89 GHz channel, modeled emissivities show substantially less variability as well as a high bias compared to both retrieval averages. While it is true that passive microwave emissivity retrieval may be contaminated at this higher frequency due to atmospheric effects including contamination by undetected, low optical thickness clouds, the fact that the model values show a consistent bias compared to

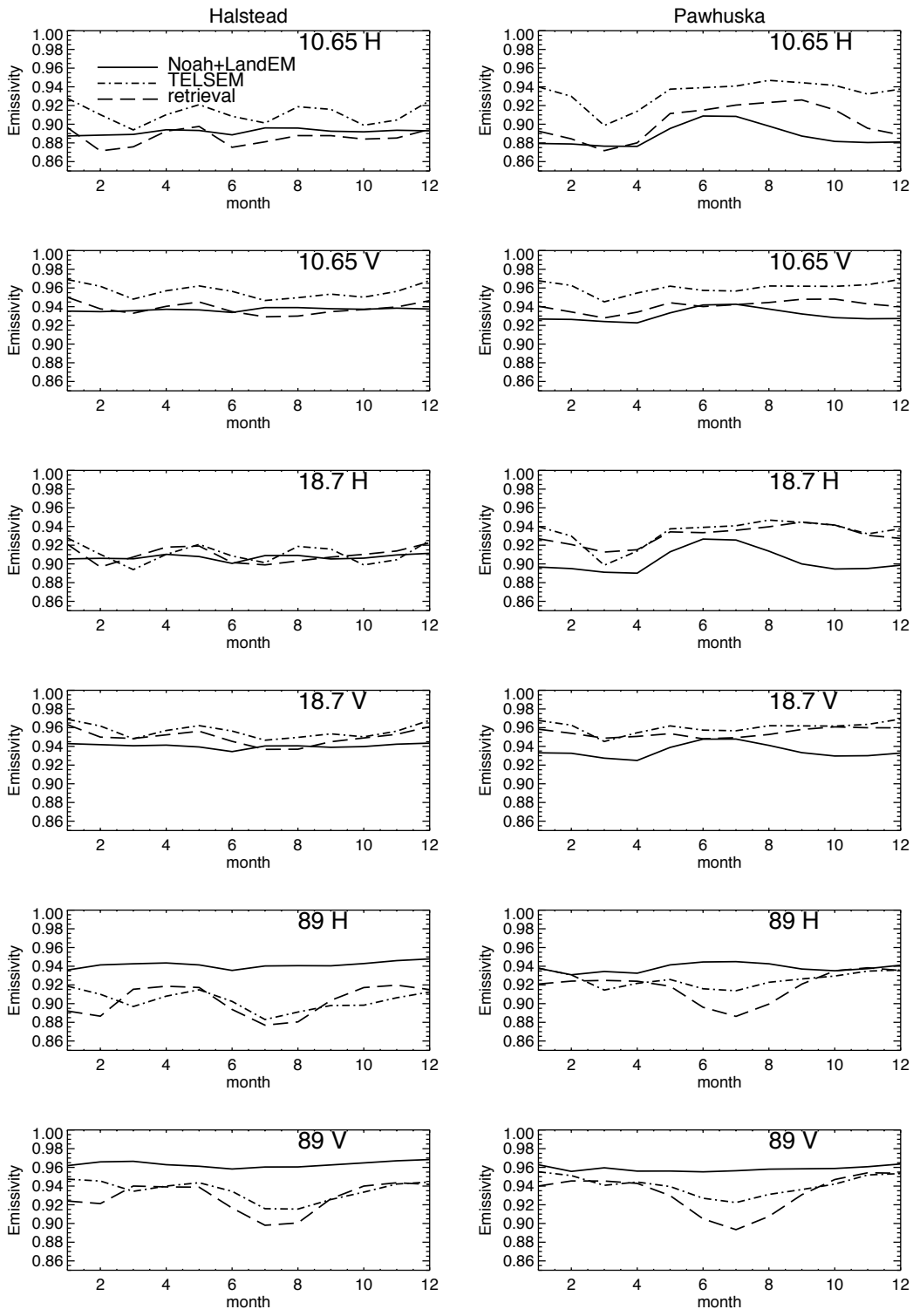

Figure 2.9: Monthly mean emissivity values for a 0.5x0.5 degree box around Halstead (left column) and Pawhuska (right column) stations. Averages computed from 8 years of model data (Noah + LandEM) (solid lines) and 8 years AMSR-E retrievals (dashed lines). The TELSEM 10 year climatology is plotted in the dash-dot lines for comparison.

two completely different retrieval schemes using two different cloud-clearing methods (International Satellite Cloud Climatology Project (ISCCP; Rossow and Schiffer 1999) for TELSEM vs. MODIS here) suggests that this is not the source of disagreement in this case. This channel is sensitive to water vapor amount and vertical distribution, which may be a more likely source of error. Surface temperature discrepancies can be ruled out here as such differences would be expected to lead to a consistent high or low bias over all channels, whereas these results show a flip in the bias with increasing frequency. The highly dynamic nature of the variability in the retrieved values here is suggestive of something not represented in the model, for example dew or post-precipitation canopy water, which behaves in a radiometric sense completely different than water content in the vegetation itself. While it is not possible in this analysis to state definitively the source of disagreement between the methods at 89 GHz, an incorrect representation of the water vapor profile in the retrieval and radiometric effects not captured by the physical model both likely play a role. Figure 2.10 shows the emissivity spectral averages for TELSEM, the AMSR-E retrieval, as well as the Noah-LandEM computations. Averages of the retrieved and Noah-LandEM model emissivities are computed point-by-point at the location of each station at the resolution of the AMSR-E footprint size, and for only cloud-free data points over the full 2004-2011 data set. Agreement between the three methods is closer at Halstead station in the lower frequencies, and deviation increases for higher frequencies between the model technique and the two satellite-derived methods. At Pawhuska station there is more spread at the lower frequencies and somewhat better agreement with the model at 89 GHz. The satellite emissivity methods show close agreement with the

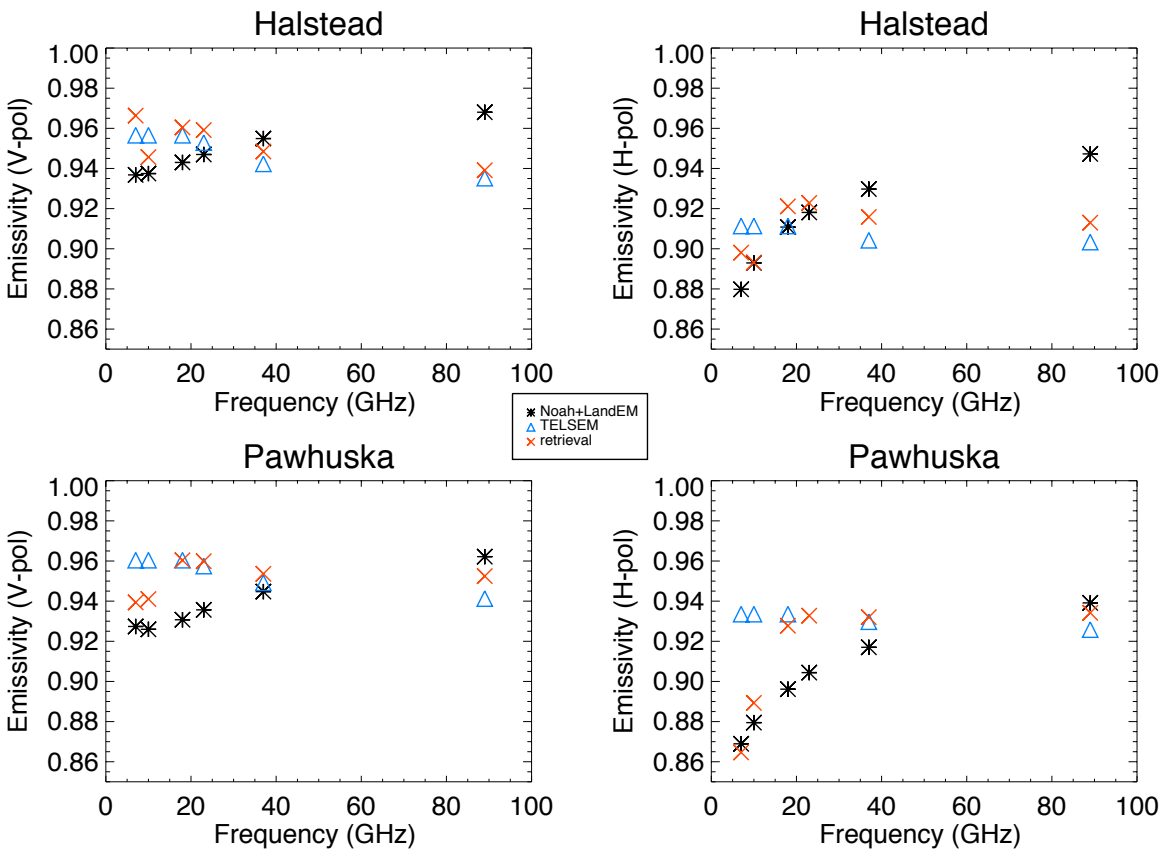

Figure 2.10: Emissivity spectra at Halstead (top) and Pawhuska (bottom) for horizontal (right) and vertical (left) polarizations. Spectra shown are computed from TELSEM (blue), AMSR-E retrievals (red), and LSM + LandEM modeling (black)

interesting exception of lower frequencies at Pawhuska, where the AMSR-E retrieval seems to track more with the model emissivities rather than the TELSEM SSM/I climatology.

The associated instantaneous emissivity anomaly comparisons are shown in Figures 2.11 and 2.12, with mean bias, RMSE, and anomaly correlation statistics included in Table 2.3 for the 2004-2011 period. Anomalies are from the monthly means computed for the entire 2004-2011 period and are calculated for instantaneous retrieved and modeled emissivities at the AMSR-E footprint size. For the Halstead location (Figure 2.11), anomalies are clearly more dynamic in the retrieval at all frequencies, illustrated by the greater spread along the x-direction. Anomaly correlations are around 0.5, with the

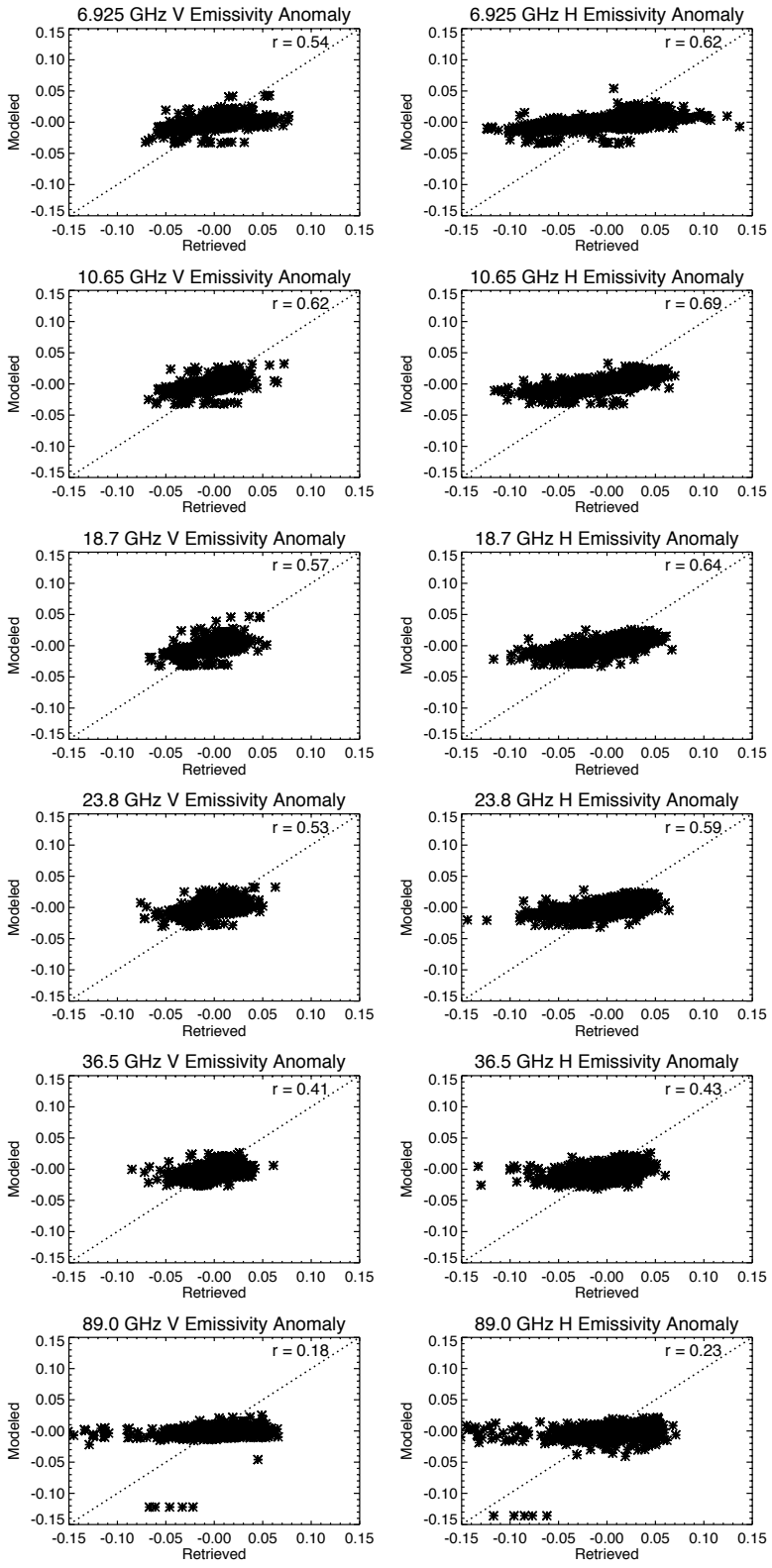

Figure 2.11: 2004-2011 emissivity Noah + LandEM and retrieved emissivity anomalies for the AMSR-E V-pol (left) and H-pol (right) channels at Halstead station.

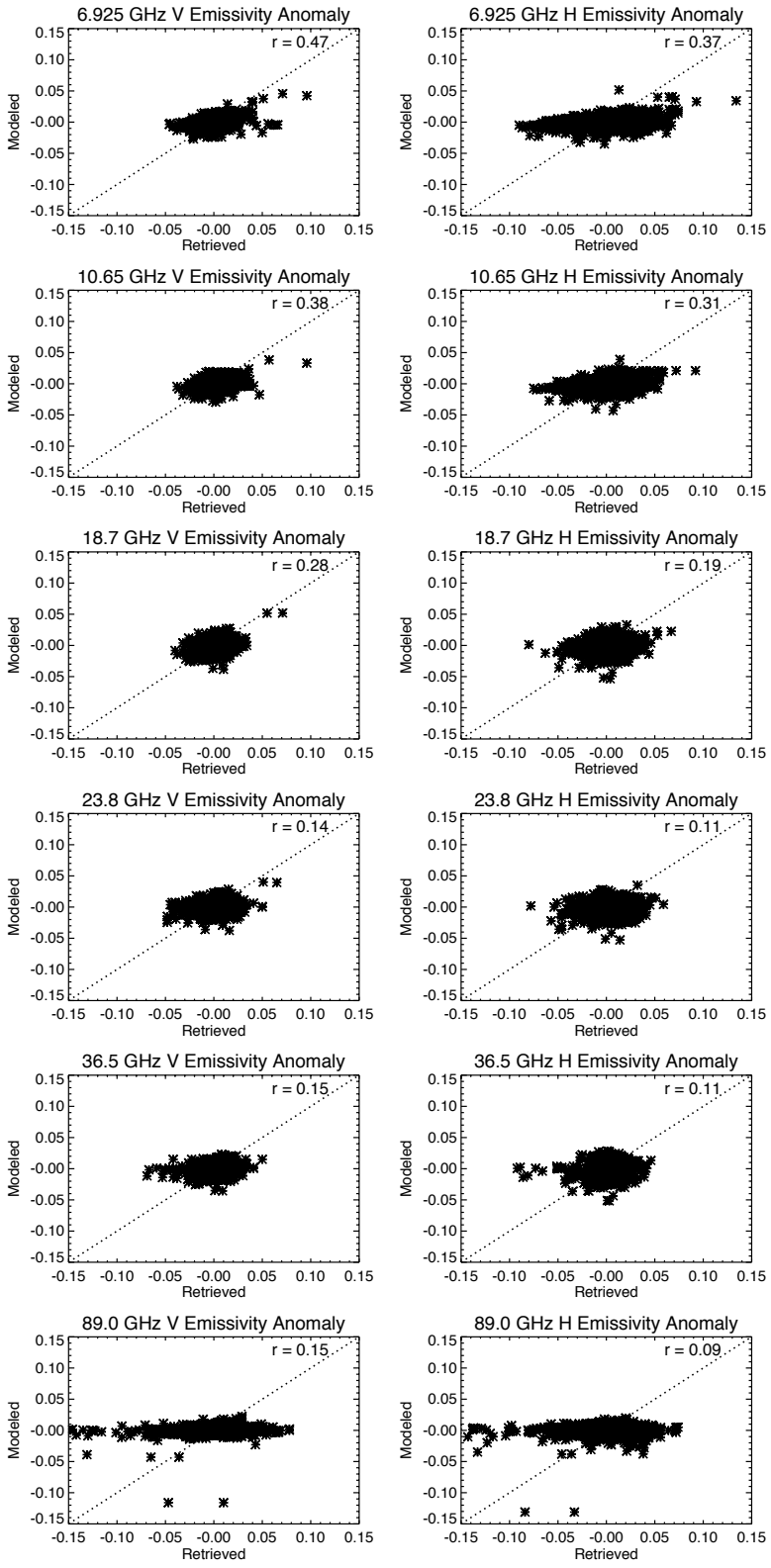

Figure 2.12: 2004-2011 emissivity Noah + LandEM and retrieved emissivity anomalies for the AMSR-E V-pol (left) and H-pol (right) channels at Pawhuska station.

Table 2.3: Emissivity statistics comparing instantaneous forward-modeled and retrieved emissivity values for 2004-2011 at two DOE-ARM surface stations.

6.9 GHz						
	V			H		
	Bias (%)	RMSE	ε correlation	Bias (%)	RMSE	ε correlation
Halstead	-2.10	0.029	0.54	-0.88	0.036	0.62
Pawhuska	-1.28	0.019	0.47	-1.08	0.034	0.37

10.65 GHz						
	V			H		
	Bias (%)	RMSE	ε correlation	Bias (%)	RMSE	ε correlation
Halstead	-0.14	0.016	0.62	0.58	0.027	0.69
Pawhuska	-1.29	0.018	0.38	-1.93	0.031	0.31

18.7 GHz						
	V			H		
	Bias (%)	RMSE	ε correlation	Bias (%)	RMSE	ε correlation
Halstead	-1.15	0.019	0.57	-0.57	0.024	0.64
Pawhuska	-2.34	0.028	0.28	-3.24	0.038	0.19

23.8 GHz						
	V			H		
	Bias (%)	RMSE	ε correlation	Bias (%)	RMSE	ε correlation
Halstead	-0.10	0.017	0.53	0.35	0.024	0.59
Pawhuska	-1.14	0.024	0.14	-2.13	0.032	0.11

36.5 GHz						
	V			H		
	Bias (%)	RMSE	ε correlation	Bias (%)	RMSE	ε correlation
Halstead	0.91	0.018	0.41	1.20	0.026	0.43
Pawhuska	0.12	0.019	0.15	-0.91	0.024	0.11

89.0 GHz						
	V			H		
	Bias (%)	RMSE	ε correlation	Bias (%)	RMSE	ε correlation
Halstead	3.01	0.045	0.18	3.09	0.048	0.23
Pawhuska	2.41	0.043	0.15	1.60	0.041	0.09

exception of the 89 GHz channel, which shows less correlation. Large negative anomalies visible in Figure 2.11 are associated with precipitation events (occurring during a clear-sky overpass following a precipitation event) and are correlated in sign but stronger in magnitude for the retrieved emissivities versus the modeled values. Given that Halstead is a more agricultural surface type, it is possible that irrigation is adding to the soil moisture and increasing the negative anomalies in the retrieval, while the positive anomalies are more correlated in the lower frequency channels. At 89 GHz, emissivities are much more dynamic in the retrieved data than the modeled values, which are relatively flat over the 8-year analysis period. Pawhuska (Figure 2.12) shows less variability in the lower frequency channels. More positive anomalies occur in the retrieval than in the model emissivities. Anomaly correlations are smaller here as well, particularly in the H polarization, and are close to zero at 89 GHz. This analysis suggests that surface emissivity dynamics, as captured by anomalies in the time series, are represented more accurately by the forward model at Halstead station. The model dynamics are flat as compared to variability in the retrievals at all frequencies in both locations. Further improvement in mapping of dynamic surface and vegetation type-specific parameters may improve agreement and is a part of ongoing research. An adequate representation of the dynamics is particularly lacking at 89 GHz for both locations over the course of the 8-year comparison.

The dew effect common in agricultural regions as discussed in Lin and Minnis (2000) and more recently Moncet et al. (2011) is difficult to analyze in this context. While canopy water interception and dew are available output via the land surface model, there is as yet no mechanism in the emissivity model to calculate the radiative effects of the additional liquid atop the vegetation layer. Figure 2.13 shows the canopy interception field

from the Noah model along with modeled and retrieved 89 GHz emissivities for the single month June 2006. It should be noted that while modeled emissivities are plotted here throughout the rain event, retrieved values are calculated only for cloud-free overpasses and not during the rain itself or cloudy periods, leading to gaps in the retrieval plot (lower right). For this summer month, modeled 89 GHz emissivity values are universally higher than the

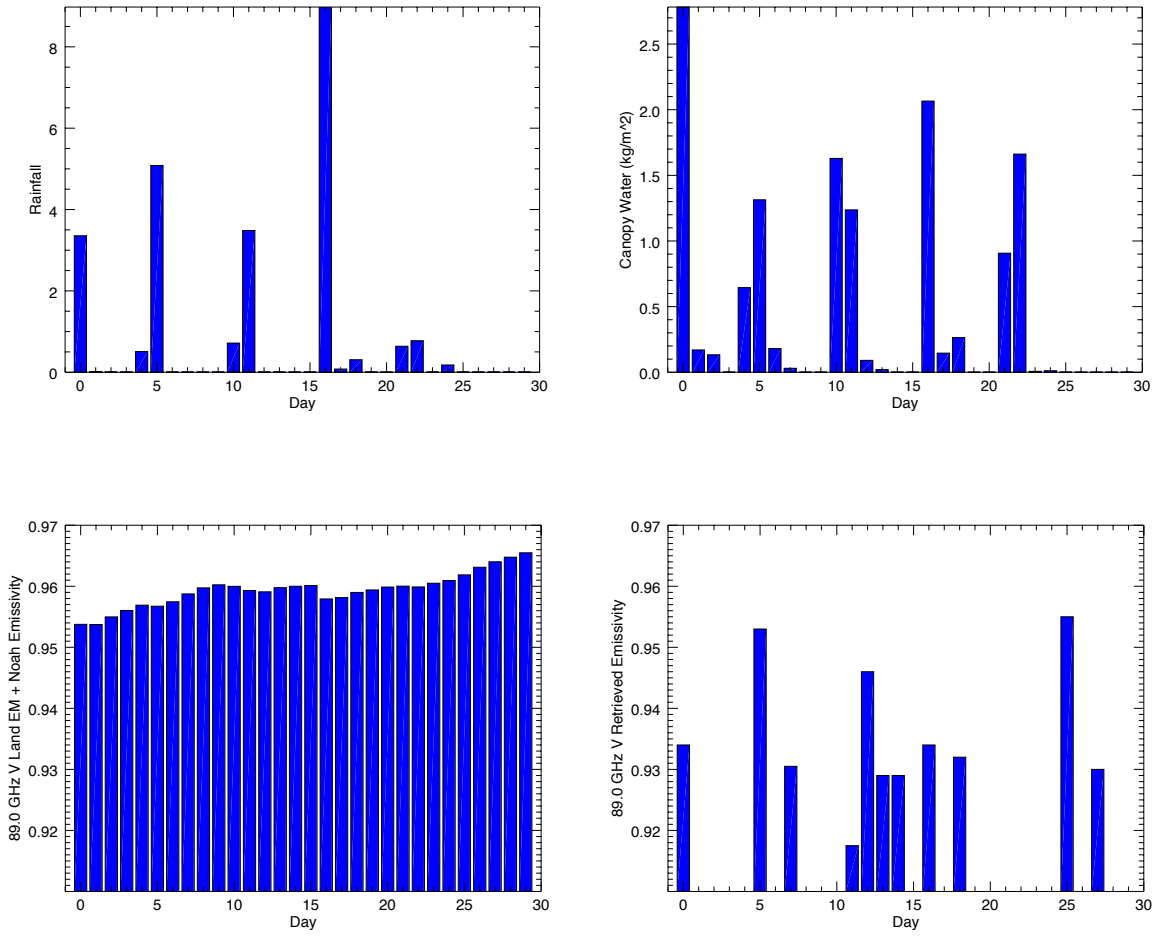

Figure 2.13: June 2006 timeseries of precipitation (top left), canopy water storage (top right), and 89 GHz emissivity from the Noah + LandEM model (bottom left) and AMSR-E clear-sky retrievals (bottom right).

satellite retrieval. Some cases (day 7, for example) show a coincident low retrieved 89 GHz emissivity following a time of precipitation and increased canopy water storage. The model dataset shows a slight drop in 89 GHz emissivity following the rain event of day 16. This decrease is also present and greater in magnitude in the retrieved dataset. There does not, however, appear to be a distinctive connection between these parameters. The comparison suggests that a dew/intercepted water layer may be a useful addition to the physical emissivity model, but more investigation is required to attain agreement at this higher frequency.

2.4: Summary and Conclusions of Emissivity Model-Retrieval Comparison

Analysis of land surface emissivities calculated using both passive microwave retrieval and physical modeling shows a need for some improvement in each method. The combination land surface – physical emissivity model used here does not appear to capture dynamic changes well and is not currently ready for operational use in physical rainfall retrieval. At the lower frequencies, where emissivity is highly sensitive to soil moisture, agreement is generally good for areas of mid-range vegetation density, exemplified by Halstead station, an agricultural area. Larger biases are observed at very low or very high values of LAI. An improvement over the default leaf thickness to one that is a function of vegetation type would likely improve agreement, along with a more functional representation of vegetation content-water relationships. Ideally, a dataset of leaf thickness measurements could be used; however, calibration of leaf thickness parameters may be the only viable approach in the absence of such data. Additionally, the conversion to vegetation water content would likely be improved by a vegetation type-specific

relationship such as described in Jackson et al. (2002). Again, data for the compilation of such an adaptable dynamic parameterization would be necessary and not particularly straightforward, and is beyond the scope of this initial investigation into model-retrieval comparisons. In the end, we simply can't know the thickness, water content, placement, and orientation of every plant and leaf in the domain. This places a limit on the absolute accuracy of physical emissivity modeling for real-time satellite retrieval purposes.

The comparison of modeled and retrieved emissivities is a complicated problem. No validation dataset exists, and the inputs required differ, leading to many possible sources of error. The model contains multiple input datasets, along with uncertainties associated with the land surface modeling scheme itself as well as the radiative transfer within the emissivity modeling component. This represents a bottom-up calculation, whereas the retrieval scheme requires information about the atmosphere and performs radiative transfer down through the atmospheric column. The requirement of strict cloud clearing in the comparisons here is meant to make the atmospheric component as little an issue as possible.

Given the high correlation of emissivity at the lower frequency channels of AMSR-E to changes in soil moisture, precipitation is clearly a major component of dynamic variability. The magnitude of response to precipitation appears to be higher in the retrieved emissivities, but it should be pointed out that the retrieval corresponds to an instantaneous observation whereas the model is a 3-hour average. It is possible that emissivity changes happen on a short timescale as water collects during and following precipitation, then dries. The timescale of drying may be highly variable, and the soil moisture change at the very surface (affecting emissivity) will be a function of soil type and

previous conditions. Irrigation in this type of area will obviously influence the emissivity as well and must be considered in assessing model agreement. The use of 3-hour model data likely affects emissivity changes connected to the soil temperature as well, and influences the models ability to capture diurnal variability.

Interpretation of the emissivity differences at 89 GHz is less clear. It is very likely that the retrieval is glossing over known (but not quantified) errors due to unaccounted-for absorption and scattering in the atmosphere. In fact, Ruston and Vonder Haar reported in a 2004 study that the impact of a cirrus cloud is an order of magnitude greater than differences due to vegetation changes. Clearly there are errors present as well on the model side as suggested by the large bias from two different retrieval methods. In the model, it is possible that unaccounted for radiative effects of liquid water over the vegetation canopy in the form of intercepted precipitation or dew is having an effect. There is a lot of work to be done in reconciling the 89 GHz channel emissivities.

As discussed previously, emissivity validation and error assessment is not straightforward. Given that the LSM is an operationally used product, well constrained and tested, it makes sense to focus efforts in this area on the physical emissivity modeling component. It is clear from the generally good agreement of 1-2% at frequencies less than or equal to 37 GHz with strict clear-sky retrievals, that LSM output coupled with a physical emissivity model is capable of producing realistic emissivity values in this region. Improvements in the higher-frequency channels and vegetation modeling as well as a better understanding of land surface temperature and penetration depth will lead to a highly valuable tool for understanding microwave land emissivity variability and its relationship to surface parameters.

Chapter 3: Development of a Semi-Empirical Model for Computing Land Surface Emissivity in the Microwave Region

Following the in-depth comparison of emissivity models and retrieved values, it is desirable to develop a technique that makes use of the best information content available from each method, in a physical framework sufficiently simple to be implemented in future passive microwave precipitation algorithms. The result is the semi-empirical model introduced in Chapter 1. The following is published in the journal Transactions in Geoscience and Remote Sensing, and referenced as Ringerud et al. 2014b.

3.1: Input Surface Parameter Datasets

The foundation of the emissivity model presented in this work is the semi-physical model used to compute emissivity at 10 GHz H-pol. The model is based upon the approaches and methods of the LandEM and CMEM models introduced in Chapter 1, and is labeled semi-physical due to its use of empirical parameterizations within a physical modeling framework. The model builds the surface as a 3-layer medium identified as soil, vegetation, and air. Inputs to the emissivity model come via NASA Goddard's Land Information System (LIS), a modular platform for running LSMs with various user-defined input as introduced in Chapter 2. NCEP's Community Noah Land Surface Model, version 3.2, is once again used. Forcing data comes from the North American Land Data Assimilation System project phase 2 (NLDAS-2). MODIS leaf area index (LAI), an 8-day product derived from visible channel spectral reflectance, is also an input to the model in a similar setup to that described in Chapter 2.

Before coupling of the LSM and emissivity model, some consideration is required of the input surface parameters and their compatibility. Soil moisture is extremely important for calculation of the surface dielectric properties. Soil moisture is a function not only of available water, but also of the material properties of the soil that determine its hydraulic conductivity. The dielectric constant for wet soil is calculated using the model of Dobson et al. (1985). For the analysis described here, the static State Soil Geographic Database (STATSGO), compiled by the United States Department of Agriculture, is employed for determination of soil type using percentage of sand, clay, and silt at 1 km resolution. Assumptions are made based upon the soil type regarding grain size and density determining the hydraulic properties of the soil within the model. Use of this type of static database, along with these assumptions about the soil properties will clearly be a source of error in both the dielectric properties of the soil due to texture as well as the soil moisture values, which are themselves highly sensitive to soil properties. Standard output from the Noah model includes a surface layer that is 10 cm thick. Microwave penetration depths in the window channels (10-89 GHz) depend upon many factors, including incidence angle, frequency, soil moisture, temperature, and soil type. The range of these depths for the AMSR-E frequencies is on the order of a couple of centimeters under dry conditions at 10 GHz and decreases to millimeter scale at the higher frequencies (Njoku and Li 1999). While it is not feasible to account for all of the possible variability in penetration depth, it is desirable to improve upon the 10 cm surface layer as input to the emissivity model, particularly as dynamic changes due to surface precipitation and other factors will be magnified in a thin surface layer.

The Noah LSM was subsequently run using an alternate sub-surface layering scheme that includes a top layer of 2 cm. Soil moisture values were compared with those from the standard 10 cm top layer run as well as 5 cm soil moisture measurements obtained from the Agricultural Research Service (ARS) Micronet observational network in western Oklahoma. All 35 available observation sites within the ARS Micronet during the period January 1, 2006 through December 31, 2008, including those from both the Little Washita and Fort Cobb basins are included in this analysis. While all stations are located within the area of western Oklahoma, a diversity of soil types are represented, with sand fractions ranging from 0.17-0.79 and clay fractions from 0.06-0.15. Histograms of soil moisture from the full set of Micronet observations as well as the Noah model at each of the 2 vertical resolutions are shown in Figure 3.1 for the three-year period. It is important to

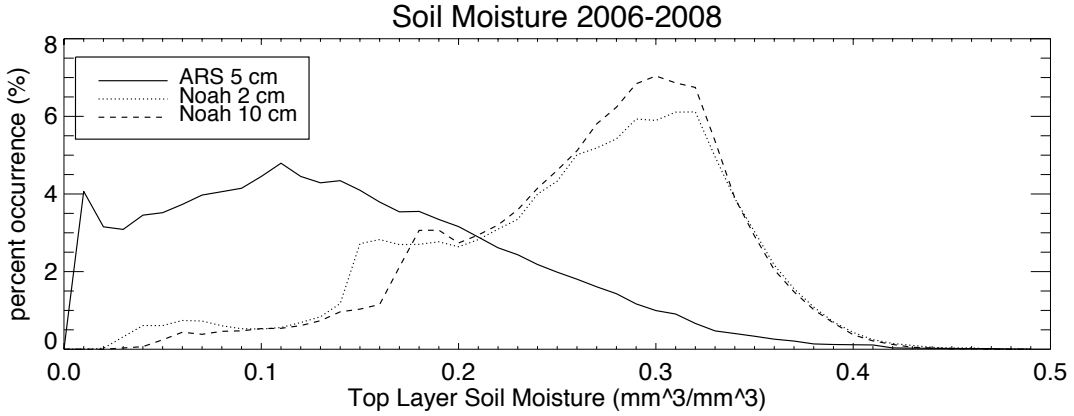

Figure 3.1: Histogram of top layer soil moisture over a three-year period (282,203 data points) at all available ARS Fort Cobb and Little Washita Micronet Stations (solid line) as well as the Noah model soil moisture at the same points from the 2 cm run (dotted line) and 10 cm run (dashed line).

note here that the comparison is between point measurements and model values for 1km grid boxes, as well as at 3 different vertical thicknesses, so while absolute value

comparisons are not necessarily useful, some insight can be gained by looking at differences and similarities. Most striking in the comparison is the presence of significantly lower soil moisture values in the observed data. The Noah values for the 2 cm thickness run are able to get slightly closer to these dry values as the shallow surface is able to dry out more quickly in the shallower layer, but in general the model soil moisture values are similar regardless of layering scheme used here. The large high bias present in both model runs as compared to the observed data at this location, coupled with the higher peaks of the model histograms indicate an inability to match the full dynamic range of the Micronet observations.

Figure 3.2 shows a time series of soil moisture over the year 2007 at a single station (F102) within the Fort Cobb watershed for the ARS 5 cm observations as well as

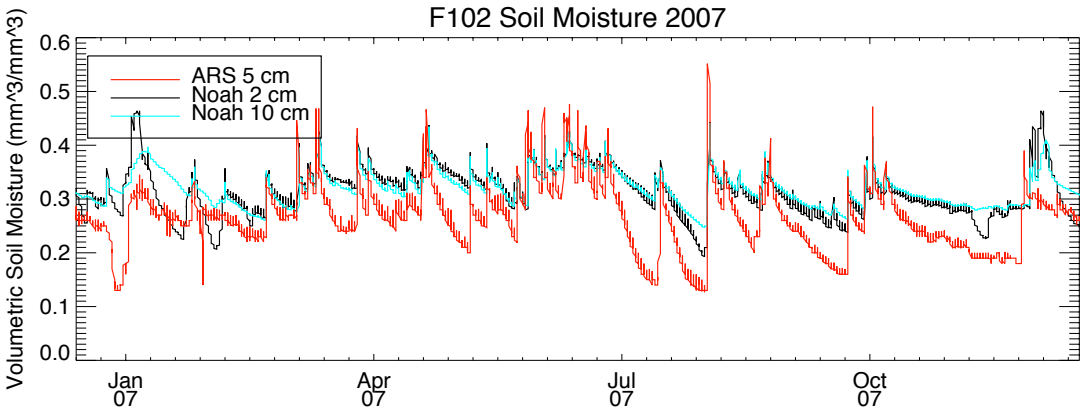

Figure 3.2: Year 2007 time series of volumetric soil moisture at the Fort Cobb Micronet station F102 from observed 5 cm values, along with Noah LSM model values resulting from runs with 2 cm, or 10 cm top layer thicknesses.

Noah model output from the 2 cm and 5 cm layer runs. The wet bias is clearly evident in this single-station context as well. In particular the response to precipitation (positive

spikes in the soil moisture) is very different in the model values. Post-precipitation drying is at a slower rate compared to the observations, and never gets as low as the measured values. This is a problem for the 2 cm data in particular, as it would be expected that the precipitation response (both wetting and drying) would be accelerated for this thin surface layer. The pattern is clearly present and correct in the model soil moisture, but the magnitude appears to be off.

The large bias in soil moisture demonstrated in this area of western Oklahoma is of great concern and clearly warrants further investigation. The Little Washita Watershed has been used in many field campaigns and validation studies over several decades (Cosh et al. 2006). Comparison of soil moisture point observations to larger footprints is a difficult problem, and there will be differences not only in horizontal scale, with possible inhomogeneity within the model grid box, but also differences between the volumetric moisture depth in the model and the actual range of sensitivity from the measurement probes (Owe and Van de Griend 1998). The focus of this paper, however, is not the fidelity of the land surface model, but the simulation of correct emissivities. Disagreements in volumetric soil moisture values, in addition to the inexact comparison, could be a result of incorrect input data, such as rainfall, soil texture, incorrect soil hydraulic physics in the model, or other model problems. As a result of the more physically correct representation of microwave penetration depth as well as the observed slight increase in dynamic range, the 2 cm LSM output is chosen as the basis of input to the emissivity model. Values of soil moisture used in the dielectric mixing model are adjusted in the absence of recent precipitation based upon histogram matching in a purely empirical scheme until the models and input data can be improved.

It is worth noting here that while soil moisture at 2 cm depth is more physically correct for computation of microwave emissivities, it is not a readily available dataset for possible future operational implementation of the emissivity model. It is possible however, to use the coincident model runs done here as a mapping from 10 cm depth (a more commonly available output) to a 2 cm value for emissivity calculation. Data assimilation techniques, such as that described by Reichle and Koster (2004) can easily be implemented for such mapping. The technique matches the cumulative distribution function (cdf) of soil moisture from the two different simulations at each point in the domain. Figure 3.3 shows

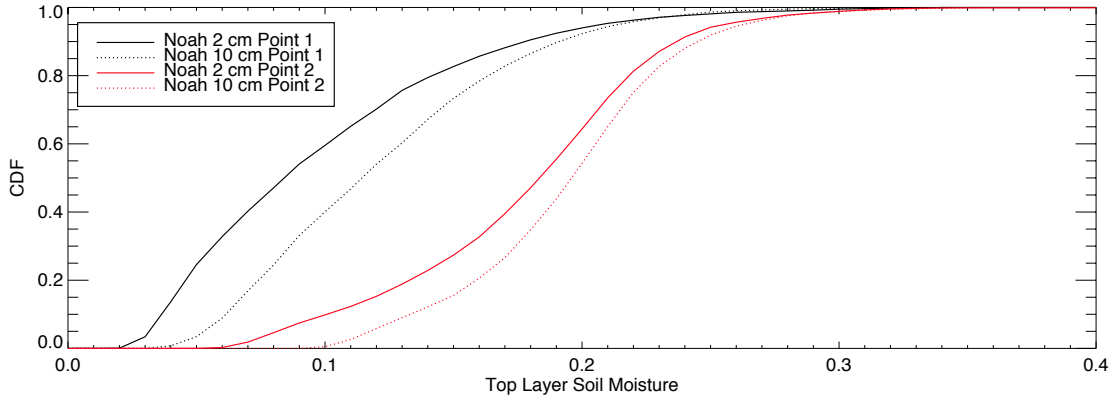

Figure 3.3: Cumulative distribution functions of volumetric soil moisture in the top Noah model layer from the 2 cm (solid lines) and 10 cm (dotted lines) simulations at two points in the SGP domain. Black curves correspond to point 1, a highly sandy soil area in western OK, and red curves to point 2, a point in eastern OK with higher clay content and more vegetation.

an example of the soil moisture cdfs for 2 very different points over the 5-year period January 2004- December 2008. Point 1 is located in southwest Oklahoma and has very sandy soil with STATSGO sand fraction of 0.91 and clay fraction 0.03. The mean MODIS LAI over the 5-year period is 0.75. In contrast, point 2, located in eastern Oklahoma, has a STATSGO sand fraction of 0.14 and a high 0.29 clay fraction. Five-year average LAI at this point is higher at 0.94. The cdf at each point incorporates the static parameters, including

soil type, and also contains the observed variability in dynamic parameters such as the LAI within the distribution over 5 years. The Reichle and Koster technique matching the two cdfs could easily be implemented for future emissivity calculation in cases where only the standard 10 cm layer LSM output is available.

The correct temperature for calculation of emissivity poses a similar problem, as it is also a function of depth. In this case the correct temperature may lie 2 mm below the soil or in the vegetation canopy, depending upon frequency and surface characteristics. Again, it is not feasible to derive the correct temperature in real time, and it is therefore desirable to determine the best choice of temperature from readily available datasets. In the 3-layer physical emissivity model used here, two temperature values are required. One is used to compute emission from the soil, and a separate temperature is used for the layer above containing any vegetation and air. A histogram comparison of top-layer soil temperature from the three sources used in the soil moisture discussion above is shown in Figure 3.4. In

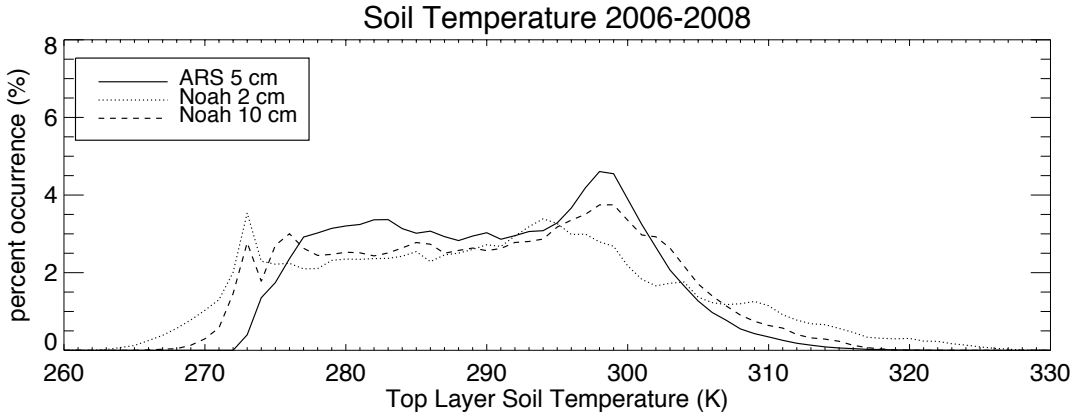

Figure 3.4: Histogram of top layer soil temperature from the three sources shown in figure 1 for the 3-year period 2006-2008 at all available ARS Micronet station within the Fort Cobb and Little Washita watersheds (301,233 data points).

the case of soil temperature, the histograms resulting from the 3 layer thicknesses are quite similar. The 2 cm thickness temperatures show a slightly wider dynamic range on both the high and low ends of the distribution, as would be expected for the shallowest layer with most exposure to the more rapidly changing air interface. This is also evident in the time series comparison for 2007 shown in Figure 3.5. Because of the increased

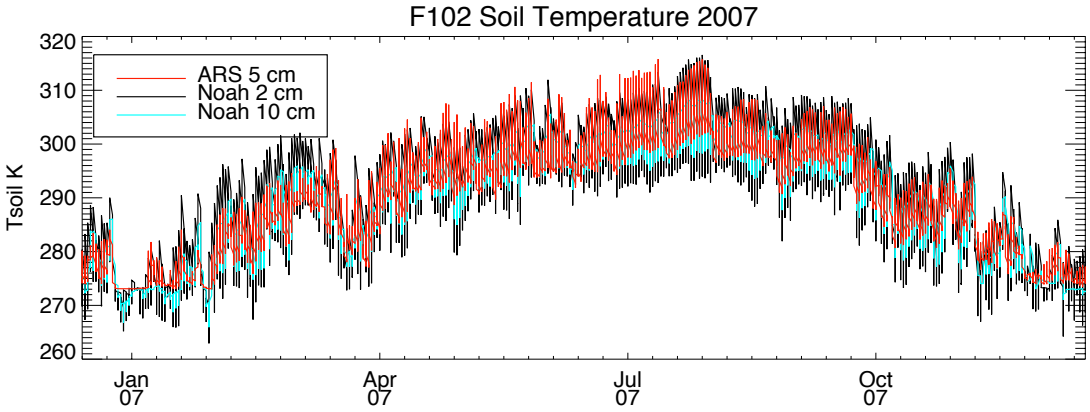

Figure 3.5: Top layer soil temperature at the F102 ARS Micronet station time series over the year 2007 from 3 data sources.

dynamic variability as well as a desire to stay consistent with the soil moisture layering, the 2 cm data will be used as input to the soil dielectric model.

The effective temperature representing the surface in equation (2) will depend upon vegetation type and amount along with other factors. Several input datasets are available from the model. There is the soil temperature as described above, as well as a surface "skin" temperature. The ERA-Interim reanalysis data being used for the atmospheric input in calculating the TOA Tbs also contains a surface temperature.
As an investigation into the effect of using these different temperatures, a simplified surface temperature retrieval is created for analysis. This is not a true retrieval, in that it

assumes that all error in TOA Tb is due to the temperature, but can provide information about the differences in these datasets. The emissivity model is run using a "first guess" surface temperature. TOA Tbs are computed and compared to observed AMSR-E values. If the Tbs differ the temperature is adjusted in an iterative process until the Tbs match within 1K. The "retrieved" temperature is then compared to the available input T datasets. After performing this procedure, it is found that the input temperatures appear consistently to be too low in cold, snow covered cases, and consistently too high in warm, high LAI cases. Between the temperature datasets themselves however, the correlations to "retrieved" temperature are nearly identical (within 0.005) in every case (Figure 3.6), and the

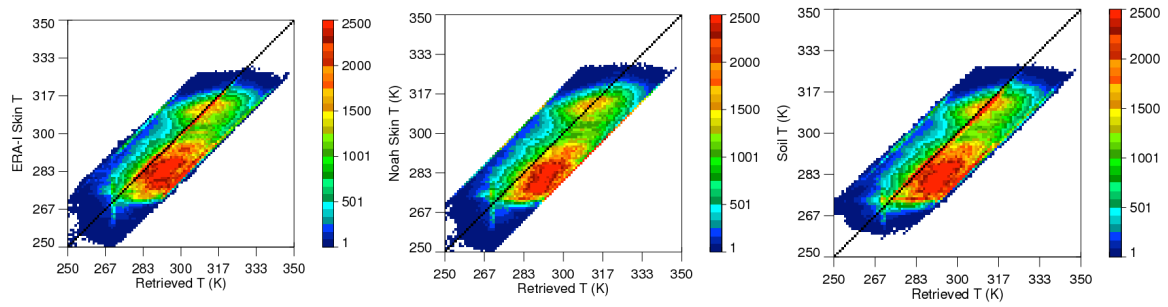

Figure 3.6: Comparison of each temperature dataset (Left: ERA-Interim skin temperature, Middle: Noah LSM surface skin temperature, Right: Noah LSM 2 cm soil temperature) to the adjusted temperature used in "retrieval" to match observed Tb within 1K. Colors indicate data density at each temperature value.

correlations between temperature datasets are all above 0.99. It is clear from Figure 3.6 that using temperature as a "tuning knob" for emissivity retrieval is not the correct solution, and that in the absence of an ideal surface temperature data set, consistency will be the most important factor when comparing observed and retrieved emissivities. The use of the same surface temperature value to both retrieve and model the emissivity will not eliminate any absolute errors in computed emissivities, but ensures that quantitative comparison between the two will eliminate the component of the differences resulting

from use of an incorrect temperature. The Noah surface temperature is chosen as input to both the emissivity model and emissivity retrievals in order to stay consistent in the model realm as well as for ease of implementation.

3.2: The 10 GHz Physical Emissivity Model

Emission from the soil is the product of the soil's temperature and emissivity. The soil emissivity is determined by a combination of a smooth component and a component due to roughness. The Dobson mixing model (Dobson et al. 1985) is used for calculation of the soil dielectric constant. This is a relatively simple and often used semi-empirical model based upon the index of refraction and developed for 1.4-18 GHz. Required inputs are temperature, volumetric moisture, and sand/clay fractions of the soil. The basic parameter relationships of the model are illustrated in Figure 3.7, which plots the model-calculated

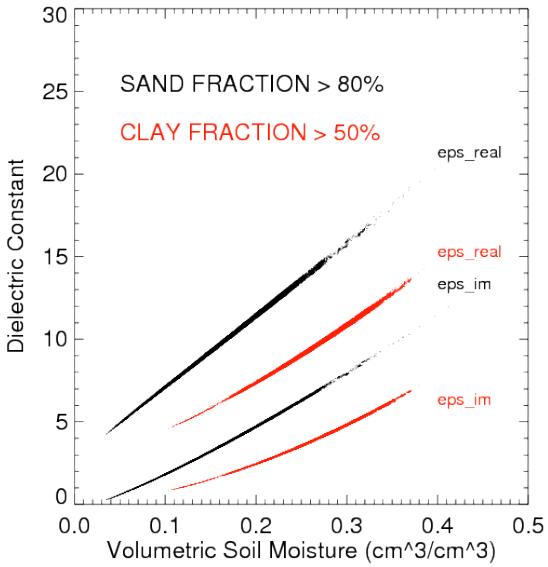

Figure 3.7: Dobson (1985) model calculated 10 GHz soil dielectric constant values for 1 month (June 2004) of data points where T is within 1K of 300K over the 5-degree SGP box. Black points are soil with > 90% sand, red points > 50% clay.

dielectric constant as a function of volumetric soil moisture for one month (June 2004) of SGP model data with surface temperature within 1K of 300K. Both the real part of the dielectric constant ε', which describes the ability of the particles to align with an electric field, as well as the imaginary part ε'', which indicates energy loss, are plotted for 10 GHz. The black data points show this relationship for very sandy soil (sand fraction > 90%, 86,677 data points) and the red points represent soil with a higher clay fraction (greater than 50%, 75,656 data points). In cases of a higher clay fraction, more bound water is present in the soil, decreasing the dielectric constant, whereas sandy soil allows for the presence of free water and has generally higher dielectric constant (Owe and Van de Griend 1998). The air-soil interface smooth surface reflectivity is calculated using Fresnel law. For the rough reflectance, the semi-empirical model of Wegmuller and Matzler (1999), which demonstrated good agreement in the original study with observations at 10GHz, is used. This model is measurement-based and applies to 1-100 GHz. A rougher surface results in higher emissivity values and reduced polarization difference. As stated previously, the roughness height and standard deviation are difficult values to quantify, and are parameterized using historical values for similar surfaces.

Vegetation optical depth is calculated using MODIS LAI and the tau-omega approach of the CMEM model. This routine is based upon Wegmuller et al. (1995) and is formulated for 1-100 GHz. The vegetation layer contributes to the surface emission both positively, via emission from the vegetation itself, and negatively by attenuation of upwelling radiance from the soil layer below. These contributions depend upon the dielectric properties of the vegetation as well as its structure and scattering properties. In the absence of direct knowledge regarding the content and structure of the vegetation, the tau-omega approach

relies upon many assumptions and parameterizations. The vegetation structure and dielectric information is parameterized using typical water content and geometry for crop/grassland vegetation, and quantified by the input of the MODIS LAI product. The water content in this methodology is a function of the LAI, leading to a linear relationship between LAI and 10 GHz vegetation optical depth. The dielectric constant is parameterized as a combination of pure water and dry vegetation mass for a single leaf of assumed thickness. A coefficient is chosen based upon vegetation type (in this case crop and grassland) to represent vegetation structure for calculation of vegetation opacity. The resulting optical depth shows a linear relationship with LAI and increased values as the temperature of the vegetation layer decreases. Figure 3.8 shows this relationship over the

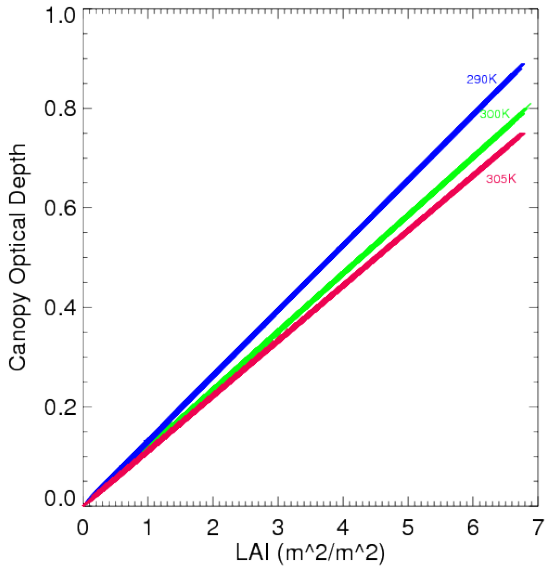

Figure 3.8: Vegetation canopy optical depth values calculated for 10 GHz using the tau-omega approach of Wegmuller et al. 1995. Data is from June 2004 over the full 5-degree SGP box. Colored lines are for 3 different surface temperatures (+/- 0.1K): 290K (blue), 300K (green), and 305K (red).

full 5-degree SGP box over the same month used for Figure 3.7, June 2004, and the colored lines correspond to three surface temperature values (+/- 0.1K). Blue is 290K, green is 300K, and red is 305K.

While the SGP area is not often snow-covered, the physical model used within the LandEM model is included for computing the emissivity of snow-covered surfaces. The model is described in Weng et al. (2001). A parameterized snow particle grain size is used to compute an inhomogeneous dielectric constant of the snow layer using dense medium scattering theory. The snow model defaults to empirical solutions included with the code package in the event of snow depth greater than 10 mm. The empirical solution is derived from satellite retrievals over snow-covered surfaces.

Emissivity is calculated for these layers using the Weng model 2-stream radiative transfer solution. An empirical adjustment is made in cases of recent precipitation as a function of the amount of liquid precipitation having fallen on the surface. The relationship is purely empirical and used was calculated based upon five years of the 2cm layer model comparisons to retrieved emissivity (over 2 million footprint matches). The adjustment value is very simply calculated using the average bias in model emissivities compared to retrieved values as a function of antecedent precipitation calculated from the NLDAS2 dataset over the 24 hours prior to observation. This adjustment is included to account for the change in emissivity due to intercepted water on the vegetation canopy and/or atop the soil layer following recent precipitation. The model is run at 1km resolution, after which the results are averaged to AMSR-E 10 GHz footprint resolution (51x30 km) using a Gaussian averaging scheme. The physical modeling component of the method as described here is basically a modified version of the LandEM model used in CRTM, but in practice any

physical emissivity model found to be optimal for a particular surface type could be employed for this step.

3.3: The Empirical Model

The empirical method described in Bytheway and Kummerow (2010) is next used to map the computed 10 GHz H-pol emissivity to the other AMSR-E channels based upon the covariance of retrieved emissivity at each channel. To develop the empirical model, retrieved clear sky AMSR-E emissivities were used, and the covariance relationships computed between the 10H channel and all others. The retrieval dataset covers 5 years of observations over the 5x5 degree SGP box (over 2 million pixels) and uses the Noah-NLDAS2 surface temperature along with atmospheric information from the ERA-Interim reanalysis in a plane-parallel Eddington radiative transfer scheme. The full dataset of retrieved emissivities was first examined and is plotted in Figure 3.9 as a function of soil moisture and LAI. Gradients in the LAI direction are more prominent at higher frequencies. Gradients in soil moisture space are most visible at lower frequencies and lower LAI. The relationships become unstable around the edges where there is less data available. At higher frequencies, particularly the 89 GHz channels, emissivity generally decreases with increasing LAI, the effect of increasing roughness being most prominent for the smallest wavelength. At the lower frequencies, variability is strongest in soil moisture space, indicating the greater importance of the dielectric contribution and penetration depth at these longer wavelengths.

Covariance relationships are compiled relating the 10 GHz H-pol frequency to all other AMSR-E channels. The correlation coefficients for these relationships are given in Table 3.1, along with the correlations when binning emissivities by LAI and soil moisture. The relationships clearly improve when the binning technique is used, and these covariances are therefore used to compile the empirical emissivity model.

The covariance relationships, though calculated empirically, contain information about the surface characteristics within each distribution. As an illustration of this, Figure 3.10 plots the covariance relationships over the full 5-year dataset for four combinations of

Table 3.1: Retrieved emissivity correlations with respect to the 10.65H channel for AMSR-E channels over the 5-year period 2004-2008 (2.2 million pixels). Correlations are given with and without binning of the data by soil moisture and LAI.

Channel	r-NO BINS	r-BINS
10.65V	0.84	0.91
18.7V	0.74	0.87
18.7H	0.91	0.91
23.8V	0.60	0.83
23.8H	0.81	0.89
36.5V	0.56	0.80
36.5H	0.68	0.77
89.0V	0.32	0.67
89.0H	0.40	0.68

LAI and soil moisture between the 10.65H and three other AMSR-E frequencies. Snow covered pixels have been excluded. The top two rows in Figure 7 are for points with a lower-than-average LAI of 0.5, and the bottom two rows for higher-than average LAI of 3.0. The first and third rows are points with a lower-than-average soil moisture of 0.2, and the second and third higher-than-average soil moisture of 0.3. The 10.65 H emissivities are compared to three different AMSR-E frequencies. The left column is 18.7 GHz H, center

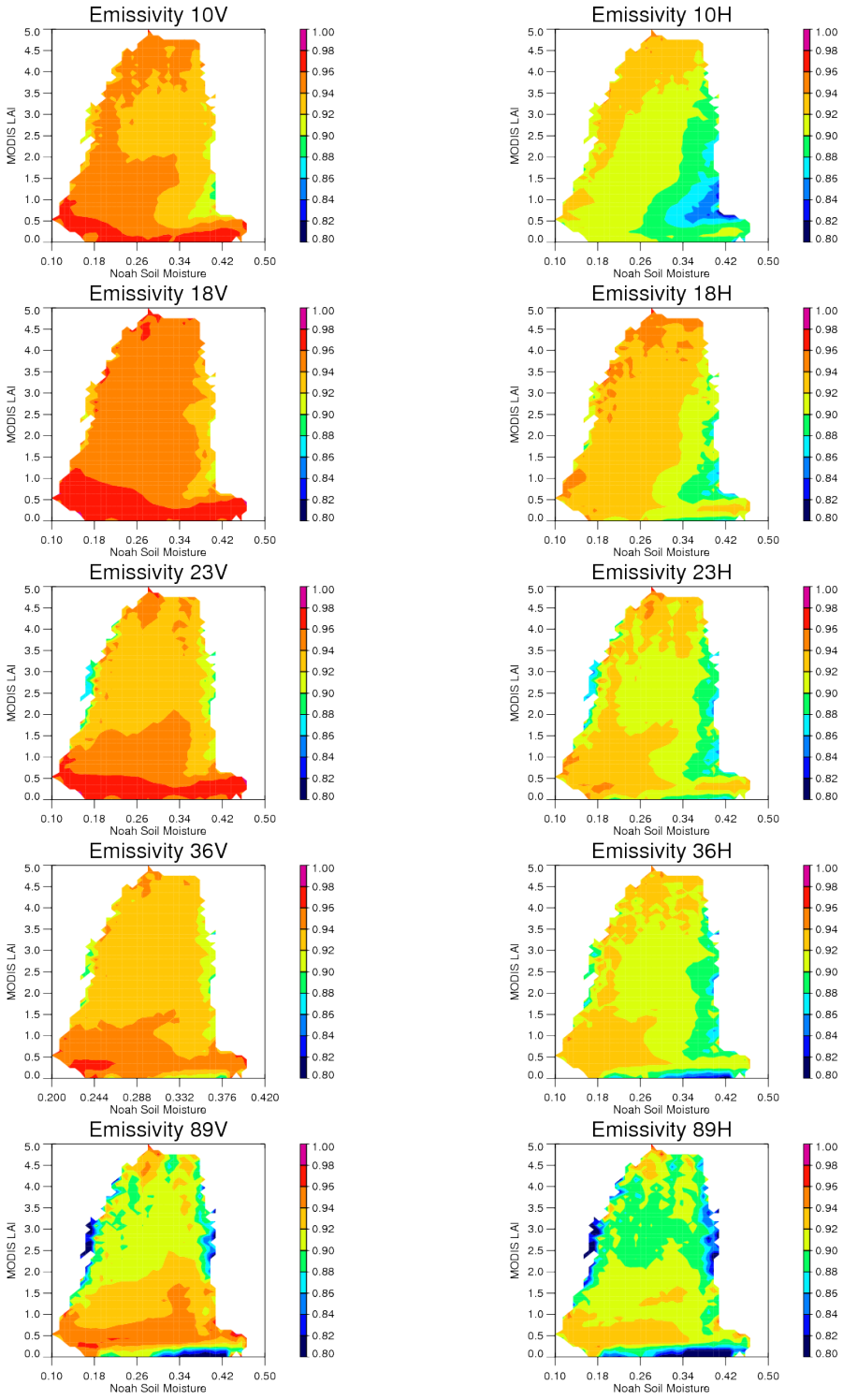

Figure 3.9: Color contours of 2004-2008 retrieved AMSR-E emissivity as a function of LAI and soil moisture for the 5-degree SGP box.

column 36.5 GHz H, and right column 89.0 GHz H. The number of observations within each bin varies from 348 for the high LAI, low soil moisture case, to 30,790 for the low LAI, high soil moisture case. The colors on each scatter plot divide the temperature at an average value of 285K for the top plots and 300K for the bottom, higher LAI cases, with the colder temperatures in blue. In the lower 18.7 GHz frequency (left column), the differences between the two soil moisture bins are noticeable, with emissivities extending to lower values at higher soil moisture, as would be expected. The slope of the covariance also varies between bins. While this dimension of variability is being constrained via the binning process, each bin clearly shows a range of dependence on temperature within the bin, visible as delineation between blue and red points along the line of each covariance relationship. Higher temperatures (red points) lead to lower emissivities in each channel for all bins shown. At the higher frequencies, there is a more noticeable change in slope as LAI varies, illustrated by the differences in the 36.5 GHz and 89.0 GHz plots in the top two rows (low LAI) versus the bottom two rows (high LAI). There is a clear issue, magnified with increasing frequency, with lower emissivity cases, particularly at the higher LAI value, as data points trail off vertically downward. A likely explanation for this issue is that cloud contamination exists in the retrieved dataset. Validation studies analyzing the MODIS 1KM cloud mask product used here in comparison to coincident cloud-aerosol lidar observations indicate that detection agreement between the two has a rate of 75%, and over the SGP area in particular, the MODIS product tends to miss high clouds (Holz et al. 2008). To investigate the effects of high, thin clouds on the AMSR-E frequencies in this area,

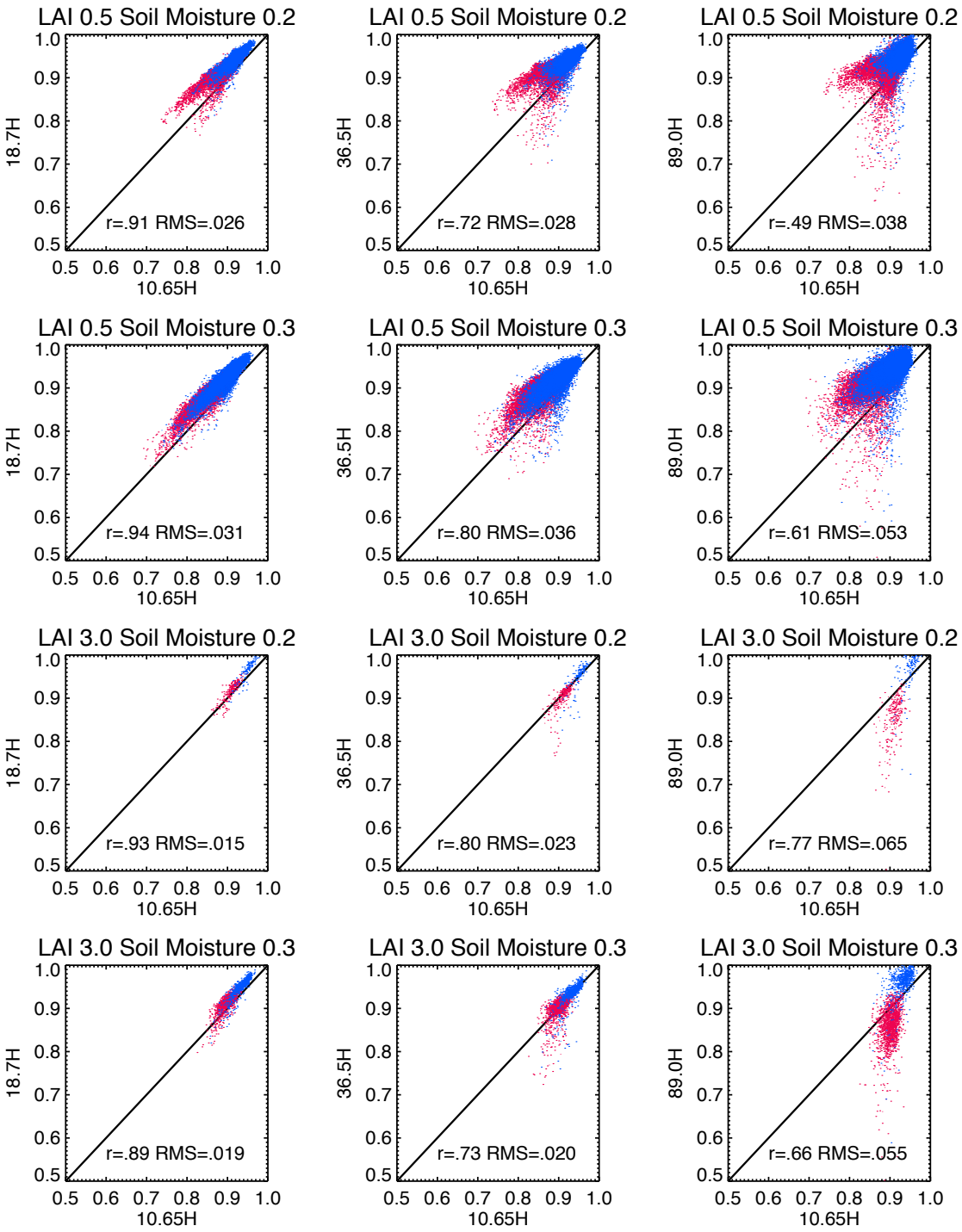

Figure 3.10: Covariance relationships between the 10.65 GHz H and 18.7 GHz H (left column), 35.5 GHz H (middle column), and 89.0 GHz H (right column) AMSR-E channels for LAI = 0.5, soil moisture = 0.2 (top row), LAI=0.5, soil moisture = 0.3 (second row), LAI = 3.0, soil moisture = 0.2 (third row), and LAI = 3.0, soil moisture = 0.3 (bottom row). Blue color denotes data points with colder than average (300K for high LAI, 285 K for lower LAI) temperature, and red colors warmer than average temperatures.

a single-column radiative transfer model is employed, along with average SGP emissivity values and a clear atmosphere. Addition of a thin, high liquid water cloud is found to decrease Tbs at all AMSR-E frequencies, with the decrease at 89 GHz H-pol 25 times larger than the decrease at 10 GHz H-pol. Recalling Equation 2, a lower 89 GHz Tb at the same surface temperature and under the same assumed atmosphere yields and artificially low emissivity at that frequency, and would yield the vertically trailing points present in Figure 3.10. An attempt to correlate this issue with model TPW and other available atmospheric parameters yielded no connection, so this remains an area for future improvement, and suggests that the dataset used for creation of an operational model will require highly reliable cloud clearing.

The resulting unique model utilizes the semi-physical 10 GHz emissivity model and surface parameter dataset from the LSM output, in combination with the set of covariance relationships based upon retrieved emissivities and stratified by LAI and soil moisture. The model itself is simply a table of coefficients describing the covariance relationships shown in Figure 3.10 for each LAI/soil moisture bin. For comparison to satellite observations, Tbs are calculated for the top of the atmosphere (TOA) using the resulting emissivities and coincident atmospheric information from the ERA-Interim reanalysis (described in Dee et al. 2011). The modeled emissivities along with atmospheric profiles of temperature and water vapor obtained from the reanalysis are input to a plane-parallel radiative transfer scheme to calculate the TOA Tbs. The model is run over the SGP box for a two-year period independent of the years used for compiling the empirical model. Results are presented and discussed in section 3.4.

3.4: Semi-Empirical Model Results and Analysis

The emissivity results are first examined in the context of the surface parameter fields. Figure 3.11 plots skin temperature from the Noah LSM in the upper left panel, MODIS LAI in the upper right, Noah 10 cm soil moisture lower left, and total precipitation over the previous 24 hours on the lower right panel, all at the 1KM LSM resolution for the 5-degree grid box at 0Z on July 1, 2009 or 7PM local time. The Oklahoma state southern boundary is outlined and visible on the lower left, with the horizontal line between latitude 36 and 37 indicating the Kansas-Oklahoma border. This is a diverse and non-homogeneous domain, with the west side clearly warmer and drier with low levels of vegetation as indicated by the MODIS LAI values. The urban areas of Witchita, Oklahoma City, and Tulsa are evident in each field, exhibiting typical urban heat island higher temperatures, as well as very low LAI. The minima in soil moisture on the western side of the domain follow areas of higher elevation and very sandy soil. Precipitation over the previous 24 hours is concentrated in southern and western Oklahoma. Figure 3.12 shows the simulated emissivities for the same time step for 10 AMSR-E channels. The simulated emissivities in this scene vary with the surface parameters as would be expected using physical arguments about the differences in the surface states. Spatial patterns in the higher frequencies are very similar to the map of LAI, indicating the importance of surface roughness due to vegetation effects on emissivity at these frequencies, with increased vegetation optical depth corresponding to high emissivity values. The green area of reduced soil moisture in the northern part of the box is associated with higher emissivities. Lower emissivities, particularly in the H-pol channels, are associated with the highest soil

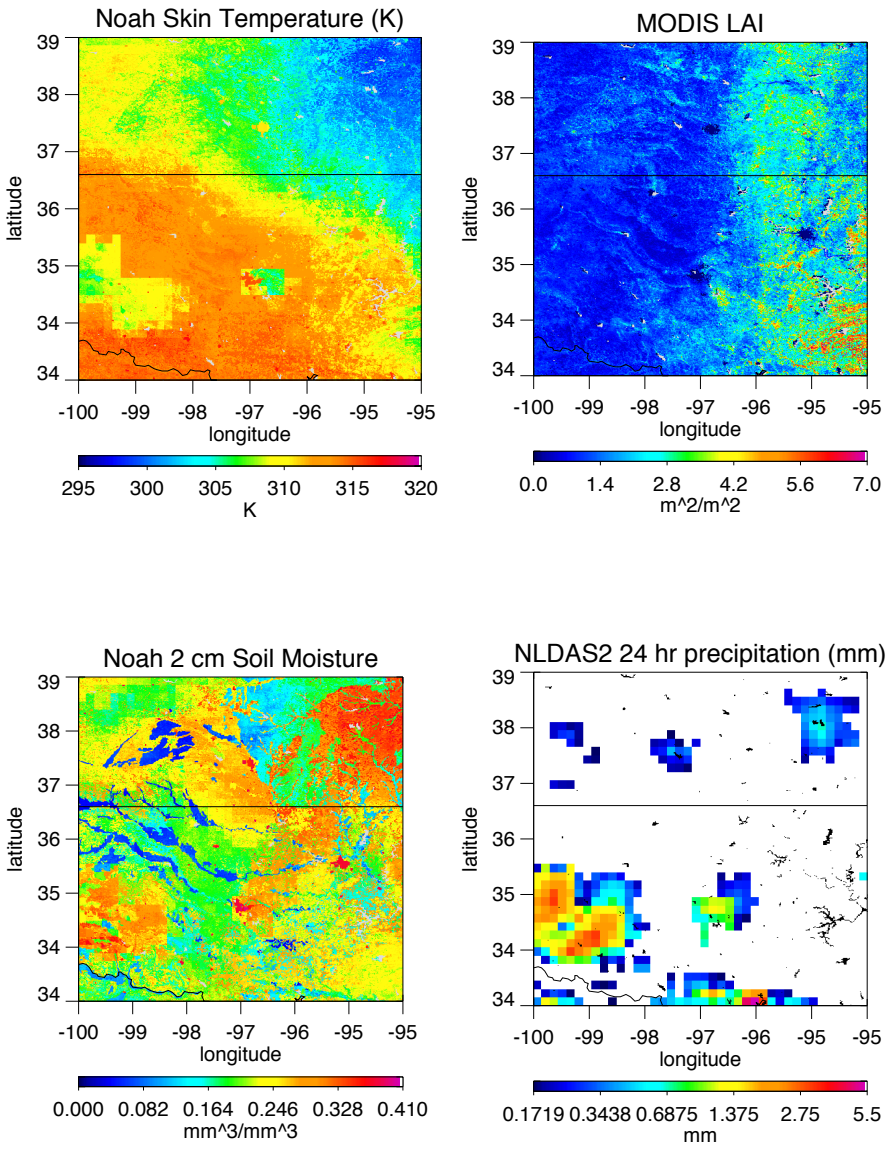

Figure 3.11: Noah skin temperature, MODIS LAI, and Noah 2 cm soil moisture for 0Z July 1, 2009 mapped over the full 5-degree SGP box.

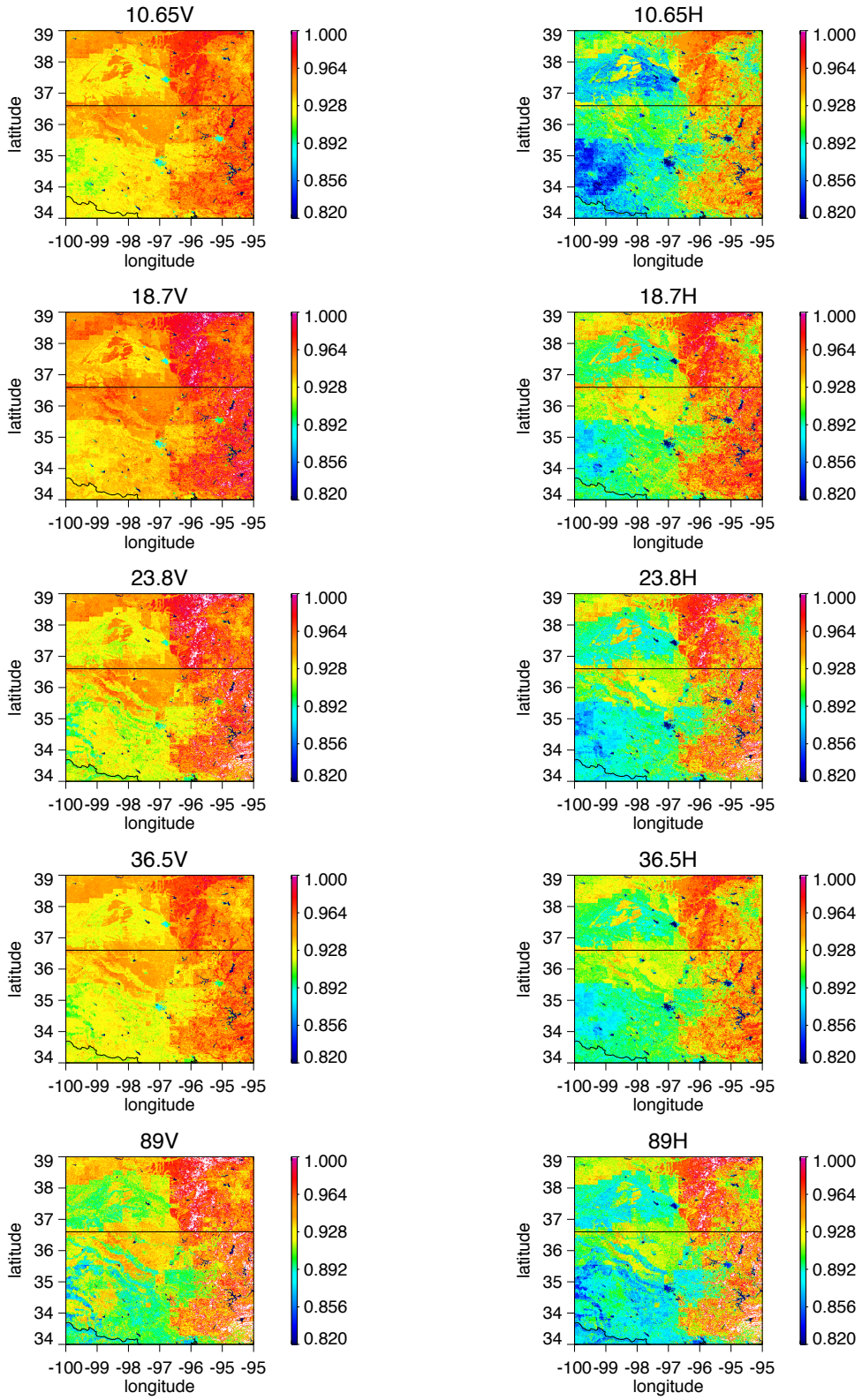

Figure 3.12: Maps of simulated emissivity at 10 AMSR-E channels over the SGP box for the time step pictured in figure 3.11.

moisture values in the far upper right as a result of the increased dielectric constant as soil moisture increases. The area of lowest emissivity is associated with likely water on the surface in the areas of recent precipitation in southwestern Oklahoma. The urban areas are easily visible as relative minima at each frequency as a result of the high temperatures and low LAI, both associated with an increase in emissivity.

In order to more quantitatively assess the performance of the emissivity model, the simulated clear-sky brightness temperatures are next compared with observed values. Scatter plots comparing Tbs modeled using the methodology described in the previous section are shown in Figure 3.13 (left) for all cloud-free pixels over the full 5-degree SGP box during the two-year period Jan 2009-Dec 2010. Table 3.2 gives the associated error statistics relative to the observed AMSR-E Tbs for the period including all cloud-free matches in the box, or 910,111 data points. Correlations range from 0.85-0.93 and biases are less than 1K with the exception of the 89 GHz channels at 1.25K. It is worth noting that one of the lowest correlations is for the 10 GHz H-pol channel, which is the semi-physical model. This suggests that future improvements in the physical model would help in increasing general agreement here. The most obvious area of disagreement is visible in the 89 GHz plots, involving observed Tbs much lower than those modeled. These points were thoroughly investigated for correlation to the surface or atmospheric parameter fields used here, and no such correlations were found, other than that they tended to be from afternoon (around 1PM local time) overpasses. This is directly related to the relative lack of correlation in the covariance relationships at these high frequencies and lower emissivities as shown in Figure 3.10. As discussed in the previous section, it is likely that this is a result of cloud contamination in the retrieved emissivities used in constructing the

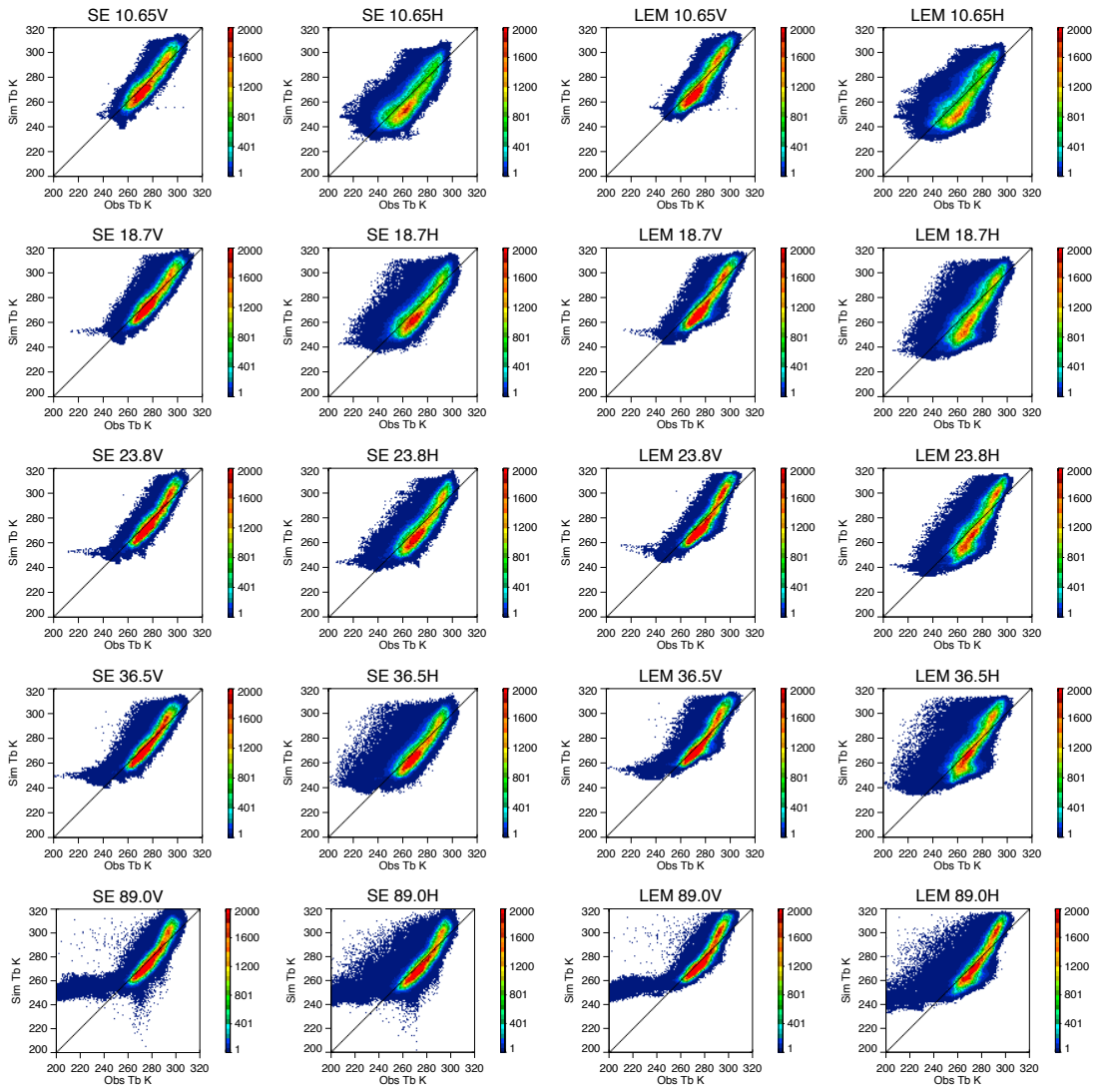

Figure 3.13: Comparison of modeled and observed Tbs for all 877,847 cloud-free pixels over the 5-degree SGP box for the 2-year period 2009-2010 using the semi-empirical model (SE) on the left, and the CRTM LandEM physical model (LEM) on the right for all frequencies. Colors indicate the density of data points at each Tb.

covariance relationships and in computing the Tbs. In particular, points that exhibit disagreement only in the 89 GHz frequency may include optically thin ice clouds, as this is the only AMSR-E frequency with ice sensitivity. Figure 3.13 (right) and Table 3.2 contain the same information for a parallel run using the LandEM version 2.1 for physical emissivity calculation in all 10 channels. The semi-empirical model yields a cleaner looking

Table 3.2: Error statistics for the semi-physical model (top) and CRTM LandEM model (bottom) relative to observed AMSR-E brightness temperatures for all SGP cloud-free pixel matches (910,111 total) during the period 2009-2010 using the semi-empirical model.

Semi-Empirical	10.65V	10.65H	18.7V	18.7H	23.8V	23.8H	36.5V	36.5H	89.0V	89.0H
Correlation	0.93	0.85	0.93	0.87	0.94	0.90	0.93	0.86	0.88	0.85
Mean bias (K)	0.71	-0.060	0.51	0.20	0.78	0.45	0.87	0.66	1.25	1.25
RMS	0.009	0.010	0.005	0.004	0.002	0.0006	0.0007	0.003	0.009	0.013

CRTM LandEM	10.65V	10.65H	18.7V	18.7H	23.8V	23.8H	36.5V	36.5H	89.0V	89.0H
Correlation	0.91	0.81	0.92	0.84	0.93	0.88	0.91	0.83	0.87	0.85
Mean bias (K)	-0.92	-1.76	-3.67	-4.60	-1.01	-0.82	0.82	1.00	1.24	0.82
RMS	0.013	0.015	0.012	0.017	0.006	0.010	0.002	0.007	0.007	0.006

relationship, with correlations improved by 0.02-0.04 and significantly reduced biases with the reduction ranging from 0.2 to several Kelvin in multiple frequencies (Table 3.2).

Figure 3.14 shows the Tb comparison plot for cases with LAI values less than 0.2 and non-frozen soil (1416 data points). This is relatively bare and gives an indication of the performance of the Dobson semi-empirical soil model performance. There is greater scatter in the lower frequencies for these points, indicating that the soil modeling can be

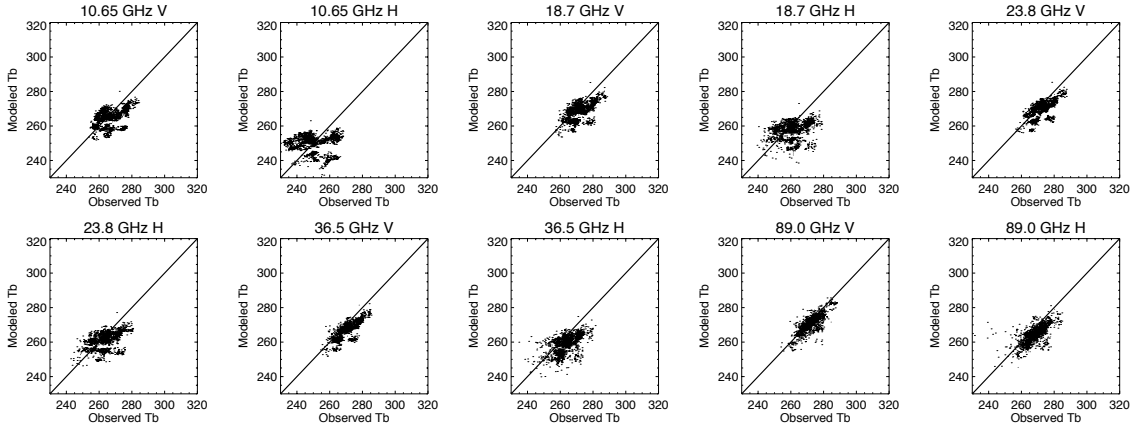

Figure 3.14: Same as figure 3.13, but for cases with LAI < 0.20 and soil temperature > 275K.

improved upon, particularly by improving input data and its mapping to the frequency-specific depth. Figure 3.15 shows agreement for the most highly vegetated areas, with

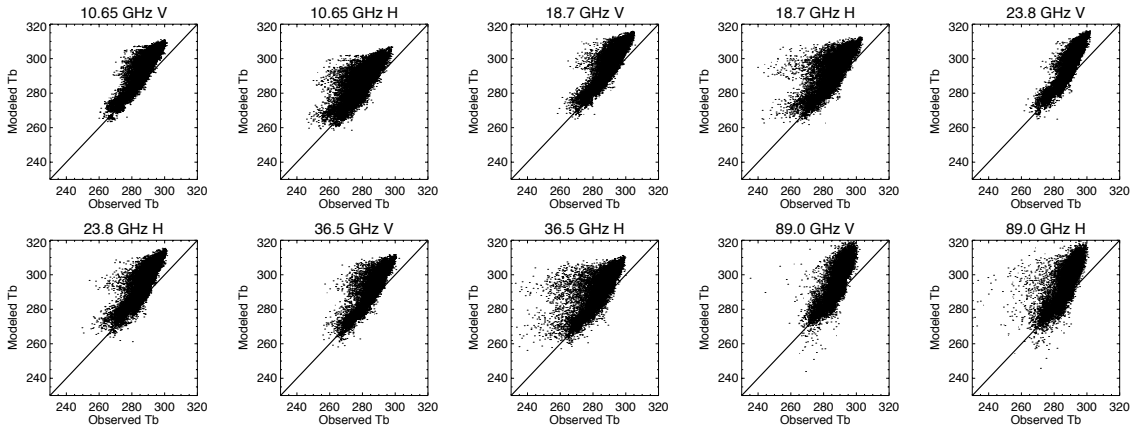

Figure 3.15: Same as Figure 3.13 but for cases with LAI > 3.0 (15,087 data points).

LAI > 2.0 (15,087 points). A high bias is clearly evident in this case, amplified at the higher frequencies. As discussed in section 3.2, the vegetation component of the physical model involves a large number of assumptions and parameterizations. Errors in these assumptions as well as problems in determining the correct radiative temperature for the most vegetated surfaces likely contribute to the scatter and bias here.

The sensitivity of the model to the choice (and availability) of surface parameters is of interest, as future implementation into a physical precipitation retrieval algorithm will likely require *a priori* datasets with availability and accuracy that varies by location. Soil moisture, with its large influence on emissivity, is well measured in parts of the US, but such datasets are not available over the African Savanna, where soil moisture might come from a satellite retrieval technique. The 5-degree box used here was chosen partially as a result of the density of available high-quality hydrological and meteorological data and its past use in numerous validation and field campaigns (e.g. Jackson et al. 1999). In order to

investigate the effect that input data might have on model development, the semi-empirical model is run for the 2009-2010 period with no changes to the emissivity model, but using as soil moisture input the top layer value from a Noah model run using the standard operational depth of 10 cm for the calculations. The resulting biases with respect to the observed AMSR-E Tbs are given in Table 3.3 for 91,070 footprints over the 5-degree box in

Table 3.3: Mean Tb bias (simulated-observed) over the full 5-degree SGP box for the years 2009-2010, calculated using the semi-empirical model and ingesting Noah model soil moistures from both the 2 cm (top row) and more standard 10 cm (bottom row) model runs.

	10.65V	10.65H	18.7V	18.7H	23.8V	23.8H	36.5V	36.5H	89.0V	89.0H
2 cm Mean Bias (K)	0.71	-0.060	0.51	0.20	0.78	0.45	0.87	0.66	1.25	1.25
10 cm Mean Bias (K)	-1.05	-2.91	-0.89	-2.01	-0.62	-1.32	-0.36	-0.95	0.34	-0.15

the two-year period. The use of the lower-depth soil moisture data introduces a clear negative Tb bias in the physical modeling stage (10.65 H channel), which is then translated to the other frequencies through the covariance relationships. This is due to the somewhat wetter soil conditions at this depth as shown in the histogram of Figure 3.1 and the decreased post-precipitation drying demonstrated by the time series in Figure 3.2. Correlations for the 10 cm case follow the same pattern with values 0.01-0.03 less. Although in this context it is not possible to diagnose the exact source of error in the final calculated Tb values, the increased agreement demonstrated by this analysis lends further support to the use of the more physically correct 2 cm depth input for emissivity calculation. This also illustrates that future geographical expansion of the emissivity model

will require investigation into the availability of accurate soil moisture data and its mapping to the shallower depth.

3.5: Semi-Empirical Model Discussion and Conclusions

A semi-physical emissivity model at 10 GHz in combination with an empirical covariance mapping to other passive microwave frequencies shows promise for generating realistic emissivities over the SGP area, reflecting dynamic changes in the input surface parameters. By using the simulated emissivities in combination with a model atmosphere and radiative transfer scheme, top of the atmosphere brightness temperatures can be calculated for comparison to observed satellite Tbs for cases where the atmosphere is cloud-free and the bulk of the signal is coming from the surface. Biases in simulated clear-sky brightness temperatures with respect to observed brightness temperatures are less than 1 K except at the 89 GHz frequency, where it is 1.25. RMS errors are less than 0.0013 and correlation coefficients range from 0.85-0.93, with the closest agreement at the lower window channel frequencies. Dynamic inputs required for the model are soil moisture, leaf area index, skin temperature, and antecedent precipitation, not unreasonable ancillary data for a global retrieval algorithm. Soil moisture is the most dynamic of these parameters, and implementation using input datasets with lower temporal and/or spatial resolution will have to be investigated for the errors introduced. A closer look at near-bare soil cases as well as highly vegetated pixels show that there is room for improvement in the soil and vegetation modules of the semi-physical 10 GHz model. One highly desirable quality of this modular-type scheme is that any portion can be continuously improved, optimized, and updated, as the various areas of the algorithm are better understood. An improved canopy

optical depth module, for example, can easily be "plugged in" for quick implementation into the full model. Changes in input surface parameters at the 10% level introduce biases of roughly 1-3K, illustrating the need for reasonably accurate input data.

A limitation of the current results is that they apply strictly to only a small five-degree box, though this box does contain a wide range of vegetation and soil moisture combinations, as well as some topography differences and seasonal temperature and vegetation changes. Current ongoing work involves expanding this approach to similar surface types and eventually to completely different surface types using the same methodology but perhaps different parameters. For example, over desert areas a LAI/soil moisture database may not make sense, but the methodology could still be applied using more appropriate parameters to be determined, such as surface temperature and soil texture. In areas of very complex terrain, such as coastlines or mountain ranges, this more physical approach may not be feasible, though advances in modeling of complex terrain and improved radiative transfer in such areas may make the approach possible. The promising results demonstrated here for the SGP surface type certainly suggest that there is value in further extension, exploration, and optimization of the semi-empirical model.

Chapter 4: Constructing the Physical Database

The semi-empirical emissivity model developed in Chapter 3 is next implemented, together with atmospheric information derived using collocated active-passive observations from the Tropical Rainfall Measurement Mission (TRMM) satellite, for the construction of a physical database for use in Bayesian precipitation algorithms. As the performance of a Bayesian scheme is a direct function of the quality of the database used, the database created using the dynamic semi-empirical model will be compared to one using climatological emissivity values in order to assess value added. In Kummerow et al. 2011, the construction of such a database is described for ocean surfaces. The scheme utilizes a combined retrieval technique, where liquid precipitation profiles are derived from the active PR measurements. Constrained matching of observed radar profiles to cloud resolving model profiles supplies the information regarding liquid below the sensitivity of the PR as well as ice profiles. Adjustments are made to the hydrometeor drop size distribution, which, while remaining constrained to match the PR, are adjusted to be radiometrically consistent with TMI Tbs.

The methodology is similar to that employed over the ocean in operational physical precipitation retrievals as described in Kummerow et al. 2011, with the addition of the semi-empirical emissivity model for calculation of the surface contribution. Due to the relatively higher importance of ice scattering signal for retrieving precipitation over land, a simple scheme is added to improve the characterization of ice concentrations while remaining radiometrically consistent with observed Tbs. Similar to the techniques employed over ocean, the database is constructed at the location and resolution of a PR

pixel. Only the center 11 near-nadir PR pixels are used in order to minimize the influence of surface clutter. The 5-degree SGP box is again used as the study area to determine the feasibility of the physical scheme.

4.1: The Semi-Empirical Emissivity Model for TMI

While the emissivity modeling system developed in Chapter 3 demonstrated the success of the semi-empirical technique in calculating emissivities in the SGP area, the results shown there were specific to the footprint resolution, overpass times, and frequencies of the AMSR-E radiometer. The process is repeated here for TMI-specific parameters.

The physical model described in Chapter 3 is again used for calculation of the 10.65 GHz H-pol emissivity, in the identical framework used for AMSR-E. Surface information, including soil moisture, LAI, and surface temperature, is as described in Chapters 2 and 3. The physical emissivity model is run at the footprint resolution of the TMI 10 GHz channel.

The empirical emissivity model is constructed using MODIS confident-clear cloud-free footprints, ERA-Interim atmospheric information, and the iterative emissivity retrieval scheme described in Chapter 2, in this case using Tbs from the TRMM TMI. Unlike AMSR-E, the TMI instrument does not fly in a sun-synchronous orbit, yielding increased information about the diurnal cycle. This does limit coincident overpasses with MODIS (which was kept for cloud-clearing purposes in order to assure consistency with the earlier work) as compared to AMSR-E and, together with a smaller orbit extent, this yields a smaller dataset for construction of the empirical retrieval. The database, created using retrievals within the SGP box for the 5-year period 2004-2008, contains 322,217 TMI pixels. The smaller

sample size does not affect the resulting relationships, however. Figure 4.1 shows the retrieved emissivities at each frequency as a function of soil moisture and LAI. Table 4.1 gives the associated channel correlations for TMI. Comparing these with Figure 3.17 and Table 3.1, the physical relationships between emissivity, LAI, and soil moisture at each frequency are clearly the same for each sensor, and the correlations between the 10.65 H and all other channels nearly identical, with slightly higher correlations for the slightly different frequencies and slightly larger footprint sizes of the TMI dataset.

Table 4.1: Retrieved emissivity correlations with respect to the 10.65H channel for TMI channels over the 5-year period 2004-2008 (322,217 pixels). Correlations are given with and without binning of the data by soil moisture and LAI.

Channel	r-NO BINS	r-BINS
10.65V	0.88	0.93
19.35V	0.78	0.87
19.35H	0.91	0.89
21.3V	0.69	0.82
37.0V	0.67	0.82
37.0H	0.77	0.79
85.5V	0.47	0.71
85.5H	0.53	0.69

The covariances relationships mapping 10.65 GHz H-pol emissivities to each of the other TMI channels are again constructed as a function of LAI and soil moisture bin using the retrieved emissivity values at each frequency and polarization. For construction of the physical database, the semi-empirical model is used to calculate emissivity in the forward radiative transfer calculations for each pixel. Input surface data is from the Noah LSM as described in Chapter 2. It should be noted that, as the NLDAS-2 forcing data used here includes information about current precipitation, the input soil moistures reflect that precipitation through the model values.

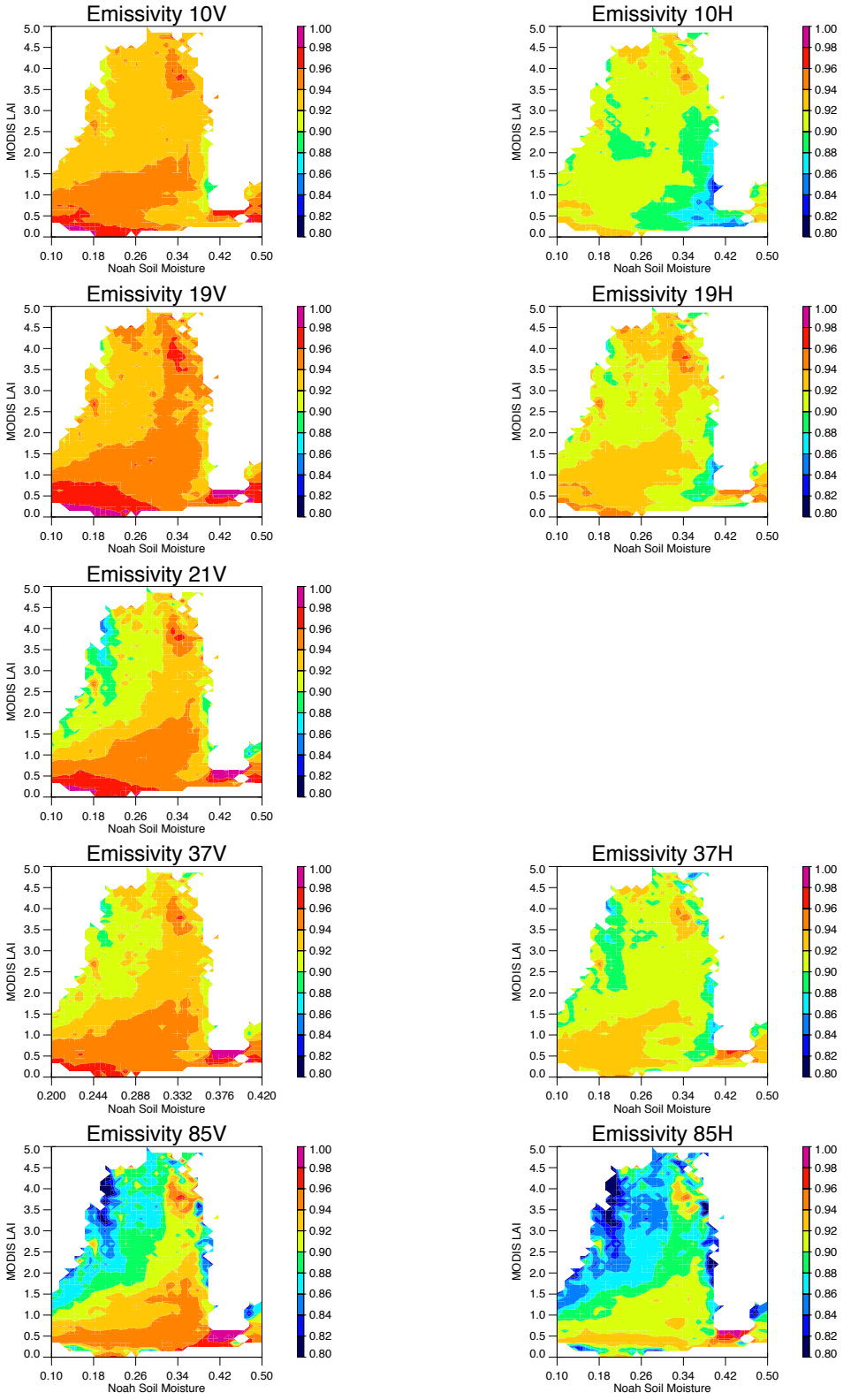

Figure 4.1: Color contours of 2004-2008 retrieved TMI emissivity as a function of LAI and soil moisture for the 5-degree SGP box.

4.2: Ancillary Atmospheric Data

For construction of the physical database, all surface and atmospheric parameters affecting TOA Tb must be included for radiative transfer. While the use of the PR as a coincident active sensor contributes information regarding size and concentration of hydrometeors in the column, it does not have sensitivity to many other TMI-sensitive parameters, including ice and cloud water. These parameters must therefore be obtained elsewhere. The ERA-Interim reanalysis, described previously as applied to the clear-sky emissivity retrievals, is used for the background temperature and water vapor profiles, atmospheric pressure, and cloud water in non-raining areas. This ancillary data is collected for each 4 km PR pixel, which will define the resolution for the final radiative transfer computations.

While the addition of ancillary data is necessary for full column radiative transfer modeling, there are caveats involved with the use of the reanalysis data here. The resolution in time and space (6 hourly, ¼ degree) is coarse compared to the instantaneous satellite overpass. Clouds in particular will differ significantly on these scales. While the microwave window channels are sensitive to these parameters, the sensitivity is small compared to that of the surface emissivity, which comes from the semi-empirical model, and liquid hydrometeors, which will be derived using the PR observations. As the purpose of creating this database is not for implementation into an operational algorithm but assessment of sensitivity to characterization of the surface emissivity, use of the reanalysis as background environmental information is deemed sufficient.

4.3: Hydrometeor Profiles

In order to remain radiometrically consistent, hydrometeor profiles in the database must have associated reflectivity that matches each observed PR profile. While standard PR products contain information about rain water amounts derived using assumed drop size distributions, the PR does not have much sensitivity to ice above the freezing level, which is important for calculation of higher frequency Tbs. For this reason, model hydrometeor profiles are used for partitioning of hydrometeor species for each raining profile. Matching with a model profile is constrained by local atmospheric conditions as well as the requirement of a match with the profile in reflectivity space. The matching procedure is defined in detail below.

The model hydrometeor profiles used here are taken from one year of simulations over the continental United States using the Goddard Cumulus Ensemble (GCE) model with spectral bin microphysics run as part of the NASA Multiscale Modeling Framework (MMF). The cloud-resolving model utilizes a bin microphysical scheme with 33 size bins, simulating size spectra of seven hydrometeor types and explicitly representing microphysical processes of all phases (Li et al. 2010). Model resolution is equal to that of the TRMM PR footprint, at 4 km. The one-year period yields 16.8 million raining profiles. In order to keep data size manageable, every 5^{th} profile is kept for potential use in the profile database.

For each hydrometeor profile, reflectivity as would be seen by the PR is calculated. A determination of whether each profile is convective or stratiform is first made using the partitioning technique of Lang et al. 2003. For stratiform profiles, sub-layers are created near the melting layer, as described in Masunaga and Kummerow 2005, in order to better

represent the melting layer and resulting bright-band in reflectivity. Drop size distribution is assumed to be that used in the operational PR rainfall algorithm (Iguchi et al. 2000). Attenuation through the volume at the PR frequency is calculated, and the reflectivity profile is adjusted to replicate the attenuated signal that would be observed by the PR. For each reflectivity profile, associated profiles of other hydrometeor species, as well as information about the background environment, are stored in the database.

For each raining PR profile used in construction of the physical database, a constrained matching is performed. PR reflectivity profiles are compared to computed reflectivity profiles from the CRM, constrained using similar total precipitable water (tpw), near-surface liquid water content, and freezing level. The use of constraints ensures the most physically consistent conditions for each profile match. The closest match in reflectivity space is chosen, with portions of the profile below the freezing level weighted most heavily in the matching process, as PR sensitivity is highest for precipitation-sized, liquid hydrometeors. The profiles of all other hydrometeor species, including cloud water, snow, graupel, and hail are assigned to each PR pixel based upon the reflectivity profile match.

4.4: Radiative Transfer and Ice Adjustment

Following assignment to each PR pixel of background atmospheric information, surface emissivity via the semi-empirical model, and hydrometeor information, radiative transfer modeling is used to compute Tbs for each pixel at all TMI frequencies and polarizations.

Extinction due to the clear air and cloud water is calculated assuming absorption and assuming no scattering at the TMI frequencies. For rain, snow, and graupel, mie-calculations are performed for calculation of the optical parameters. Some major assumptions are necessary here. Drop size distribution is calculated as in Iguchi et al. 2000 in order to maintain consistency with the PR algorithm. Ice particles are modeled as spherical particles of assumed density. Density is assigned as 400 kg/m^3 for graupel, and 100 kg/m^3 for snow particles, and dielectric constants are calculated as ice matrices with air inclusions. The particle distribution intercept (N0) is prescribed for each species. This is an area for possible major improvement in this scheme, particularly when it can be applied to the GPM GMI radiometer, which includes higher frequency channels and the possibility to experiment with the use of non-spherical oriented ice particles of different densities such as used in the work of Liu 2008. Ice profiles could be further adjusted within the constraint of matching DPR reflectivities.

Following calculation of the absorption and scattering parameters, radiative transfer calculations are performed through the column using the Eddington approximation (Kummerow 1993), yielding Tbs at each PR footprint. This is convolved to yield the TMI channel values. In order to maintain radiometric consistency in the higher frequency channels, simulated Tbs at 85.5 GHz are compared to observed TMI Tb. If a large positive difference (simulated Tb is much higher than observed) is found, it is assumed that ice scattering is underestimated for this pixel. Ice is added to the original profile in small increments and re-compared with the observed Tb until a match is confirmed, or to a maximum of an increase by 50%. Following this procedure the physical database entry

now includes a full set of surface, atmosphere, and hydrometeor information all fully radiometrically consistent with both the observed TMI Tbs and PR reflectivity profile.

The PR-resolution Tbs are convolved to the location and footprint resolution of the coincident TMI observations at each frequency using Gaussian-weighted averaging. This final step allows for comparison to the observed values, which will be used for in-depth analysis of the database algorithm in the following section.

4.5: Discussion and Analysis of Physical Database

The database creation scheme is applied to TRMM data within the 5-degree SGP box for the 5-year period January 2004-December 2008. An example set of input surface parameters is shown in Figure 4.2 for a typical precipitating scene, along with the coincident PR rain rates. The plotted domain is focused on the southern portion of the SGP box, covered by a TRMM overpass on May 1, 2004, and has been gridded to $1/10^{th}$-degree resolution for display purposes. Oklahoma City is visible in the upper center, and the southern Tulsa area in the upper right, as anomalies in both LAI (negative) and surface temperature (positive). Precipitation up to 14 mm/hr is falling over the southeast corner of the box. An area of extremely high soil moisture is present in this area associated with the rainfall, and in contrast to much lower soil moisture in the western portion of the box. Observed TMI Tbs are shown in Figure 4.3 for the same domain. The lower frequency channels clearly show warm emission from the liquid water associated with the rainfall in the southeast, and lower Tbs associated with the drier west. Oklahoma city, with its higher temperature and low LAI, is visible in all but the highest frequency channel as a negative Tb anomaly. There

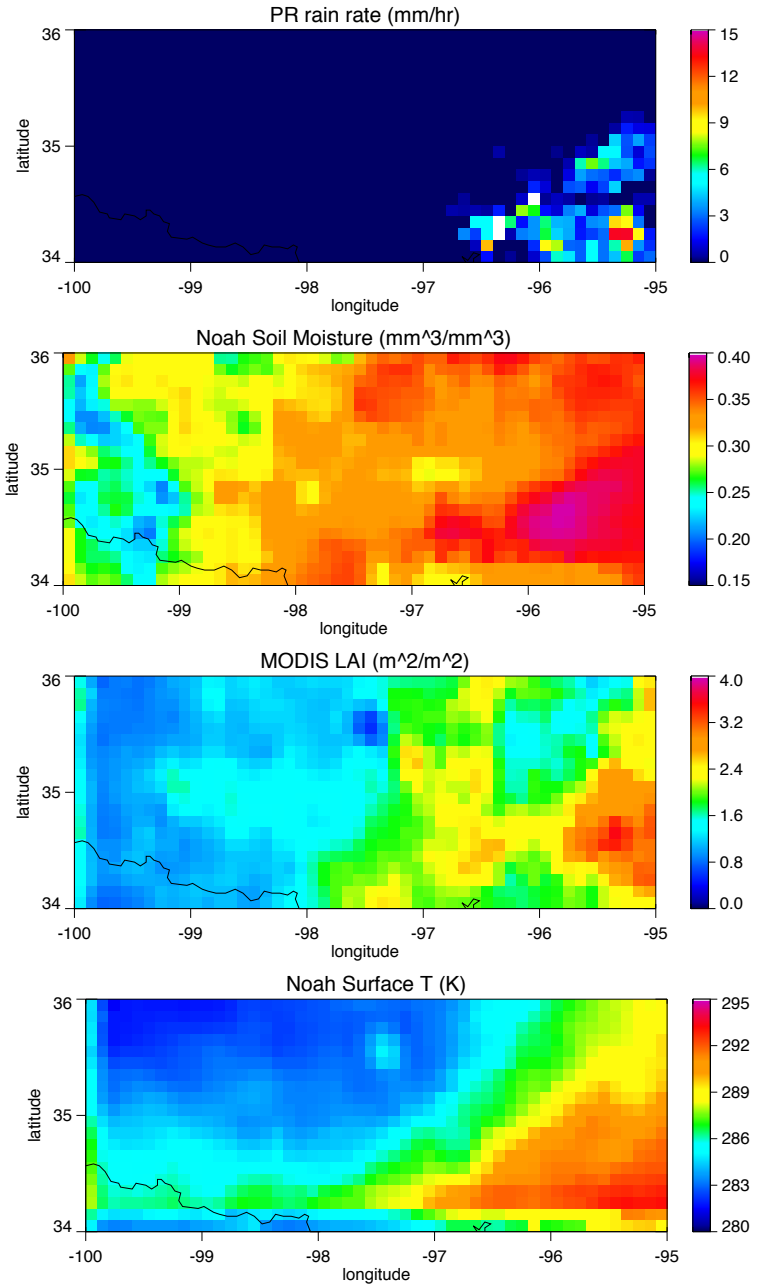

Figure 4.2: Surface parameters associated with a TRMM overpass of the SGP area on May 1, 2004. Rain rates (top) are measured from the TRMM PR. Soil moisture and surface temperature come from the Noah LSM, and LAI from the 8-day MODIS product.

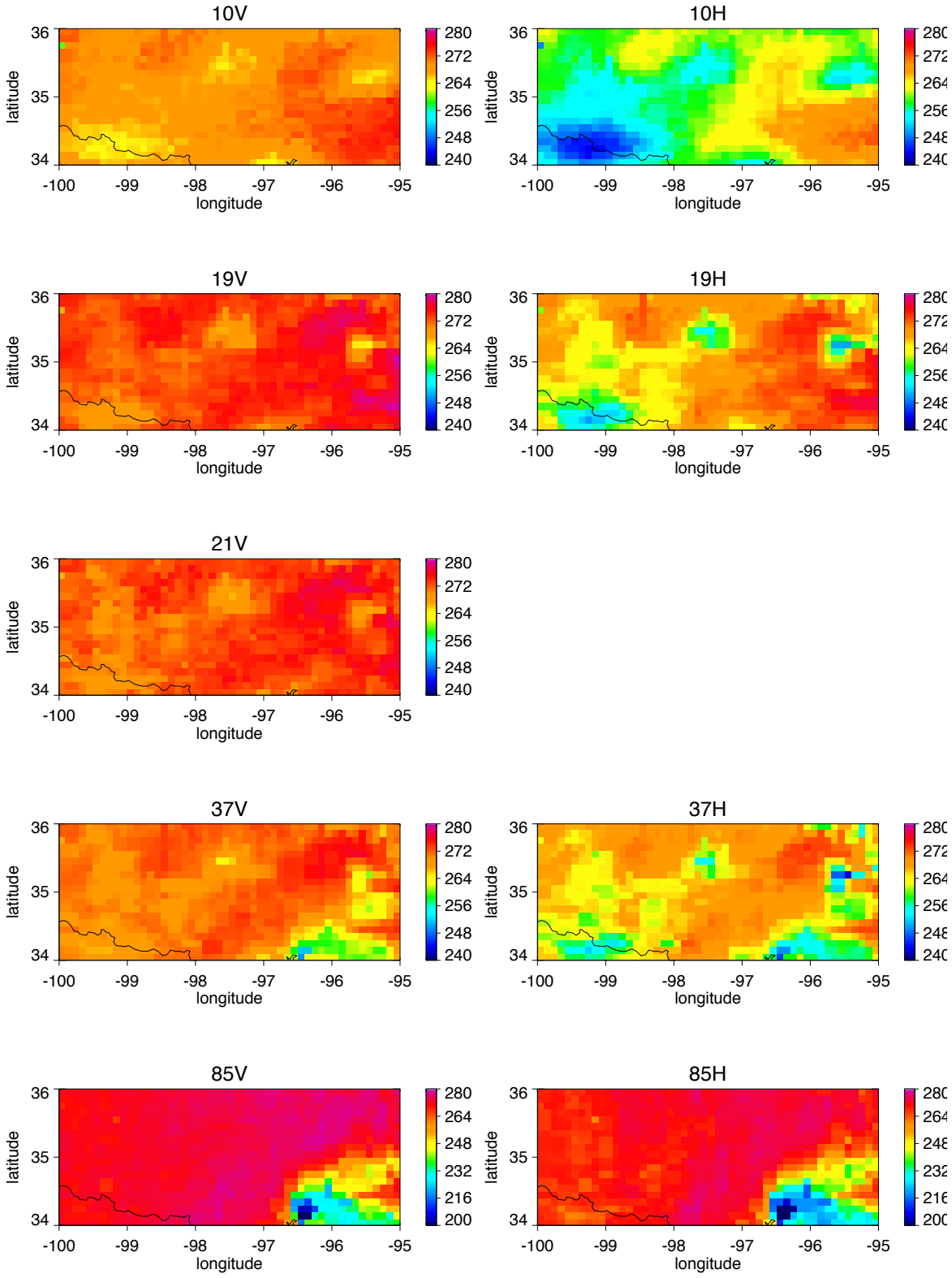

Figure 4.3: Observed TMI Tb over the southern part of the SGP domain May 1, 2004.

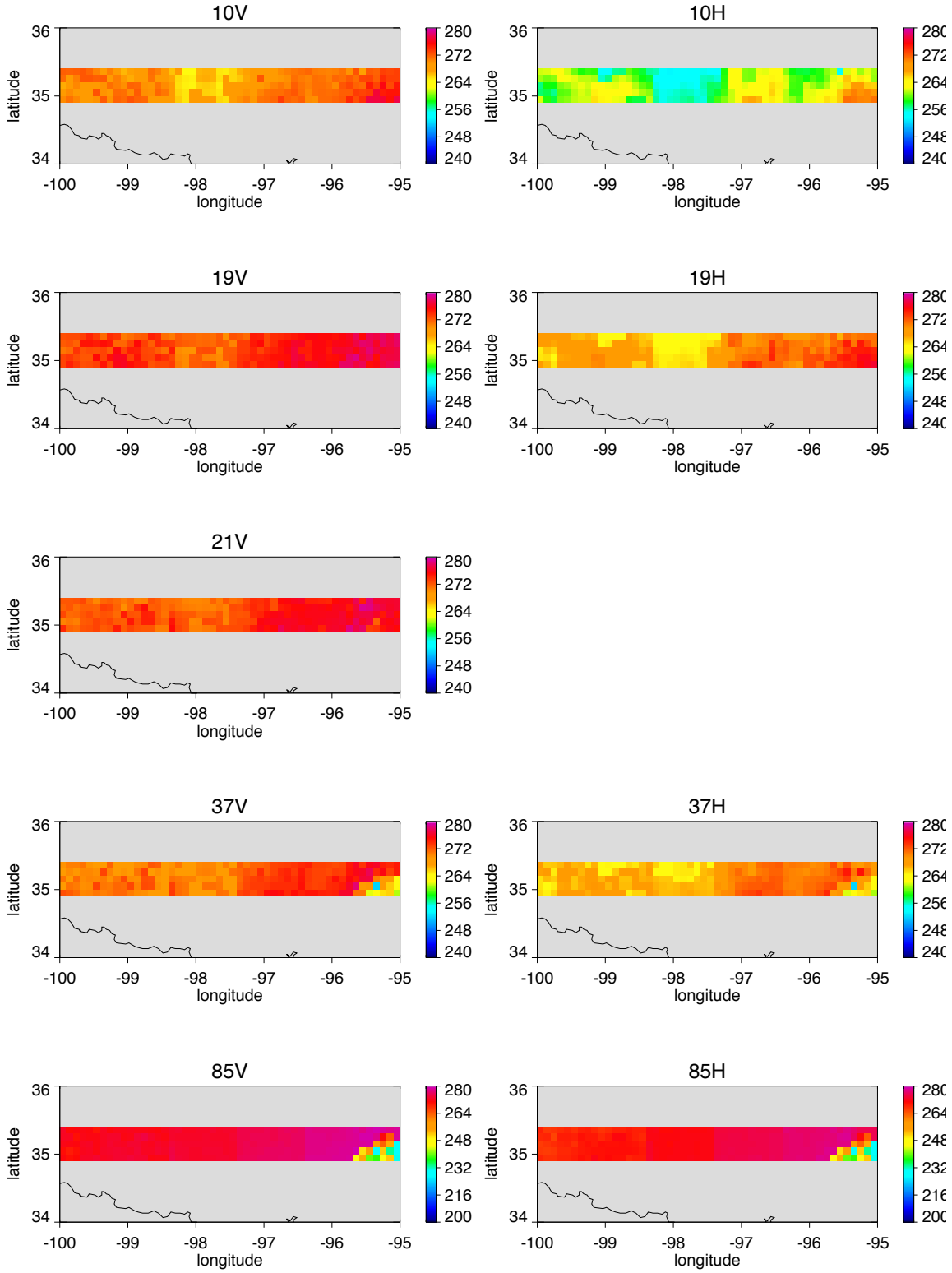

Figure 4.4: Simulated Tbs for the overpass pictured in Figure 4.3.

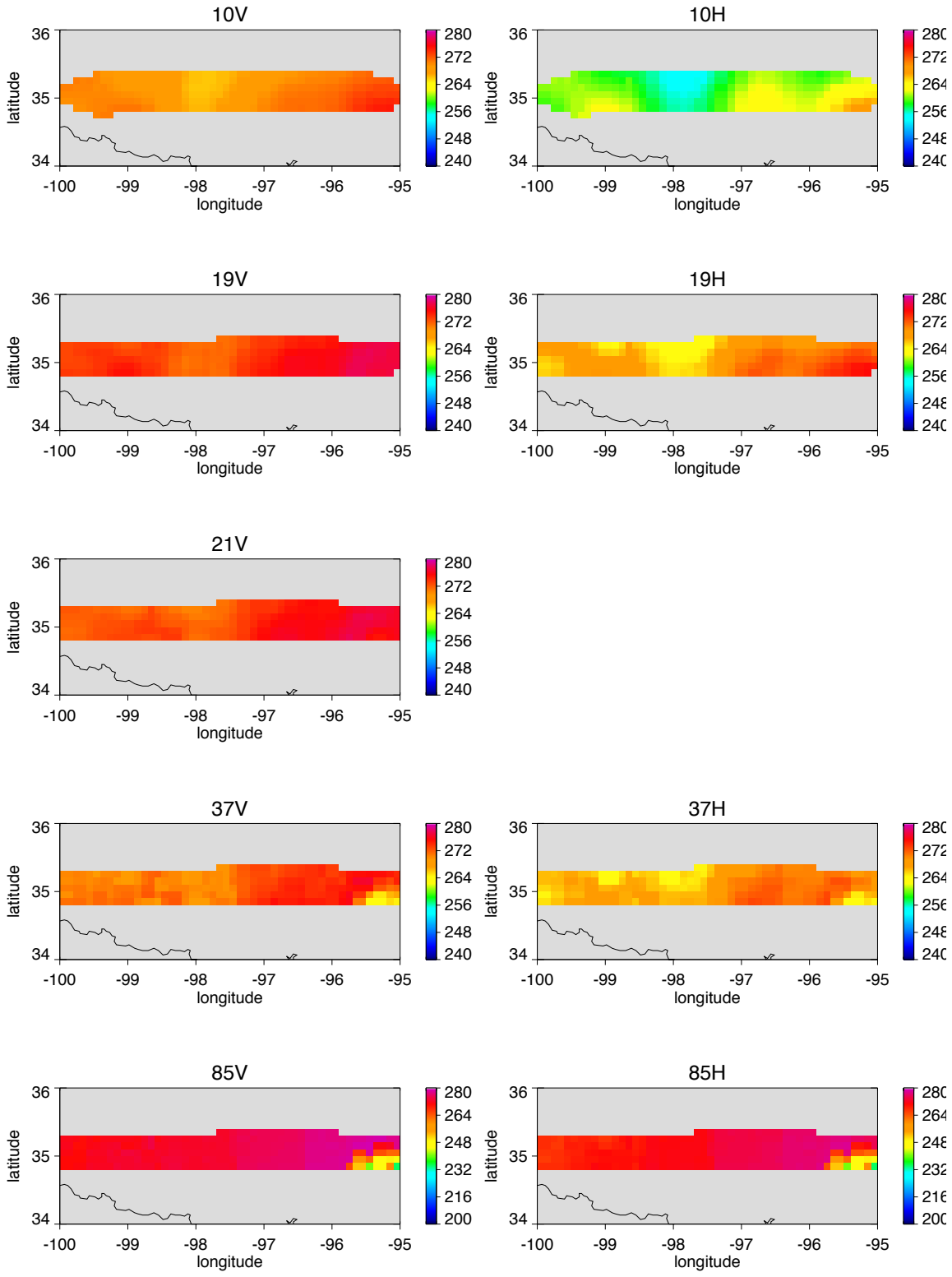

Figure 4.5: Same as Figure 4.4, convolved to TMI footprint resolution at each frequency.

is a significant ice scattering signal in the higher 37 and 85 GHz channels associated with the Tb depressions visible in the precipitating area.

Figure 4.4 shows the simulated Tbs computed using the database creation scheme for the same overpass at the resolution of the PR, the resolution at which each Tb is computed. The area of simulated Tbs is smaller than that of the original TMI observations as a result of the restriction to the narrow near-nadir swath of 11 PR pixels. The 10 and 19 GHz channels simulate the increased Tbs associated with the precipitation on the east side of the domain, but miss the significant negative anomaly in the west. At the higher frequencies, the ice scattering signal is present on the eastern edge of the domain. Figure 4.5 plots the final Tbs, convolved to the TMI footprint resolution at each frequency. The Gaussian averaging has a smoothing effect at the lower frequencies, while at 85 GHz the footprint size is similar to the PR.

For a quantitative evaluation of the Tb simulations, observed and simulated Tbs are compared over the full 5-year period. The 5-year database includes 734,842 profiles, including 40,102 raining cases. Figure 4.6 shows scatter plots of the observed-simulated Tb comparison for non-raining cases, and Figure 4.7 shows the raining cases. Table 4.2 gives the associated error statistics including correlation, mean bias, and RMS error for the simulated Tbs as compared to observed values in raining, non-raining, and total database cases. Correlations, while still near 0.9, are decreased in raining cases. Biases and RMSE are increased substantially. This indicates room for improvement in representing the raining processes. The positive bias at lower frequencies in raining cases, for example, indicates that more moisture is required in the column to match the observed Tb. For ocean retrievals, Kummerow et al. (2011) increased agreement in the database Tbs for

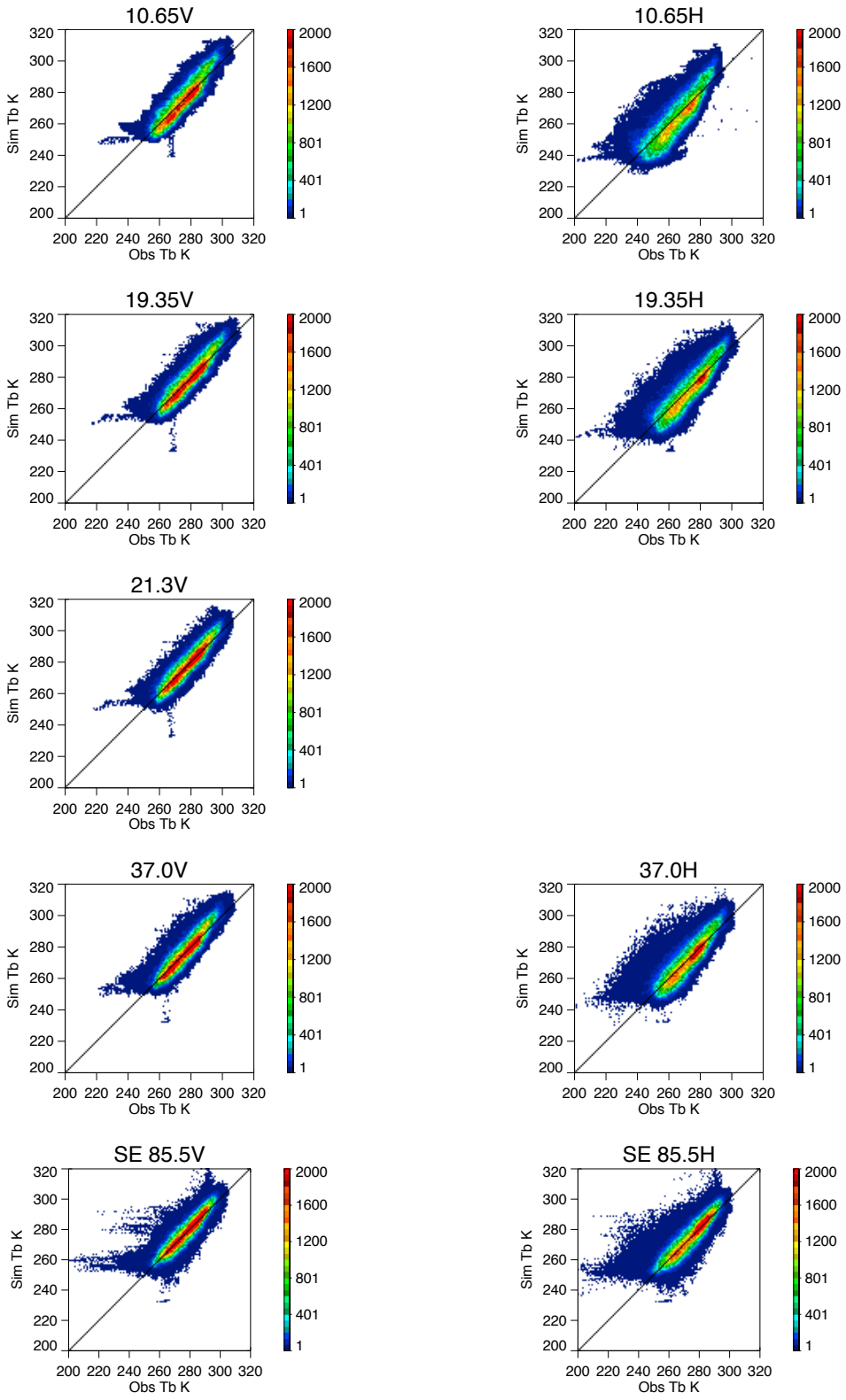

Figure 16: Observed vs. simulated TOA Tbs for all non-raining entries in the SGP database. Color indicates data density.

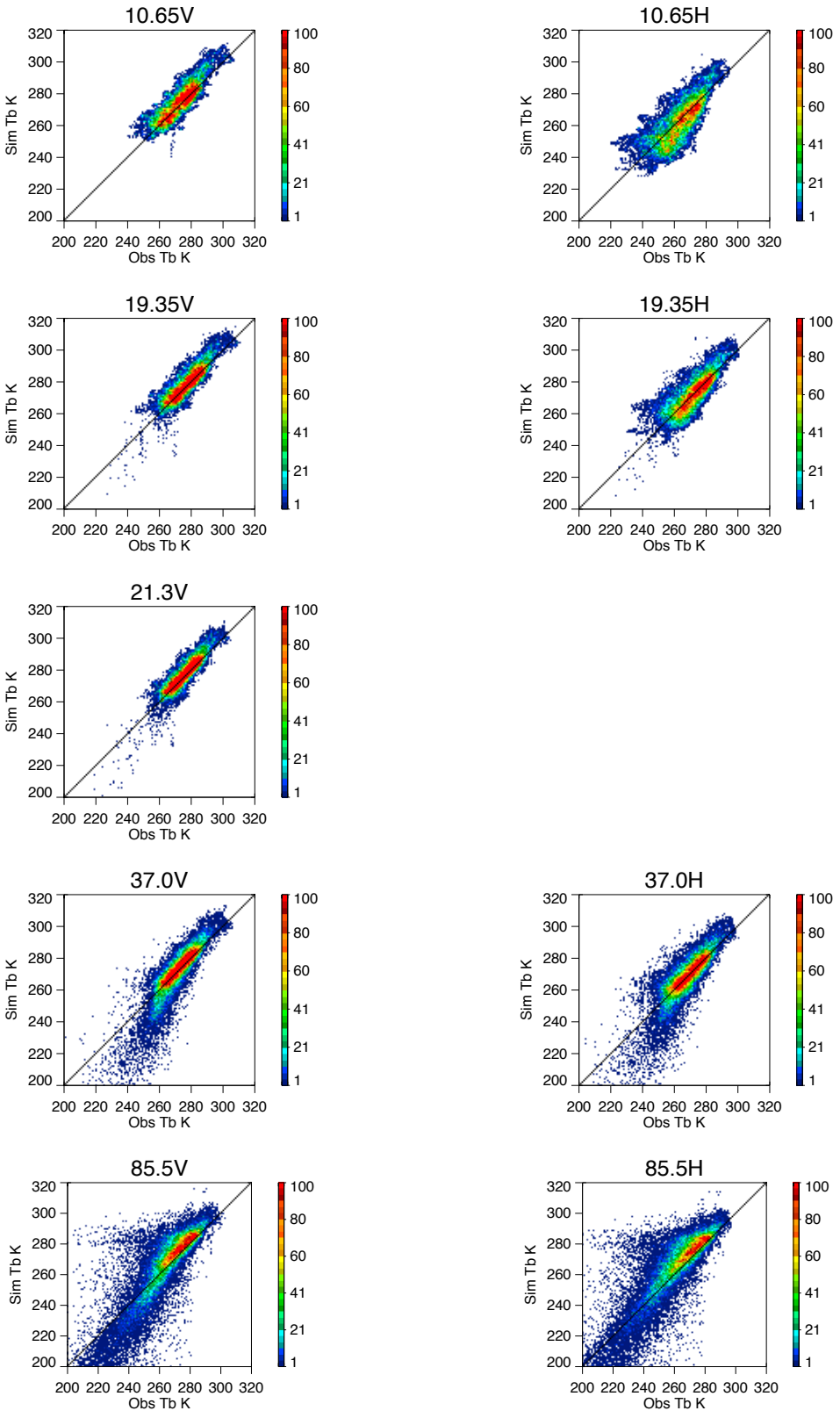

Figure 17: Same as Figure 4.6, for raining database pixels.

Table 4.2: Error statistics for simulated Tbs relative to observed values in the 2004-2008 SGP database.

Total Database	10.65V	10.65H	19.35V	19.35H	21.3V	37.0V	37.0H	85.5V	85.5H
Correlation	0.91	0.84	0.92	0.87	0.92	0.91	0.86	0.91	0.89
Mean bias (K)	0.52	-0.63	0.53	0.03	0.54	0.69	0.51	0.76	1.08
RMS	0.009	0.020	0.009	0.017	0.011	0.010	0.017	0.015	0.021

Non-Raining	10.65V	10.65H	19.35V	19.35H	21.3V	37.0V	37.0H	85.5V	85.5H
Correlation	0.91	0.85	0.92	0.87	0.93	0.92	0.86	0.91	0.89
Mean bias (K)	0.43	-0.61	0.50	0.00	0.48	0.74	0.53	0.80	0.99
RMS	0.009	0.021	0.010	0.017	0.011	0.011	0.018	0.016	0.021

Raining	10.65V	10.65H	19.35V	19.35H	21.3V	37.0V	37.0H	85.5V	85.5H
Correlation	0.87	0.78	0.88	0.81	0.90	0.89	0.85	0.89	0.88
Mean bias (K)	2.0	-0.99	1.55	0.50	1.7	0.22	0.23	0.24	2.64
RMS	0.013	0.059	0.021	0.051	0.029	0.0017	0.027	0.003	0.017

such cases by addition of drizzle below the threshold of the PR sensor, and by decreasing drop sizes (increasing LWC at constant reflectivity). Similarly negative biases can be addressed by increasing drop sizes, reducing liquid water content while maintaining consistency with PR reflectivities. Disagreements in the higher frequency channels can be addressed using similar techniques applied to ice hydrometeors. Again, this is a simplified simulation framework developed with the intention of assessing the impact of surface emissivity characterization, and development of such finely tuned adjustment schemes are beyond the scope of this work.The ice species profiles are of great interest due to the use of ice as an adjustable parameter for high frequency channels, and the historical use of ice signal as a proxy for precipitation in passive microwave algorithms. Improving agreement between the simulated and observed high frequency Tbs has benefits for the physical

precipitation retrieval scheme, but also provides information back to the cloud modeling community. Ice profiles are not a parameter that can easily be validated by the modelers, and information about the distribution of ice that best fits observations has value in that regard. Figure 4.8 shows the total column ice amounts for each raining database profile as a function of PR rain rate.

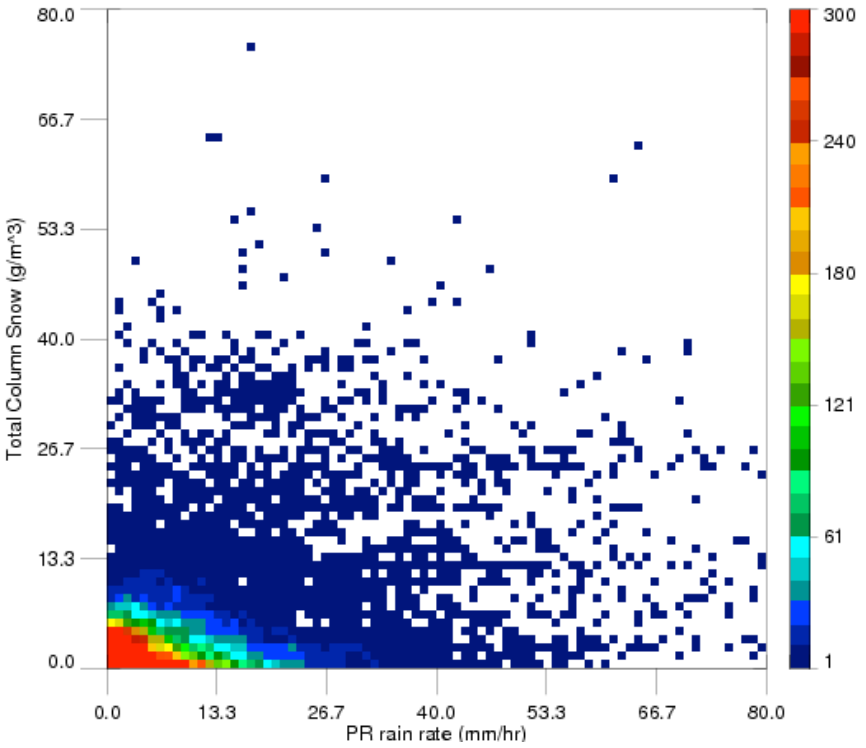

Figure 18: Total column snow as a function of rain rate for all raining database pixels. Color indicates data density at each location.

The large amount of scatter and wide distribution evident in this plot demonstrates a fundamental example of why empirical retrieval methods are destined to fail at the pixel scale, and the motivation for developing more physical retrieval schemes.

To explore the complexity of this issue further, two profiles are chosen from the raining database with identical surface rain rates, in this case 10.05 mm/hr. The first profile corresponds to a satellite overpass in summer, on August 22, 2005. The second is a

fall profile, from October 1, 2005. Surface rain rates are identical according to the PR. At 10GHz, Tbs are nearly identical, corresponding to the similar amounts of precipitating liquid water in each column. The Tbs diverge significantly as frequency increases, however, to a maximum difference of 80K at 85 GHz. The reason for this is apparent from the hydrometeor profiles associated with each case, plotted in Figure 4.9.

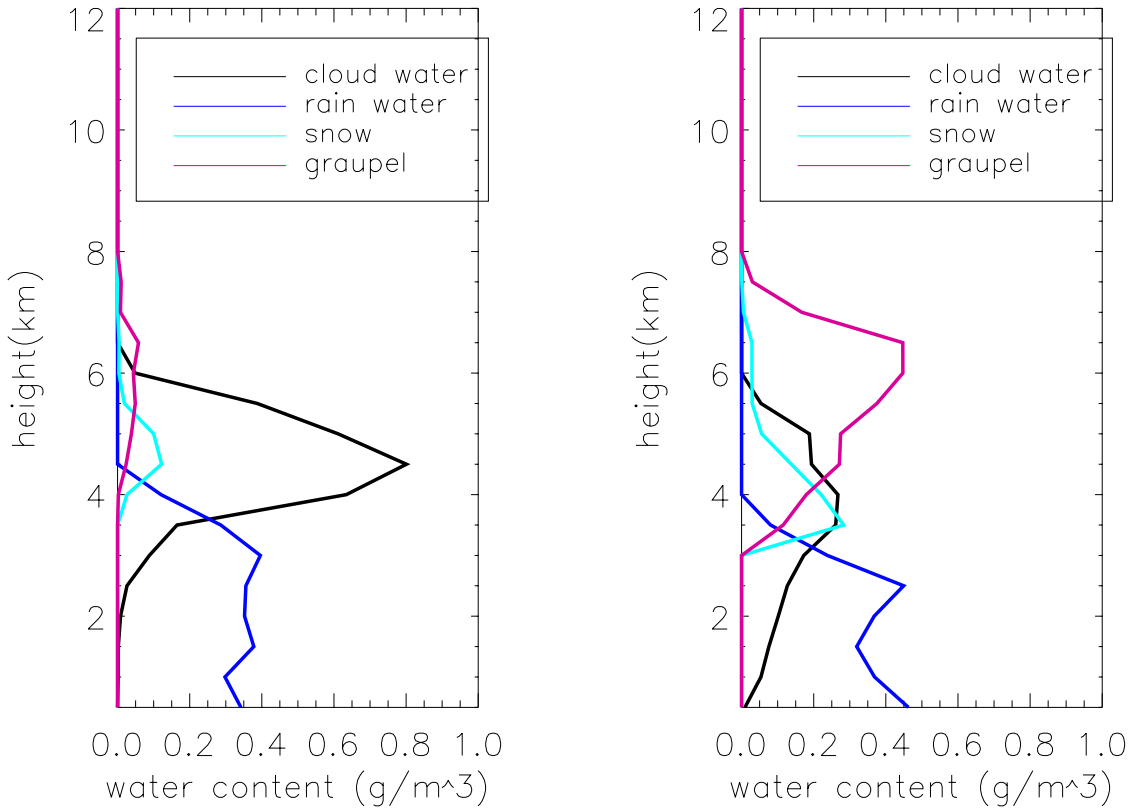

Figure 19: Hydrometeor profiles associated with two cases for which surface rain rate is identical at 10.05 mm/hr, but 85.5 GHz Tbs differ by nearly 100K.

The summer case, shown in the left panel of Figure 4.9, occurs in a warm, moist environment, with total precipitable water (TPW) value 8 mm higher than the second case, and temperature 10 K warmer. A large amount of cloud liquid water is present, and very little ice. For the fall case shown in the right panel, the same rain rate is falling in a cooler,

drier environment with large amounts snow and graupel aloft. The increased ice leads to extinction due to ice scattering in this case, yielding the much lower Tbs at higher frequency. Clearly an empirical passive microwave technique relating ice scattering to rain rate would miss the warmer rain case in the left panel, though the measured radar rain rates are identical. This demonstrates the importance of the information added by the full use of multispectral observations from the radiometer in building the physical database.

4.6: Evaluating the Impact of Dynamic Emissivity Information

The correlations between observed and simulated Tbs in section 4.5 indicate that the techniques used in construction of the prototype database are able to reasonably simulate TOA Tbs in raining and clear sky conditions. The question remains however, as to whether the dynamic surface information utilized in the semi-empirical emissivity model and calculation of the surface component of emission has improved the simulations over other, more static techniques. In order to test sensitivity to the surface characterization, the entire database creation scheme is repeated using climatological emissivity values. The climatology is computed using the five-year 2004-2008 retrieved emissivity dataset, and uses monthly mean values at 0.25-degree resolution for all points within the SGP study area.

The database simulation scheme is run using both the dynamic semi-empirical emissivity model and the monthly climatology for the two-year period Jan. 2009-December 2010, which was not included in the original construction of the emissivity model. The correlation of simulated Tb to observed TMI values at each of the 9 TMI channels is plotted

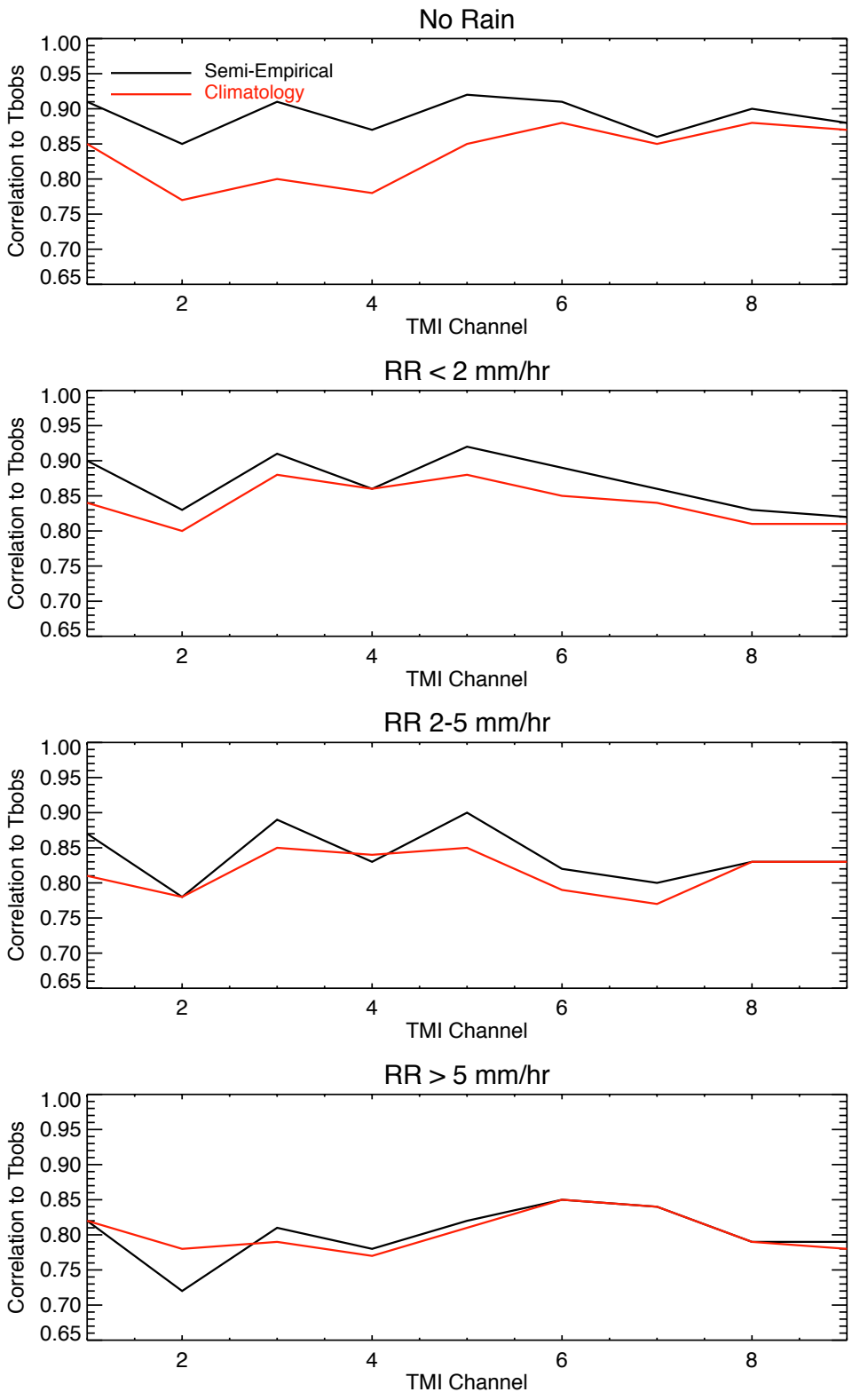

Figure 4.10: Correlation of simulated and observed Tbs at each TMI channel for the database simulations over the period 2009-2010, using dynamically modeled emissivities (black) and climatological values (red). Each row corresponds to increasing rain rate, no rain (top), 0-2 mm/hr, 2-5 mm/hr, and greater than 5 mm/hr (bottom).

for both methods in Figure 4.10. Correlations for the database using the dynamic emissivities calculated via the semi-empirical model are shown in black, with values corresponding to the run using climatological values in red. Each panel in the column shows correlations for particular rain rates as reported by the coincident PR observations and averaged to the 19 GHz footprint area for a TMI rain rate. The comparison suggests several conclusions. First of all, regardless of rain rate, the high frequency channels show small to zero difference in correlation to observed Tb, indicative of the lower sensitivity to the surface at these smaller wavelengths. At the lower frequencies, the dynamic emissivity values show significantly improved correlation to observations for non-raining pixels. This improvement decreases as rain rate increases. At 5 mm/hr over the TMI footprint, correlations are nearly identical for the two databases, suggesting that at this rain rate level, representation of the surface becomes secondary to accurate simulation of the hydrometeors and atmospheric conditions. A comparison of biases indicates the same behavior, with smaller general biases using the dynamic emissivities, and differences between the biases from the climatology database that decrease as a function of both rain rate and frequency. This also suggests that, in raining areas where the higher frequency 85 GHz channels are known to have little to no sensitivity to the surface, the decreased surface sensitivity in the lower frequencies provides added benefit, in that these Tbs can now be interpreted as a function of other information content, such as rain profile information and the discrimination of cold surfaces from precipitation scattering signals.

4.7: Database Construction Conclusions

In developing a physical database for Bayesian-type precipitation retrieval schemes over land, accurate representation of the surface emission is an important and difficult problem. In the work presented here, a simple physical database is constructed in order to assess sensitivity of such a database to surface emissivity characterization. The semi-empirical emissivity model developed in Chapter 3 is implemented for this purpose, and is used to compute emission from the surface in a forward model for database radiative transfer simulations. The atmosphere is modeled using background environment information from the ERA-Interim reanalysis along with hydrometeor profiles derived from constrained matching of CRM profiles with profiles from the active measurements of the TRMM PR. Ice profiles are adjusted in an iterative scheme aimed at increasing agreement in the higher frequency channels. For non-raining pixels, resulting agreement between simulated and measured TMI Tbs is good, with correlations around 0.9 and multispectral biases less than 1K. In raining areas the agreement is somewhat degraded, but still shows correlation with measured Tbs of 0.8-0.9.

The resulting SGP database is utilized to explore the importance of accurate representation of ice profiles in such a scheme. Precipitating database entries suggest a complex, non-unique relationship between profile ice and rain rate. Investigation at the profile level demonstrates that rain rates can match exactly and correspond to very different Tbs due to extinction by ice in the column as well as environmental parameters that affect the different frequencies on very different levels. Future expansion of the database will require continued work in the area of accurate representation of column ice, which may include changing amounts (concentration and mass), densities, species, and

orientation. The recent launch of the GPM satellite offers the possibility of creating a similar active-passive database with the addition of higher frequency channels, adding more information for such advancement.

Comparison of the database to an identical one constructed using climatological emissivity values provides information regarding the importance of dynamic representation of emissivity in such a scheme. Correlations to observed Tb values are increased when simulated using the dynamic surface, particularly at the lowest TMI frequencies. This improvement is largest for pixels with no rain and therefore more soil moisture influence, and decreases with rain rate. At a rain rate of 5 mm/hr averaged over the 19 GHz TMI footprint area, the difference in correlation becomes insignificant. This comparison suggests that dynamic representation of surface emissivity in simulations for precipitation database construction will have the most significant impact in areas of light or no rain, with emissivity accuracy becoming less important in areas of heavier rain and at higher frequencies that have less sensitivity to the surface.

It appears clear that with optimization, it is possible to develop a database with precipitation signals that can be accurately distinguished from surface emission over land, and that such a database could be implemented in to a Bayesian retrieval framework. While the present work demonstrates the feasibility of physical retrieval, clear biases are present along with other problem areas, which could be targeted in future work.

Chapter 5: Conclusions

With the recent launch of the GPM satellite, the potential exists to greatly increase current knowledge of global precipitation. A dual frequency radar, increased radiometer resolution, higher frequency channels, and increased global orbital extent will allow for the creation of high quality physical databases for implementation in Bayesian-type precipitation schemes and application to other radiometers. Such an increase in available information content will particularly allow for better passive microwave measurement of precipitation over land, where historically retrievals have relied on empirical ice scattering relationships (e.g. Gopalan et al. 2010).

The greatest area of difficulty in improving physical retrieval schemes over land involves the accurate representation of surface emission. Over ocean surfaces, emissivity in the microwave window channels is on the order of 0.5, a radiometrically cold background from which to distinguish the warm emission signal of liquid water in the atmosphere. The ocean surface emissivity is a function of relatively few parameters, including temperature, wind speed (roughness), and salinity. Over land however, the emissivity is often greater than 0.9. It is a complex function of dielectric properties corresponding to all components of the soil, vegetation, and anything else on the surface. The emissivity is challenging to model, and can be easily retrieved only in clear-sky conditions.

The initial goal of this work is therefore the development and implementation of a method for dynamic representation of the microwave land surface emissivity that has sufficient accuracy to be used as the surface component in the full column modeling

necessary in creating a physical database. As a feasibility experiment, this work is centered in a 5-degree latitude-longitude box in the US Southern Great Plains area, due to its large number of available input data sets and observations for validation.

Work is first undertaken to assess the accuracy of various emissivity calculation techniques, as outlined in Chapter 2. Comparison of the physical emissivity model operationally used by NCEP within CRTM, with retrieved emissivities suggests that, particularly in the higher microwave frequencies, modeled values fail to reproduce dynamic variability present in the observations. The issue of accurate input data is explored, and it is clear that global emissivity modeling results will depend upon the temporal and spatial quality of input data at each location, an important caveat.

Following the conclusions of the model-retrieval comparison, a semi-empirical model is constructed with the goal of implementing the highest information content available from the models and observations in the resulting scheme. A physical emissivity model is used at a single polarization and frequency, chosen as a result of closest agreement in the comparison study. These modeled emissivities are then mapped to all other frequencies using empirically derived covariance relationships from robust data sets of retrieved emissivities. The covariance relationships are computed and applied as a function of soil moisture and leaf area index, optimizing correlation values for the relationships. The resulting emissivities are used to compute TOA Tbs for cloud-free areas over a two-year period, and found to agree well with observed Tbs, with correlations around 0.9 and biases generally less than 1K.

The semi-empirical technique is then implemented in development of a physical database for the SGP area, utilizing the TRMM satellite and similar techniques to those

employed by Kummerow et al. 2011 over the tropical oceans. Background environment information from the ERA-interim reanalysis is used along with hydrometeor profiles derived from constrained matching of TRMM PR reflectivity profiles and CRM data. Ice profiles are adjusted in an iterative scheme for the best match in the highest frequency channels. The result is a simple, radiometrically consistent physical database of the type applied in radiometer algorithms for Bayesian precipitation retrieval. Simulated Tbs compare to observations with high correlations and low bias. In order to assess the value added by implementation of a dynamic model for surface emissivity, the database construction scheme is compared to results using climatological emissivity values. The results indicate improved correlation with observed Tb values for the database that includes dynamic emissivity, with an improvement that is most significant at low frequencies and zero or small rain rates. The higher frequencies, less sensitive to the surface, show much less sensitivity to emissivity used. As rain rate increases, the sensitivity to surface emissivity becomes much smaller, with correlations nearly identical for the two methods above a rain rate of 5 mm/hr over a 19 GHz TMI footprint area.

The present work, constructing a simple physical database, suggests that physical passive microwave retrievals can be accurately implemented over land where the emissivity can be accurately represented and distinguished from emission and scattering by hydrometeors. Work remains in developing this system for global operational use. While the SGP area encompasses a reasonable range of vegetation, soils, and seasonal temperature change, extension to other surface types will be challenging. Over desert surfaces in particular, emissivity is difficult to calculate as dry, sandy soils allow for a highly variable and larger

penetration depth, which must be properly modeled. Snow-covered surfaces, coastal areas, inland water, and uneven terrain and orography similarly present challenges.

The success of the semi-empirical model here does, however, illustrate that as the emissivity characteristics of such surface types become better understood, the techniques demonstrated in this work can be easily implemented using the same physical basis that has been successfully used in retrieving precipitation over the ocean. Combining dynamic surface representation with future improvements in hydrometeor representation resulting from the increased information available via the GPM GMI/DPR collocated observations, has the potential to lead to a smooth, consistent, physical retrieval for the globe.

References

Ackerman, S.A., R.E. Holz, R. Frey, E.W. Eloranta, B.C. Maddux, and M. McGill, 2008: Cloud detection with MODIS: Part II: Validation, *J. Atmos. Oceanic Technol*., **25**, 1073–1086.

Adler, R.F., G. J. Huffman, and P. R. Keehn, 1994: Global tropical rain rate estimates from microwave-adjusted geosynchronous IR data. *Remote Sens. Rev.,* **11**, 125–152.

Aires, F., C. Prigent, W.B. Rossow, M. Rothstein , 2001: A new neural network approach including first guess for retrieval of atmospheric water vapor, cloud liquid water path, surface temperature, and emissivities over land from satellite microwave observations, *J. Geophys. Res.,* **106**(D14), 14887-14907.

Aires, F., C. Prigent, F. Bernardo, C. Jiménez, R. Saunders, and P. Brunel, 2011: A Tool to Estimate Land-Surface Emissivities at Microwave frequencies (TELSEM) for use in numerical weather prediction, *Q.J.R. Meteorol. Soc*., **137**, 690–699.

Arkin, Phillip A., Bernard N. Meisner, 1987: The Relationship between Large-Scale Convective Rainfall and Cold Cloud over the Western Hemisphere during 1982-84. *Mon. Wea. Rev*., **115**, 51–74.

Barrett, Eric C., 1970: The Estimation of Monthly Rainfall From Satellite Data. *Mon. Wea. Rev*., **98**, 322–327.

Bauer, P., E. Moreau, and S. Di Michele, 2005, Hydrometeor Retrieval Accuracy Using Microwave Window and Sounding Channel Observations, *J. Appl. Meteor*, **44**, 1016– 1032.

Boukabara, S-A., K. Garrett, Wanchun Chen, F. Iturbide-Sanchez, C. Grassotti, C. Kongoli, Ruiyue Chen, Quanhua Liu, Banghua Yan, Fuzhong Weng, R. Ferraro, T. J. Kleespies, and Huan Meng, 2011: MiRS: An All-Weather 1DVAR Satellite Data Assimilation and Retrieval System, *IEEE Transactions on Geoscience and Remote Sensing*, **49**, 3249-3242.

Bytheway, J. L., and C. D. Kummerow, 2010: A Physically Based Screen for Precipitation Over Complex Surfaces Using Passive Microwave Observations. *IEEE Transactions on Geoscience and Remote Sensing*, **48**, 299-313.

Calvet, J., J. Wigneron, J. Walker, F. Karbou, A. Chanzy, and C. Albergel, 2011: Sensitivity of Passive Microwave Observations to Soil Moisture and Vegetation Water Content: L-Band to W-Band, *IEEE Transactions on Geoscience and Remote Sensing*, **49**, 1190-1199.

Conner, Mark D., Grant W. Petty, 1998: Validation and Intercomparison of SSM/I Rain-Rate

Retrieval Methods over the Continental United States. *J. Appl. Meteor*., **37**, 679–700.

Cosh, M/H., T.J. Jackson, P. Starks, G. Heathman, 2006: Temporal Stability of Surface Soil Moisture in the Little Washita River Watershed and its Applications in Satellite Soil Moisture Product Validation, *J. Hydrology*, **323**, 168-177.

Dee, D.P., S.M. Uppala, A.J. Simmons, P. Berrisford, P. Poli, S. Kobayashi, U. Andrae, M.A. Balmaseda, G. Balsamo, P. Bauer, P. Bechtold, A.C.M. Beljaars, L. van de Berg, J. Bidlot, N. Bormann, C. Delsol, R. Dragani, M. Fuentes, A.J. Geer, L. Haimberger, S.B. Healy, H. Hersbach, E.V. Holm, L. Isaksen, P. Kallberg, M. Kohler, M. Matricardi, A.P. McNally, B.M. Monge-Sanz, J.-J. Morcrette, B.-K. Park, C. Peubey, P. de Rosnay, C. Tavolato, J.-N. Thepaut, and F. Vitart, 2011: The ERA-Interim reanalysis: configuration and performance of the data assimilation system, *Q. J. R. Meteorol. Soc.* **137**, 553-597.

Dobson, M. C., F.T. Ulaby, M. T. Hallikainen, and M. A. El-Rayes, 1985: Microwave Dielectric Behavior of Wet Soil – Part II: Dielectric Mixing Models, *IEEE Trans. Geosci. Remote Sens.*, **GE-23**, 35-46.

Ek, M. B., K. E. Mitchell, Y. Lin, E. Rogers, P. Grunmann, V. Koren, G. Gayno, and J. D. Tarpley, 2003: Implementation of Noah land surface model advances in the National Centers for Environmental Prediction operational mesoscale Eta model, *J. Geophys. Res.,* **108**(D22), 8851.

Elliott, R.L., F.R. Schiebe, K.C. Crawford, K.D. Peter and W.E. Puckett, 1993: A unique data capability for natural resources studies", Paper No. 932529, International Winter Meeting; American Society of Agricultural Engineers, Chicago, IL, Dec. 14-17.

Evans, K. F., J. Turk, T. Wong, and G. Stephens, 1995: A Bayesian approach to microwave precipitation profile retrieval. *J. Appl. Meteor.*, **34**, 260–279.

Ferraro, R., C.D. Peters-Lidard, C. Hernandez, F.J. Turk, F. Aires, C. Prigent, X. Lin, S. Boukabara, F.A. Furuzawa, K. Gopalan, K.W. Harrison, F. Karbou, L. Li, C. Liu, H. Masunaga, L. Moy, S. Ringerud, G.M. Skofronick-Jackson, Y. Tian, and N. Wang, 2013: An Evaluation of Microwave Land Surface Emissivities over the Continental United States to Benefit GPM-era Precipitation Algorithms", *IEEE Transactions on Geoscience and Remote Sensing*, **51**, 378-398.

Frey, R. S. A. Ackerman, Y. Liu, K. I. Strabala, H. Zhang, J. Key, and X. Wang, 2008: Cloud detection with MODIS: Part I. Improvements in the MODIS Cloud Mask for Collection 5, *J. Atmos. Oceanic Technol*., **25**, 1057– 1072.

Fritz, Sigmund, Jay S. Winston, 1962: Synoptic Use of Radiation Measurements From Satellite TIROS II. *Mon. Wea. Rev*., **90**, 1–9.

Gao, H., E.F. Wood, M. Drusch, W. Crow, and T.J. Jackson, 2004: Using a microwave emission model to estimate soil moisture from ESTAR observations during SGP99, *J. Hydromet*., **5**, 49– 63.

Gopalan, K., N. Y. Wang, R. Ferraro, and C. Liu, 2010: Status of the TRMM 2A12 land precipitation algorithm. *J. Atmos. Oceanic Technol.*, **27**, 1343–1354.

Grody, N.C., 1988: Surface Identification Using Satellite Microwave Radiometers, *IEEE Transactions on Geoscience and Remote Sensing*, vol. **26**, pp. 850-859.

Grody, N.C, 2008: Relationship between snow parameters and microwave satellite measurements: Theory compared with Advanced Microwave Sounding Unit observations from 23 to 150 GHz, *J. Geophys. Res.,* **113**, D22108.

Heymsfeld, G.M. and R. Fulton, 1992: Modulation of SSM/I Microwave Soil Radiances by Rainfall, *Remote Sensing of Environment*, **39**, pp. 187-202.

Holmes, T.R.H., M. Drusch, J.-P. Wigneron, and R. A. M. de Jeu, 2008: A Global Simulation of Microwave Emission: Error Structures Based on Output From ECMWF's Operational Integrated Forecast System, *IEEE Transactions on Geoscience and Remote Sensing*, **46**, 846-856.

Holz , R.E., S. A. Ackerman , F. W. Nagle , R. Frey , S. Dutcher , R. E. Kuehn , M. A. Vaughan and B. Baum, 2008: Global MODIS cloud detection and height evaluation using CALIOP, *J. Geophys. Res.*, **113**.

Hong, S., 2010: Detection of small-scale roughness and refractive index of sea ice in passive microwave remote sensing. *Remote Sensing of Environment*, **114,** 1136-1140.

Hou, A.Y., R.K. Kakar, S. Neeck, A.A. Azarbarzin, C.D. Kummerow, M. Kojima, R. Oki, K. Nakamura, T. Iguchi, 2014: The Global Precipitation Measurement (GPM) Mission, *Bull. Amer. Meteor. Soc.,* **95**, 701-722.

Iguchi, T., T. Kozu, R. Meneghini, J. Awaka, and K. Okamoto, 2000: Rain-profiling algorithm for the TRMM precipitation radar. *J. Appl. Meteor*, **39**, 2038–2052.

Jackson, T.J., and L. Moy, 1999: Dew Effects on Passive Microwave Observations of Land Surfaces," *Remote Sensing of Environment*, **70**, 129-137.

Jackson, T.J., D.M. Le Vine, A.Y. Hsu, A. Oldak, P.J. Starks, C.T. Swift, J.D. Isham, and M. Haken, 1999: Soil Moisture Mapping at Regional Scales Using Microwave Radiometry: The Southern Great Plains Hydrology Experiment, *IEEE Trans. Geosci. Remote Sens*., **37**, 2136–2151.

Jackson, T.J., A.Y. Hsu, and P.E. O'Neill, 2002: Surface Soil Moisture Retrieval and

Mapping Using High-Frequency Microwave Satellite Observations in the Southern Great Plains, *J. Hydromet.*, **3**, 688– 699.

Jackson, T.J., M.H. Cosh, R. Bindlish, P.J. Starks, D.D. Bosch, M. Seyfried, D.C. Goodrich, M.S. Moran, and J. Du, 2010: Validation of Advanced Microwave Scanning Radiometer Soil Moisture Products, *IEEE Trans. Geosci. Remote Sensing*, **48**, 4256-4272.

Jones, M. O., L.A. Jones, J.S. Kimball, and K.C. McDonald, 2011: Satellite passive microwave remote sensing for monitoring global land surface phenology, *Remote Sensing of Environment*, **115**, 1102-1114.

Justice, C.O., J.R.G. Townshend, E.F. Vermote, E. Masuoka, R.E. Wolfe, N. Saleous, D.P. Roy, and J.T. Morisette, 2002: An overview of MODIS land data processing and product status, *Remote Sensing of Environment*, **83**, 3-15.

Kelly, R.E., A.T. Chang, L. Tsang, and J.L. Foster, 2003: A Prototype AMSR-E Global Snow Area and Snow Depth Algorithm, *IEEE Trans. Geosci. Remote Sensing*, **41**, 230-242.

Kumar, S., C.D. Peters-Lidard, Y. Tian, P.R. Houser, J. Geiger, S. Olden, L. Lighty, J.L. Eastman, B. Doty, P. Dirmeyer, J. Adams, K. Mitchell, E. F. Wood and J. Sheffield, 2006: Land information system: an interoperable framework for high resolution land surface modeling," *Environ Model Software,* **21**, 1402–1415.

Kummerow, C., 1993: On the accuracy of the Eddington approximation for radiative transfer in the microwave frequencies. *J. Geophys. Res.*, **98**, 2757-2765.

Kummerow, C., W. Barnes, T. Kozu, J. Shiue, and J. Simpson, 1998: The Tropical Rainfall Measuring Mission (TRMM) sensor package. *J. Atmos. Oceanic Technol.,* **15**, 808-816.

Kummerow, Christian, D.B. Shin, Y., Hong, W.S. Olson, S. Yang, R.F. Adler, J. McCollum, R. Ferraro, G. Petty and T.T. Wilheit, 2001: The Evolution of the Goddard Profiling Algorithm (GPROF) for Rainfall Estimation from Passive Microwave Sensors. *J. Appl. Meteor.*, **40**, 1801–1820.

Kummerow, C., S. Ringerud, J. Crook, D. Randel, and W. Berg, 2011: An observationally based a priori database for microwave rainfall retrievals. *J. Atmos. Oceanic Technol.*, **28**, 113–130.

Lang, S., W-K. Tao, J. Simpson, and B. Ferrier, 2003: Modeling of Convective-Stratiform Precipitation Processes: Sensitivity to Partitioning Methods. *J. Appl. Meteor.*, **42**, 505–527.

Li, X., W-K. Tao, T. Matsui, C. Liu, and H. Masunaga, 2010: Improving a spectral bin Microphysical scheme using TRMM satellite observations. *Q. J. R. Meteorol. Soc.* **136**, 382-399.

Lin, B., and P. Minnis, 2000: Temporal variations of land surface microwave emissivities over the atmospheric radiation measurement program southern Great Plains site. *J. Appl. Meteor*. **39**, 1103–1116.

Liu, G., 2008: A database of microwave single-scattering properties for nonspherical ice particles. *Bull. Amer. Meteor. Soc*., **89**, 1563–1570.

Masunaga H., and C.D. Kummerow, 2005: Combined Radar and Radiometer Analysis of Precipitation Profiles for a Parametric Retrieval Algorithm. *J. Atmos. Oceanic Technol.,* **22**, 909-929.

Matzler, C., 2005: On the determination of surface emissivity from Satellite observations, *Geoscience and Remote Sensing Letters, IEEE* , **2**, no.2, 160- 163.

McCabe, M.F., E.F. Wood, and H. Gao, 2005: Initial soil moisture retrievals from AMSR-E: Multiscale comparison using in situ data and rainfall patterns over Iowa," *Geophys. Res. Letters,* **32**, L06403.

Moncet, J., P. Liang, J.F. Galantowicz, A.E. Lipton, G. Uymin, C. Prigent, and C. Grassotti, 2011: Land surface microwave emissivities derived from AMSR-E and MODIS measurements with advanced quality control, *J. Geophys. Res.,* **116**, D16104.

Njoku, E.G., and L. Li, 1999: Retrieval of Land Surface Parameters Using Passive Microwave Measurements at 6-18 GHz, *IEEE Trans. Geosci. Remote Sensing*, **37**, pp. 79-93.

Njoku, E.G.; Jackson, T.J.; Lakshmi, V.; Chan, T.K.; Nghiem, S.V., 2003: Soil moisture retrieval from AMSR-E, *IEEE Trans. Geosci. Remote Sensing*, **41**, 215-229.

Norouzi, H., W. Rossow, M. Temimi, C. Prigent, M. Azarderakhsh, S. Boukabara, and R. Khanbilvardi, 2012: Using microwave brightness temperature diurnal cycle to improve emissivity retrievals over land. *Remote Sensing of Environment*, **123**, 470-482.

Owe, M., and A. A. Van de Griend, 1998: Comparison of soil moisture penetration depths for several bare soils at two microwave frequencies and implications for remote sensing, *Water Resources Research*, **34**, 2319-2327.

Owe, M., R. de Jeu, and T. Holmes, 2008: Multisensor Historical Climatology of Satellite-Derived Global Land Surface Moisture. *J. Geophys. Res.,* **113**, F01002,

doi:10.1029/2007JF000769.

Petty, Grant W., 1999: Prevalence of Precipitation from Warm-Topped Clouds over Eastern Asia and the Western Pacific. *J. Climate*, **12**, 220–229.

Prigent, Catherine, Filipe Aires, William B. Rossow, 2006: Land Surface Microwave Emissivities over the Globe for a Decade. *Bull. Amer. Meteor. Soc.,* **87**, 1573– 1584.

Reichle, R.H., and R.D. Koster, 2004: Bias Reduction in Short Records of Satellite Soil Moisture", *J. Geophys. Res.,* **31**, L19501.

Ringerud, S., C. Kummerow, C. Peters-Lidard, Y.Tian, and K. Harrison, 2014a: A Comparison of Microwave Window Channel Retrieved and Forward-Modeled Emissivities Over the U.S. Southern Great Plains, *IEEE Trans. Geosci. Remote Sensing*, **52**, 2395-2412.

Ringerud, S., C. D. Kummerow, C. Peters-Lidard, 2014b: A Semi-Empirical Model for Computing Land Surface Emissivities in the Microwave Region. *IEEE Transactions on Geoscience and Remote Sensing*, doi:10.1109/TGRS.2014.2351232

Rossow, W.B., and R.A. Schiffer, 1999: Advances in Understanding Clouds from ISCCP," *Bull. Amer. Meteor. Soc.*, vol. **80** pp. 2261-2287.

Ruston, B.C., and T.H. Vonder Haar, 2004: Characterization of summertime microwave emissivities from the Special Sensor Microwave Imager over the conterminous United States. *J. Geophys. Res.,* **109**,D19103.

Skofronick-Jackson, G.M., M. Kim, J.A. Weinman, and D. Chang, 2004: A Physical Model to Determine Snowfall Over Land by Microwave Radiometry, *IEEE Transactions on Geoscience and Remote Sensing*, **42**, 1047-1058.

Stephens, Graeme L., Christian D. Kummerow, 2007: The Remote Sensing of Clouds and Precipitation from Space: A Review. *J. Atmos. Sci*., **64**, 3742–3765.

Tian, Yudong, Christa D. Peters-Lidard, Bhaskar J. Choudhury, Matthew Garcia, 2007: Multitemporal Analysis of TRMM-Based Satellite Precipitation Products for Land Data Assimilation Applications. *J. Hydrometeor*, **8**, 1165–1183.

Turner, D.D., R. Ferrare, L.A. Brasseur, 2001: Average Aerosol Extinction and Water Vapor Profiles Over the Southern Great Plains. *Geophysical Research Letters,* **28**, 4441-4444.

Wegmuller, U. C. Matzler, and E.G. Njoku, 1995: Canopy Opacity Models, in Passive Microwave Remote Sensing of Land-Atmosphere Interactions, Eds. B.J. Choudhury, Y.H. Kerr, E.G. Njoku, and P. Pampaloni, VSP Utrecht, NL, 685 pp.

Wegmüller, U., and C. Mätzler, 1999: Rough bare soil reflectivity model, *IEEE Trans.*

Geosci. Remote Sens., **37**, 1391–1395.

Weng, F., and N.C. Grody, 1998: Physical retrieval of land surface temperature using the special sensor microwave imager, *J. Geophys. Res.,* **103**(D8), 8839-8848.

Weng, F., Y. B. Yan, and N.C. Grody, 2001: A microwave land emissivity model. *J. Geophys. Res.,* **106**(D17), 20,115-20

Xia, Y., K. Mitchell, M. Ek, B. Cosgrove, J. Sheffield, L. Luo, C. Alonge, H. Wei, J. Meng, B. Livneh, Q. Duan, and D. Lohmann, 2012: Continental-scale water and energy flux analysis and validation for the North American Land Data Assimilation System project phase 2 (NLDAS-2): 1. Intercomparison and application of model products, *J. Geophys. Res*., **117**, D03109.

Yang, W. B. Tan, D. Huang, M. Rautiainen, N.V. Shabanov, Y. Wang, J.L. Privette, K.F. Huemmrich, R. Fensholt, I. Sandholt, M. Weiss, D.E. Ahl, S.T. Gower, R.R. Nemani, Y. Knyazikhin, and R.B. Myneni, 2006: MODIS Leaf Area Index Products: From Validation to Algorithm Improvement," *IEEE Trans. Geosci. Remote Sens.* **44**, 1885-1898.